博士論文

Coherent Doppler lidar observational studies on mesoscale phenomena associated with sea breezes

コヒーレントドップラーライダーを用いた海風に関連するメソスケール現象の観測的研究

岩井　宏徳

平成 29 年

Doctoral Thesis
博士論文

Coherent Doppler lidar observational studies on mesoscale phenomena associated with sea breezes

コヒーレントドップラーライダーを用いた海風に関連するメソスケール現象の観測的研究

東北大学大学院理学研究科
地球物理学専攻

Hironori Iwai
岩井　宏徳

論文審査委員

岩崎　俊樹　教授（主査）
早坂　忠裕　教授
青木　周司　教授
森本　真司　教授
岩渕　弘信　准教授
山崎　剛　　准教授

2017
平成 29 年

Acknowledgements

I would like to express my sincere appreciation to my advisor, Professor Toshiki Iwasaki, for his guidance, supervision, and advice in this thesis. I would like to thank my committee members, Professors Tadahiro Hayasaka, Shuji Aoki, and Shinji Morimoto, and Associate Professors Hironobu Iwabuchi and Takeshi Yamazaki for their comments and suggestions.

I would like to express my special thanks to my colleagues at the National Institute of Information and Communications Technology (NICT). I am deeply grateful to Drs. Shoken Ishii, Kohei Mizutani, and Toshikazu Itabe for their professional advice, fruitful discussions, and technical support regarding the coherent Doppler lidar development and observations for more than ten years. Dr. Yasuhiro Murayama gave me missions to conduct observational studies using the coherent Doppler lidar. I am very grateful to Drs. Nobumitsu Tsunematsu and Ryoko Oda for their support and discussions regarding the coherent Doppler lidar observations. I am grateful to Dr. Seiji Kawamura and Mr. Yuichi Ohno for providing the data observed by the wind profiler radar and ceilometer. I also thank all members of the remote sensing group at NICT for their valuable discussions, comments, and support.

I would like to thank Dr. Izumi Yamada of the Electronic Navigation Research Institute and Dr. Naoki Matayoshi of the Japan Aerospace Exploration Agency for providing the data observed by the coherent Doppler lidar and helicopter. I wish to thank Drs. Kenichi Kusunoki and Eiichi Sato for providing the data observed by the Ku-band radar. The data of surface meteorological sensors at Sendai Airport were provided by the staff members of the Sendai Aviation Weather Center.

The field experiment at Sendai Airport in 2007 was funded by the Japan Ministry of Education, Culture, Sports, Science and Technology (MEXT) (PI: Professor Toshiki Iwasaki, 19204046). The field experiment at Tokyo in 2012 was conducted under a project called Tokyo Metropolitan Area Convection Study for Extreme Weather Resilient Cities (TOMACS), which was supported by the Japan Science and Technology Agency (JST) and the MEXT as part of the “Social System Reformation Program for Adaption to Climate Change” project.

Abstract

Sea breeze is a local wind driven by the differential heating between land and sea. It occurs at coastal locations throughout the world and has significant coastal impacts including changes in air quality and convection initiation. Because populations are more rapidly concentrating in coastal areas than elsewhere, not only in Japan but worldwide, the sea breeze is an important meteorological phenomenon, and its processes and effects need to be continually understood. The convective internal boundary layer (CIBL) and sea-breeze front (SBF), which are the components of the sea breeze system, are key features owing to their significant impacts on the transport and diffusion of pollutants and on cumulus cloud development.

This thesis is devoted to an observational study of the dynamic structure of mesoscale phenomena associated with sea breezes based on coherent Doppler lidar (CDL) observations. CDLs are one of the best tools for observing near-surface wind structures because of their characteristics of eye safety, narrow beam, and no sidelobe-induced ground clutter. In this thesis, the structure and performance of two CDL systems developed by the National Institute of Information and Communications Technology (NICT) are described.

Three mesoscale phenomena associated with sea breezes are analyzed with the CDLs along with other meteorological instruments. The mesoscale phenomena focused on in this thesis are (i) horizontal convective rolls (HCRs) and near-surface streaks formed in a CIBL, (ii) a strong updraft at an SBF and the associated vertical transport of a near-surface dense aerosol, and (iii) a convection initiation associated with an isolated convective storm triggered by an SBF.

In the first case study, the three-dimensional structures of several-hundred-meter-scale HCRs and near-surface streaks in the slightly unstable CIBL formed in the sea-breeze layer are observed by two CDLs and a helicopter at Sendai Airport. Dual-Doppler lidar analysis retrieves the streaky structures of the streamwise and vertical velocity fluctuations and convergence-divergence patterns of cross-stream velocity fluctuations that were elongated in the streamwise direction near the surface. The updraft of the HCRs originated in the narrow bands of near-surface low-speed streaks. This structure is consistent with the results of previous large-eddy simulation studies. The aspect ratios of HCRs are close to that predicted by linear theories. The difference between the wavelengths of the HCRs and streaks to the north and south of Sendai Airport can be explained in terms of the different surface-heating conditions and surface roughnesses. This has recently been confirmed by numerical simulation studies using an advanced mesoscale weather forecasting system with a super-high resolution. The CDLs also performed intersecting range height indicator (RHI) scans in order to retrieve vertical profiles of horizontal wind vectors. The spatial variation in vertical wind profile in the sea-breeze layer and that in CIBL heights in the near-shore coastal area could be measured by this technique.

In the second case study, a strong updraft at an SBF and the associated vertical transport of a near-surface dense aerosol, which occurred in the Tokyo metropolitan area, are observed by the CDL and a ceilometer. By a two-dimensional variational method, the vertical air motion at the SBF is retrieved from CDL data on RHI scans. A strong updraft of approximately 5 m s^{-1} was formed over the SBF penetrating

from Sagami Bay. The horizontal and vertical scales of the updraft were about 500 m and 2 km, respectively. The updraft reached the mixing height. The updraft was triggered by the interaction between the SBF and the prefrontal thermal. Immediately after the updraft was observed by the CDL, an intense aerosol backscatter up to 2 km was observed by the ceilometer. The observational results suggest that the near-surface dense aerosols trapped in the sea-breeze head escaped from the nose of the SBF and were then vertically transported up to the mixing height by the updraft over the SBF. This implies that these phenomena occurred not continuously but intermittently. The interaction situations between the SBF and the prefrontal thermal can affect the wind structure at the SBF and the regional air quality.

In the third case study, the dynamics leading to a convection initiation associated with an isolated convective storm that occurred in the Tokyo metropolitan area is clarified using different remote sensing instruments including the CDL. Before the convection initiation, a southeasterly flow transported water vapor inland from Tokyo Bay and a well-mixed and cumulus-cloud-topped convective boundary layer developed. A convergence line in the form of an SBF also moved inland from Tokyo Bay. A near-surface air parcel was lifted to its lifting condensation level (LCL) by an updraft in a convergence zone with a 3 km horizontal scale, which formed the west edge of the convergence line. The saturated air parcel at the LCL was then lifted to its level of free convection (LFC) by the updrafts associated with thermals below the cumulus cloud base. The first echo of hydrometeors was detected by a Ku-band radar about 6 min after the air parcel reached its LFC; then, the convective cell developed rapidly. When an SBF arriving from Sagami Bay passed under the cell, the updraft over the nose of the SBF triggered a new precipitation cell, but no intensification of the preexisting cell was observed.

On the basis of the three case studies, this thesis clarifies (i) the three-dimensional structure of convection in the CIBL formed in the sea-breeze layer, (ii) the formation of the updraft at the SBF, (iii) the effect of the SBF on the vertical transport of a near-surface dense aerosol, and (iv) the effect of the SBF on the convection initiation of an isolated convective storm. The observational results obtained by the CDLs along with other meteorological instruments provide new insights into the vertical turbulent transport of momentum and heat within the CIBL formed in the sea-breeze layer and the vertical transport of aerosols and water vapor at the SBF.

Contents

List of Tables

List of Figures

1. General introduction

The main objective of this thesis is to study the dynamic structures of mesoscale phenomena associated with sea breezes using coherent Doppler lidars along with other meteorological instruments. In this chapter, a brief review of the sea breeze and mesoscale phenomena associated with the sea breeze is provided. Then, an overview of the Doppler lidar for wind measurement is introduced. Finally, the scope of this thesis is illustrated, and the structure of this thesis is described.

1.1 Sea breeze and mesoscale phenomena associated with sea breeze

Sea breeze is thermally induced and caused by the differential heating between land and sea because of their different properties and energy balances. The thermal contrast produces a local-scale pressure gradient directed from sea to land at a low level in the atmosphere. The pressure gradient forces the movement of near-surface air from sea to land (pressure gradient force; PGF). The increase in the magnitude of the pressure gradient generally increases the onshore flow near the surface from the late morning to the afternoon. The onshore flow near the surface and a surmounting offshore return flow form a vertically rotating mesoscale (2–2000 km) cell, i.e., sea breeze circulation (SBC; Fig. 1.1). The SBC can occur at coastal locations throughout the world from the tropical/equatorial regions (e.g., Hadi et al. 2002) to the polar regions (e.g., Kozo 1982).

Because of economic benefits, human settlements are more concentrated in the coastal area than elsewhere. Presently, about 40% of the world population lives within 100 km of the coastline (United Nations Department of Economic and Social Affairs 2007), and this figure is expected to rise to 75% by 2025 (Hinrichsen 1998). In 1997, nearly 80% of Japan's total population lives in the coastal area, and 77% of all Japanese live in urban areas along or near the coast (Hinrichsen 1999). Since the sea breeze has a significant impact on weather, climate, and air quality in coastal areas, it is an important meteorological phenomenon and its processes, dynamics, and effects and its interaction with the environment need to be continually understood.

The sea breeze system (SBS) has long been one of the most studied atmospheric phenomena theoretically, experimentally, and numerically (e.g., Abbs and Physick 1992; Simpson 1994; Miller et al. 2003; Crosman and Horel 2010 for reviews). The sea breezes are frequently mentioned in the Ancient Greek literature (Neumann 1973). The SBS has been studied extensively since the end of World War II (Abbs and Physick 1992) and its basic dynamics and properties are well understood (Simpson 1994; Miller et al. 2003); thus the SBS is often considered to be easily understood. However, the SBS is affected by many geophysical variables, such as the prevailing background flow (e.g., Estoque 1962), latitude dependence (e.g., Rotunno 1983), the curvature of the coastline (e.g., Baker et al. 2001), and atmospheric stability (e.g., Walsh 1974). Therefore, the SBS is a very complex phenomenon and produces associated phenomena or non-linear interactions at several scales, from the meso-β scale (20–200 km) to the inertial

subrange (Miller et al. 2003). The SBS itself consists of several spatial-scale phenomena (Fig. 1.1).

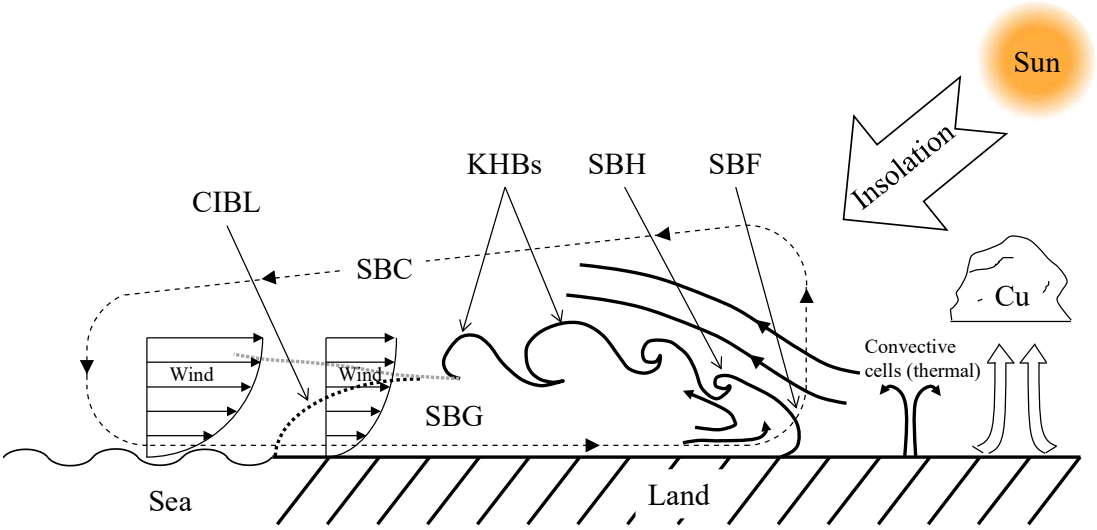

Figure 1.1. Schematic illustration of a sea breeze system (SBS; after Miller et al. 2003) and simplified two-dimensional flow model of a sea breeze front (SBF; after Simpson 1994). Some of the components of the SBS: sea breeze circulation (SBC), SBF, sea breeze head (SBH), Kelvin-Helmholtz billows (KHBs), convective internal boundary layer (CIBL), and sea breeze gravity current (SBG).

In both coastal and inland areas, the sea breeze plays an important role in the transport of pollutants (e.g., Stevens 1975), airborne pollens (e.g., Raynor et al. 1974), and flying insect pests (e.g., Berry and Taylor 1968) by forming a convective internal boundary layer (CIBL) and a sea breeze front (SBF). The CIBL is also known as a thermal internal boundary layer (TIBL; Stull 1988). When the cool and stable marine air moves over the heated land, the air near the land surface is heated by conduction and vertical mixing occurs. Owing to the increased surface roughness, turbulence is also enhanced. A CIBL develops at the coast as a result of sudden changes in thermal condition and surface roughness. The CIBL is quite shallow at the coast (typically several tens to hundreds of meters) but grows in depth with increasing time and distance from the coastline. In general, the CIBL height is proportional to the square root of the downwind distance from shore before it reaches equilibrium (e.g., Venkatram 1977; Raynor et al. 1979). The CIBL finally merges with the inland atmospheric boundary layer. The pollutants released inside the CIBL are trapped and transported inland by the sea breeze. The pollutants initially released in stable marine air above the CIBL are brought to the ground (fumigated) further inland by convection in the CIBL (Abbs and Physick 1992). Field observation related to the growth of the CIBL has been conducted in coastal areas of several countries, e.g., the United States (Raynor et al. 1979), Japan (Gamo et al. 1982), France (Druilhet et al. 1982), Sweden (Smedman and Hogstrom 1983), Greece (Melas and Kambezidis 1992), and Australia (Luhar et al. 1998). The structure and turbulence inside the CIBL were observed by instrumented towers, tethered balloons, research aircraft, and remote sensing instruments such as sodars (e.g., Prabha et al. 2002). Aerosol lidars identified the presence of the CIBL (e.g., Talbot et al. 2007; Boyouk et al. 2011). Direct measurements of the three-dimensional dynamical structure inside the CIBL, however, are difficult owing to the poor spatial representativeness of point measurements such as

instrumented towers and tethered balloons. It is also difficult for aircraft to measure the spatial distribution inside the CIBL simultaneously and low-level atmosphere over urbanized areas.

The SBF is a key feature owing to its significant contributions to the transport and diffusion of pollutants and to cumulus cloud (Cu; Fig. 1.1) development. It refers to the leading edge of the cool marine air contained within the SBC. Since the SBF is the interface between the cool marine air and the warm continental air, it is often associated with significant changes in temperature, humidity, and wind. It is well known that the SBF is a typical example of a density (or gravity) current, which is the primary horizontal flow of a fluid that is generated between two fluids with a density difference (Simpson 1987). Figure 1.1 illustrates a simplified two-dimensional flow model of an SBF (after Simpson 1994). Because the lighter continental air is uplifted at the wedge of the denser marine air, the primary updraft forms in the warm continental air ahead of the SBF. The SBF has a raised sea breeze head (SBH) because of another updraft in the cool marine air. This updraft is caused by low-level convergence between the cool marine air and the warm continental air. The height of the SBH is approximately twice that of the trailing flow (Simpson et al. 1977). The updrafts can be factors in convection initiation, the vertical transport or dilution of pollutants, and low-level wind shear (Miller et al. 2003). Kelvin-Helmholtz billows (KHBs) develop in a shear zone between the low-level trailing flow and the return flow aloft. A postfrontal roll vortex sometimes forms behind the SBF and beneath the SBH. In the late evening, the postfrontal roll vortex is separated from the sea breeze flow, and then a cutoff vortex is created when the sea breeze penetrates into a nocturnal temperature inversion (Sha et al. 1993). The cutoff vortex trapped pollutants released into the sea breeze and transported them inland (Kitada 1987).

It has long been known that boundary layer convergence lines (regions of low-level convergence of air arranged along a line; Bennet et al. 2006) are sometimes precursors to convection initiation in the absence of large-scale forcing (e.g., Wilson and Schreiber 1986). The convection initiation along convergence lines associated with the SBS including the SBF has been an active area of research. From the 1940s, there have been several observational studies of convective activity in relation to the sea breeze over south Florida (Byers and Rodebush 1948; Gentry and Moore 1954). Thereafter, numerous observational studies were conducted to study the effect of sea breezes on the convection initiation over south Florida (e.g., Frank et al. 1967; Pielke and Cotton 1977; Burpee and Lahiff 1984; Balanchard and Lopez 1985). A three-dimensional modeling study by Pielke (1974) showed that the location of thunderstorms was controlled by the location and movement of the sea breeze. In the Convection and Precipitation/Electrification (CaPE) project, which was carried out in Florida during the summer of 1991, Wilson and Megenhardt (1997) indicated that cumulonimbus clouds associated with SBFs moving inland from the east coast of Florida were small and short-lived, since the convergence at the SBFs was weak. Using Doppler radar, aircraft, satellite, and surface information, Wakimoto and Atkins (1994) and Atkins et al. (1995) discussed detailed observations taken during two sea-breeze events. They found that intersections of horizontal convective rolls (HCRs) with SBFs were preferential locations for cloud development owing to the vertical lifting by HCR updrafts. They also pointed out that the orientation of HCRs relative to the SBF plays a key role in the timing and location of convection. Collisions between

SBFs and HCRs or other boundaries such as gust fronts, however, do not always initiate convection (e.g., Wilson and Schreiber 1986; Stensrud and Maddox 1988). Kingsmill (1995) found that the collision of an SBF and a gust front generated from thunderstorms caused the increase in the magnitude of convergence at low levels but the decrease in its depth due to the effects of the relatively shallow SBF. As a result, convective activity and updrafts were not enhanced after the collision.

The interactions between the SBF and other meteorological phenomena including the HCRs have a crucial contribution to variations in SBF structure. In the daytime, which is conducive to the formation of the SBS, convective cells with a horizontal scale of a few kilometers develop above the land surface (Stull 1988). In a laboratory experiment using a water tank, Mitsumoto et al. (1983) indicated that the convective cells form in a mixed layer with a uniform thickness over land before the sea breeze moves inland. In aircraft observations, Stephan et al. (1999) and Wood et al. (1999) found that convective cells ahead of the SBF have a considerable contribution to the SBF propagation speed and frontal shape. Ogawa et al. (2003) conducted a two-dimensional numerical study of interactions between an SBF and pre-frontal convective cells that form over land ahead of the SBF. They showed that when the SBF moves to the updraft region of a convective cell, the updraft at the SBF is intensified. The periodic variations in SBF propagation speed are associated with alternately generated frontogenesis and frontolysis.

The SBF has been studied using several methods: analytical solutions (e.g., Feliks 1988), numerical simulations (e.g., Sha et al. 1991, 1993; Ogawa et al. 2003), laboratory tank experiments (e.g., Simpson et al. 1969; Simpson and Britter 1980; Mitsumoto et al. 1983), and field measurements (e.g., Simpson et al. 1977; Helmis et al. 1987; Chiba 1993, 1997; Reible et al. 1993; Lapworth 2000; Banta et al. 2005; Darby 2005; Tucker et al. 2010). Lapworth (2000) pointed out that surprisingly few sea-breeze studies used the above-surface measurements, although the sea breeze is a relatively lower tropospheric phenomenon. Recently, intensive field campaigns aimed at better understanding the circulation of sea breezes and pollutants have been carried out using numerous in-situ and remote sensing instruments, both ground-based and on airborne and shipborne platforms (e.g., Texas Air Quality Studies (TexAQS) 2000 and 2006, presented in Banta et al. (2005) and Parrish et al. (2009), and Expérience sur Site pour COntraindre les Modèles de Pollution atmosphérique et de Transport d'Emissions (ESCOMPTE; Cros et al 2004)). However, since mesoscale vertical air motion is difficult to measure directly, field measurements have only minimally investigated the three-dimensional wind structure of the SBF and the vertical transport of pollutants at the SBF.

1.2 Doppler lidar overview for wind measurement

"Lidar" is the acronym for "LIght Detection And Ranging." Doppler lidars transmit a narrow-bandwidth and collimated laser (Light Amplification by Stimulated Emission of Radiation) beam into the atmosphere and receive the light backscattered by moving aerosol particles (Mie scattering) and molecules (Rayleigh scattering) in the atmosphere. The Doppler shift of the backscattered light induced by the moving aerosol particles and molecules is estimated by signal processing to provide the line-of-sight

component of the wind vector. Doppler lidars operate typically at wavelengths from 0.35 to 10 μm. Doppler Radars (RAdio Detection And Ranging) operate with radio waves with wavelengths from 0.3 to 600 cm and the radio waves are scattered by hydrometeors, insects, and refractive index fluctuations in the atmosphere. Since Doppler lidar wavelengths are three to five orders of magnitude shorter than radar wavelengths, Doppler lidars provide different information from Doppler radars. Therefore, Doppler lidars and radars complement each other in meteorological studies.

Doppler lidars can be categorized into two main types: direct detection (or incoherent) and coherent (or heterodyne detection). The difference between the direct detection Doppler lidar (DDL) and the coherent Doppler lidar (CDL) is based on fundamental methods used to determine the Doppler shift. DDL systems determine the Doppler shift using a spectral resolving analyzer. Narrow-band spectral filters are used for DDL systems to convert a Doppler-shifted frequency change to a spectral intensity change. The spectral intensity change is directly detected using some techniques, such as the edge technique (e.g., Korb et al. 1992). Since the targets for the DDL are aerosol particles and molecules, it can observe the winds from the troposphere to the lower mesosphere. Background light, which is sunlight scattered from the atmosphere, cannot be ignored for the DDL during daytime, because the molecular backscattered signal is the main source for the DDL at visible light wavelengths.

In the CDL systems, the backscattered signal from the moving aerosol particles is optically mixed with a laser output (reference signal) of a local oscillator and the low-frequency component of the resulting beat signal is detected by a narrow-band detector. The frequency component is equal to the frequency difference between the two signals, which is the sum of a Doppler-shifted frequency and a carrier (arbitrary fixed offset) frequency. The dominant source of the noise is the shot noise generated by the local oscillator, and the near-quantum-limited detection of the backscattered signal can be achieved by the CDL systems. Background light is not an issue owing to the narrow-band detection. Therefore, the CDL can achieve a better signal-to-noise ratio (SNR) for weak scatter and the same performance during daytime and nighttime. Since the targets for the CDL are aerosol particles, it is suitable for observing the winds in areas with higher aerosol loadings, i.e., the atmospheric boundary layer and lower troposphere. The CDL also has advantages compared with the DDL in extended range measurement (typically several km to a few 10 km) at middle infrared wavelengths, which are typically from 1 to 10 μm and include an eye-safe wavelength longer than 1.5 μm (Menzies and Hardesty 1989). The CDL has made significant progress over the past few decades with the great advance of single-frequency laser technology. Because of recent advances in eye-safe solid-state and fiber laser technology, CDLs are becoming more accessible to the meteorological research community (Henderson et al. 2005; Werner 2005).

The CDL has been proposed for global wind measurements using space-based platforms (Baker et al. 1995; Huffaker et al. 1984; Menzies 1986). National Institute of Information and Communications Technology (NICT) started studying an eye-safe 2-μm CDL technology for satellite-based observations of wind on a global scale from 2001. NICT's Doppler lidar was developed as a precursor system to demonstrate the feasibility of using the CDL from flying objects (see Section 2.1). Since high-output-energy solid-state laser technology might be required for long-range wind sensing from

space-based platforms, a 2-μm conductively cooled, laser-diode-pumped single-frequency Q-switched solid-state laser has been developed at NICT for basic studies on a future spaceborne Doppler lidar (Mizutani et al. 2008; Mizutani et al. 2015). The development of a coherent 2-μm differential absorption and wind lidar (Co2DiaWiL; Ishii et al. 2010) with this laser started from 2006. The Co2DiaWiL served as a ground-based testbed for future airborne and spaceborne lidar missions to measure simultaneously the CO_2 concentration and wind (see Section 2.2).

Since the direct measurements are limited to the radial component of wind velocity by a single CDL, the CDL needs to operate at different combinations of azimuth and elevation angles to observe the two-dimensional and three-dimensional wind fields. The plan position indicator (PPI) and range height indicator (RHI) scans are two basic types of scanning. In a PPI scan, the CDL scanned in azimuth at constant elevation angles to observe the horizontal distribution of air flows over a large spatial area. In an RHI scan, the CDL scanned in the elevation angle at a fixed azimuth to observe the vertical distribution of air flows in a vertical slice. To derive vertical profiles of mean wind speed and direction using a single CDL, the velocity azimuth display (VAD) technique (Browning and Wexler 1968) and Doppler beam swinging (DBS) technique (Strauch et al. 1984) are used on the assumption of the horizontal homogeneity of the wind in the sampling volume. In addition, several techniques were proposed to extract the two-dimensional wind vectors in PPI/RHI scans. For example, Choukulkar et al. (2012) applied the optimal interpolation technique to retrieve horizontal wind vectors on PPI scans without the assumption of the wind field homogeneity. Chan and Shao (2007) adopted a variational method to retrieve horizontal wind vectors on PPI scans. Dual-Doppler analyses using noncollocated two CDLs can retrieve the three-dimensional wind vectors without the assumption of spatial homogeneity (e.g., Rothermel et al. 1985). However, dual-Doppler lidar measurements have been rare owing to the expensiveness of CDLs.

The aforementioned observational techniques, eye safety, narrow beam, and no sidelobe-induced ground clutter of CDLs allow detailed measurements of mesoscale atmospheric flows near the surface, in complex terrains, and in densely urbanized areas. The CDL measurements with high spatial and temporal resolutions can be used to compensate for the lack of the spatial representativeness by point measurements such as in-situ sensors. Several previous studies demonstrated that the CDL was a relevant instrument for observing the SBS.

Bilbro et al. (1984) used an airborne 10.6 μm CO_2 CDL to measure the two-dimensional vector wind field. They conducted two research flights in July 1981 in the California Central Valley to study the SBC. They showed that the airborne lidar system was effective in capturing the mesoscale sea breeze flow of the entire valley. Carroll (1989) analyzed data taken from the same airborne CDL. The observed data were taken in August 1984 in the California Central Valley. The airborne lidar captured the vertical shear of the SBC around a well-defined temperature inversion observed by a sounding.

The Land/Sea Breeze Experiment (LASBEX; Intrieri et al. 1990) was conducted at Monterey Bay, California, in September 1987 to study the vertical structure and mesoscale variation of the land/sea breeze using the National Oceanic and Atmospheric Administration's (NOAA's) ground-based 10.6 μm transverse excited atmospheric-pressure (TEA) CO_2 CDL (TEACO2; Post and Cupp 1990). Using the scanning

capability of the TEACO2 CDL, Banta et al. (1993) showed the horizontal and vertical variabilities of the sea breeze flow. They observed no return flow above the sea breeze using RHI scans perpendicular to the coast and parallel to the sea breeze. They argued that previous studies observed no return flow using balloonborne instruments, but it was difficult to conclude that the return flow was not there because of large deviations of the observational data in time and space. They also indicated that sea-breeze winds consisted of two scales of flow in the vertical direction and in time: a shallow, stronger sea breeze forming in midmorning and a weaker, deeper sea breeze forming later in the day. Banta (1995) extensively analyzed the TEACO2 CDL measurements on a day with offshore flow indicated before sunrise and after sunset. It is hypothesized that a local temperature contrast at the coastline produces the shallow sea breeze, whereas a larger-scale temperature contrast between the cool ocean and the hot interior valleys of California produces the deeper sea breeze later in the day. Darby et al. (2002) conducted additional mesoscale simulations to investigate the topographic effects on the two scales of sea-breeze flow and compared the model results with the TEACO2 CDL data. They concluded that the shallow sea breeze was caused by the land–sea temperature contrast and that the deeper sea breeze was caused by the onset of deep slope flow associated with the mountains near the coast. They also showed that the depth of the sea-breeze flow was enhanced by the mountains, but its speed was not necessarily enhanced. The TEACO2 CDL measurements clarified that the sea breeze at and around Monterey Bay is complex and highly three-dimensional owing to the complex terrain surrounding Monterey Bay. An airborne 2 μm Twin Otter Doppler wind lidar (TODWL; De Wekker et al. 2012) observation was conducted in the Salinas Valley and surrounding mountains near Monterey Bay in 12 November 2007. The observed data showed that a sea breeze turned into upvalley flows in the Salinas Valley and that the speed of the upvalley flows was enhanced by vertical sinking motions. Consistent with previous studies (e.g., Banta et al. 1993), no return flow associated with the sea breeze was observed. They claimed that the airborne Doppler lidar had the ability to provide a detailed and comprehensive three-dimensional structure of the sea breeze.

The role of land/sea-breeze circulations in air pollution transport was investigated using both airborne and ground-based 10.6 μm TEA CO_2 CDLs (WIND and TWL; Werner et al. 2001) during the ESCOMPTE experiment, conducted in June and July 2001 in southern France. Bastin et al. (2005) documented the vertical structure of the sea breeze using the TWL and estimated the sea breeze flow velocity and depth from the TWL data. The estimated values were comparable to the corresponding values calculated by Steyn's scaling analysis (Steyn 1998; Steyn 2003). The WIND observed the profile of the three-dimensional wind vector around Rhône and Durance valleys to investigate the impact of these valleys on sea-breeze dynamics. The WIND and TWL observations clarified that the acceleration of the channeled flow in the Durance valley suppresses the sea breeze, whereas that in the Rhône valley does not generally affect the sea breeze significantly. Lemonsu et al. (2006) conducted three-dimensional mesoscale simulations to investigate a complex stratification of the sea breeze and compared the model results with the TWL data. The presence of a shallow sea breeze (SSB) superimposed on a deep sea breeze (DSB) above Marseille during daytime was revealed by the TWL observations and simulations. The southerly SSB south of Marseille and the westerly SSB north of Marseille flowing perpendicular to the local

temperature gradient converged above the center of the city. The south-east DSB flows were perpendicular to the regional temperature gradient and forced by the gradient formed between the land and the Mediterranean Sea. Drobinski et al. (2006) showed that the WIND measurements mapped the three-dimensional structure of the SBC caused by the complex coastline shape and topography. The WIND measurements were used to estimate the sea breeze intensity, depth, and horizontal extent and to evaluate Steyn's scaling laws (Steyn 1998; Steyn 2003). If strong synoptic flows prevailed, the scaling laws failed to predict the sea breeze characteristics. Bastin et al. (2006) analyzed the event of sea-breeze–mistral interactions using the WIND measurements and a three-dimensional mesoscale model and found that the event was associated with high ozone concentrations in the coastal area. The mistral refers to a severe northerly wind that develops along the Rhône valley. The WIND captured the spatial variability of the vertical structure of the sea breeze and mistral. Because of the opposing colder and dryer mistral flow, the warmer sea breeze flow could not penetrate far inland and the ozone accumulated close to the coastline. Drobinski et al. (2007) pointed out that the synergetic use of different remote sensing instruments including CDLs with conventional in situ sensors allowed us to capture the detailed fine structure of the sea breeze and to validate high-resolution numerical models by comparing the CDL data with model outputs.

To investigate the relationship between the lower tropospheric vertical structure of winds and the ozone concentration, the TexAQS 2000 experiment was conducted in August and September 2000 in Houston using the TEACO2 CDL. Banta et al (2005) showed an SBF formed along the coastline of Galveston Bay and the Gulf of Mexico and captured its sharp structure using RHI scans of the TEACO2 CDL. Vertical profiles of the horizontal winds derived from high-elevation-angle PPI scans of the TEACO2 CDL showed the diurnal variation in the boundary layer. The TEACO2 CDL captured the opposing offshore flow and growing sea breeze flow. On several days with high ozone concentration, the large-scale flow was offshore and the SBF did not move inland until mid- to late afternoon.

Measurements made with a shipborne NOAA's high-resolution Doppler lidar (HRDL; Grund et al. 2001) were conducted during the TexAQS 2006 experiment to study the relationship between the lower tropospheric vertical structure of winds and the ozone concentration in Houston, Texas. Tucker et al. (2010) showed that the high-resolution (vertical and temporal resolutions of 5–30 m and 15 min) wind profiles derived from the HDRL data revealed the structure and evolution of strong onshore nocturnal low-level jets and provided observations of ozone mixing and transport related to the jets in the Houston coastal regions. The high-resolution wind profiles clarified the mechanism by which the afternoon sea breeze progressed into a nocturnal low-level jet. If the strong southerly onshore flow and resulting strong onshore jets prevailed, ozone and oxidant concentrations were low at night and the following afternoon. In contrast, if the dominant flow was northerly and the resulting relatively weak onshore jets prevailed, ozone and oxidant concentrations were higher on the next day and associated with the jets.

In Japan, Shibata et al. (1991) developed a CDL using a hybrid CO_2 laser with a low pressure gain section below the threshold. The configuration of the lidar is much simpler than that of the lidar with an injection-locked TEA CO_2 laser. To evaluate the CDL performance, they observed wind variation using

the DBS technique within heights of approximately 500 m caused by the passage of an SBF over the Tokyo metropolitan area. Tsunematsu et al. (2009) first observed the formation of a sharp multi-layered wind structure over the Tokyo metropolitan area after the passage of an SBF using NICT's Doppler lidar with RHI scans. They described that the multi-layered wind structure was associated with the SBC and consisted of four layers: (i) the southerly sea breeze flow below 0.8 km above mean sea level (AMSL), (ii) a thin weak wind layer between 0.8 and 1 km AMSL, (iii) the northerly return flow at more than 1 km AMSL, and (iv) a northerly synoptic wind at more than 3 km AMSL. Fujiwara et al. (2012) used a 1.54 μm CDL with low-elevation-angle PPI scans to detect dust-devil-like vortices (DDVs) over an urban area of Sapporo. The CDL observations clearly show that all DDVs were cyclonic as observed on 4 October 2006. They discussed that not only the heat-island circulation but also the sea breeze and valley winds intensified the cyclonically mesoscale circulation in Sapporo. Moreover, they found that the majority of DDVs developing along the SBF were cyclonic. Fujiwara et al. (2010) compared the cases indicating the presence and absence of a DDV to identify meteorological conditions for the DDV development associated with the SBF using the same CDL. The optimal conditions for DDV development were (i) a relatively stronger horizontal shear at the SBF, (ii) a larger boundary layer height, and (iii) balance between the vertical wind shear in the ambient environment ahead of the SBF and the horizontal vorticity at the SBF.

There were many observational studies on the sea breeze using ground-based, airborne, and shipborne CDLs. The majority of the studies mainly focused on the SBC to investigate its structure and associated air pollution transport. On the other hand, detailed observations of the dynamic structure inside the CIBL and at the SBF have been rare (e.g., Fujiwara et al. 2010).

1.3 Scope of this thesis

As described above, the sea breeze is an important meteorological phenomenon because of its significant impact on weather, climate, and air quality in coastal areas. The CIBL and SBF among the components of the SBS are key features owing to their significant contributions to the transport and diffusion of pollutants and to cumulus cloud development. Since the SBS is a very complex and relatively lower tropospheric phenomenon and produces associated phenomena at several scales, it is important to observe the near-surface three-dimensional wind structure of these phenomena using remote sensing instruments with high spatial and temporal resolutions. Doppler radars with high sensitivity can observe optically-clear-air echoes in the atmospheric boundary layer caused by birds, insects (Geotis 1964), and refractive index gradients (Atlas 1960; Eastwood and Rider 1961). However, it is not always possible for Doppler radars to measure winds in clear air. Furthermore, it is difficult for Doppler radars to observe near-surface phenomena because of significant ground-clutter contamination. Although wind profiler radars can observe winds under clear air condition by receiving echoes from refractive index fluctuations, they cannot observe the spatial distributions of winds. CDLs are one of the best tools for observing the near-surface three-dimensional wind structure of the mesoscale phenomena associated with the sea breezes, because of their characteristics of eye safety, narrow beam, and no sidelobe-induced ground clutter.

Mesoscale phenomena, which we focus on in this thesis, are (i) HCRs and near-surface streaks formed in a CIBL, (ii) a strong updraft at an SBF and the associated vertical transport of a near-surface dense aerosol, and (iii) a convection initiation associated with an isolated convective storm triggered by an SBF. These phenomena formed over urbanized areas, their dynamic structures were complex and their temporal and spatial variabilities were large. The aim of this thesis is to study their three-dimensional wind structures and temporal evolutions by using CDLs along with other meteorological instruments.

This thesis describes the structure and features of two CDL systems developed by NICT, and discusses the results of mesoscale phenomena observed by the CDL systems. The contributions of this thesis and the author are summarized in Table 1.1. The items written in red are the author's main contributions.

Chapter 2 is devoted to the detailed descriptions of two CDL systems, NICT's Doppler lidar, and Co2DiaWiL, which are developed by NICT. Their principle, structure, specifications, and data processing method to derive the radial velocity are described. The performance of the Co2DiaWiL is also described from the viewpoint of demonstrating system capabilities for remote measurements of wind velocities.

In Chapter 3, the three-dimensional structure of HCRs and the near-surface streaks in a CIBL, which occurred at Sendai Airport on 18 and 19 June 2007, are presented. In this case study, the dual-Doppler lidar observation was conducted using NICT's Doppler lidar and Electronic Navigation Research Institute (ENRI)'s Doppler lidar. The three-dimensional structure of HCRs and the near-surface streaks in the CIBL were retrieved from the results of dual-Doppler lidar analysis. The thermodynamic structure was observed using heliborne sensors. The results of dual-Doppler lidar analysis are compared with those of large-eddy simulations and linear theories.

In Chapter 4, a strong updraft at an SBF and the associated vertical transport of a near-surface dense aerosol, which occurred in the Tokyo metropolitan area on 27 May 2008, are presented. In this case study, the vertical and horizontal structures of the well-developed SBF penetrating from Sagami Bay were observed using NICT's Doppler lidar. Using the NICT's Doppler lidar and in-situ surface meteorological station data, the hypothesis that the SBF is the leading edge of a density (or gravity) current is discussed. The SBF-related vertical aerosol transport is presented using the observed results of NICT's Doppler lidar and a ceilometer. Effects of the interaction between the SBF and the prefrontal thermal on the vertical aerosol transport are discussed.

In Chapter 5, a convection initiation associated with an isolated convective storm triggered by an SBF in the Tokyo metropolitan area on 17 August 2012 is presented. The triggering mechanism leading to the convection initiation of the storm is discussed using observed results of the Co2DiaWiL and various radars. The trajectory of the air parcel from the surface to its level of free convection (LFC) is analyzed. The effect of the interaction between the SBF and the preexisting cell is also discussed. It is shown that the synergetic use of different remote sensing instruments including CDLs is important for monitoring a pre-storm environment in the vicinity of convergence lines and for capturing the motions of air parcels for a better understanding of convection initiation processes.

In Chapter 6, we give the conclusions obtained by this thesis. From the viewpoints of disaster

prevention and mitigation, it is identified that the synergetic use of CDLs and radars is essential for detecting as soon as possible severe mesoscale phenomena such as localized heavy rainfall and tornadoes.

Table 1.1. Contributions of this thesis and the author.

Coherent Doppler lidar development	Case studies
NICT's Doppler lidar (Section 2.1)	
Optical system	(i) HCRs and near-surface streaks formed in a CIBL
Signal processing	Dual-Doppler lidar analysis
Performance evaluation	(Chapter 3)
	(ii) A strong updraft at an SBF and associated vertical transport of near-surface dense aerosol
	Two-dimensional variational wind retrieval method
	(Chapter 4)
Co2DiaWiL (Section 2.2)	
Optical system	(iii) A convection initiation associated with an isolated
Signal processing	convective storm triggered by an SBF
Performance evaluation	(Chapter 5)

2. Coherent Doppler lidar systems

In this chapter, the two coherent Doppler lidar (CDL) systems used in this thesis are described in detail. The National Institute of Information and Communications Technology (NICT) started a study on an eye-safe 2-μm airborne coherent Doppler lidar (NICT's Doppler lidar) from 2001. The development of NICT's Doppler lidar was fundamental study for future spaceborne Doppler lidar missions (Baker et al. 1995; Huffaker et al. 1984; Menzies 1986). The first objective in NICT's Doppler lidar development was to perform a feasibility study of using the CDL from flying objects. The second objective was to develop an algorithm for measuring the profiles of horizontal wind vectors. The third objective was to realize a precursor system for an International Space Station-borne CDL system (Itabe et al. 2001). NICT's Doppler lidar is reviewed in Section 2.1. The development of a coherent 2-μm differential absorption and wind lidar (Co2DiaWiL) started from 2006. Further development of high-output-energy solid-state laser technology might be required for long-range wind sensing from space-based platforms (Koch et al. 2007). Therefore, a 2-μm conductively cooled, laser-diode pumped single-frequency Q-switched solid-state laser with 2.4 W power (80 mJ and 30 Hz) has been developed at NICT for basic studies on a future spaceborne CDL. Conductive cooling is a key technology used to operate the high-output-energy solid-state lasers on board satellites. The Co2DiaWiL with this laser was developed to measure CO_2 concentration and radial wind speed (Ishii et al. 2010). The Co2DiaWiL is reviewed in Section 2.2.

2.1 NICT's Doppler lidar

NICT's Doppler lidar is composed of an optical component (transmitter, receiver, and telescope) manufactured by Coherent Technologies Inc., a signal processor component, and a scanner. In the airborne experiments in 2002, 2004, and 2006, the optical component was placed in a pod attached to the bottom of a jet plane body. A silicon wedge prism was used as the scanner. In the ground-based field experiments in 2002 and 2003, the same silicon wedge prism was used. In the ground-based field experiments after 2004,

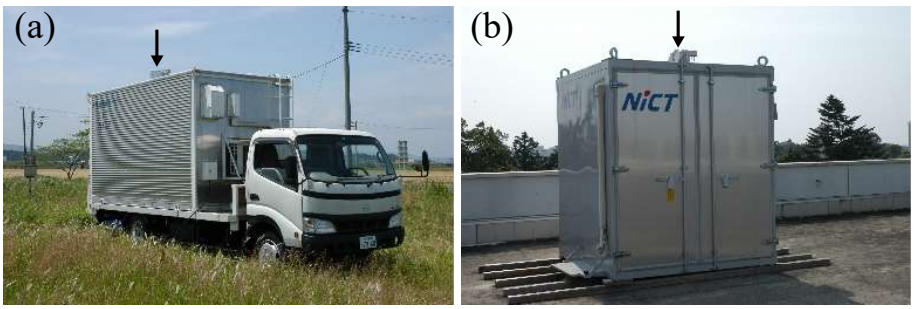

Figure 2.1. Photographs of (a) a container mounted on the cargo bed of a truck near Sendai Airport in 2007 and (b) a container stationed on the rooftop of a building at NICT headquarters in 2008. The arrow points to the scanner in (a) and (b).

the optical and signal processor components were housed in containers, and a two-axis scanner was installed on its roof (Fig. 2.1). In 2007, the container was mounted on the cargo bed of a truck near Sendai Airport (Fig. 2.1a; Section 3.2). In 2008, the container was stationed on the rooftop of a building at NICT headquarters (Fig. 2.1b; Section 4.2).

A block diagram of NICT's Doppler lidar is shown in Fig 2.2. The system parameters of NICT's Doppler lidar are listed in Table 2.1. The optical component consists of a continuous wave (CW) laser, a high-power Q-switched pulse laser, and two heterodyne detectors (mixer and detector). The CW laser is a diode-laser-pumped single-longitudinal-mode Tm:YAG laser emitting at a wavelength of 2.0125 μm. Part of the laser beam transmitted from the CW laser is passed through the acoustic optical modulator (AOM), and the frequency of the CW laser (f_L) is upshifted by 105 MHz, which is the shifted frequency (f_{shift}). The frequency-shifted laser beam is then mode-matched and injected into the high-power Q-switched pulse laser at a pulse repetition frequency of 100 Hz. The laser pulse is transmitted into the atmosphere through the telescope and scanner. The backscattered signal, which is Doppler-shifted (Doppler-shifted frequency is Δf) by moving aerosol particles, is received by the telescope. A portion of the CW laser power is photomixed with the pulse laser output and backscattered signals on heterodyne detectors.

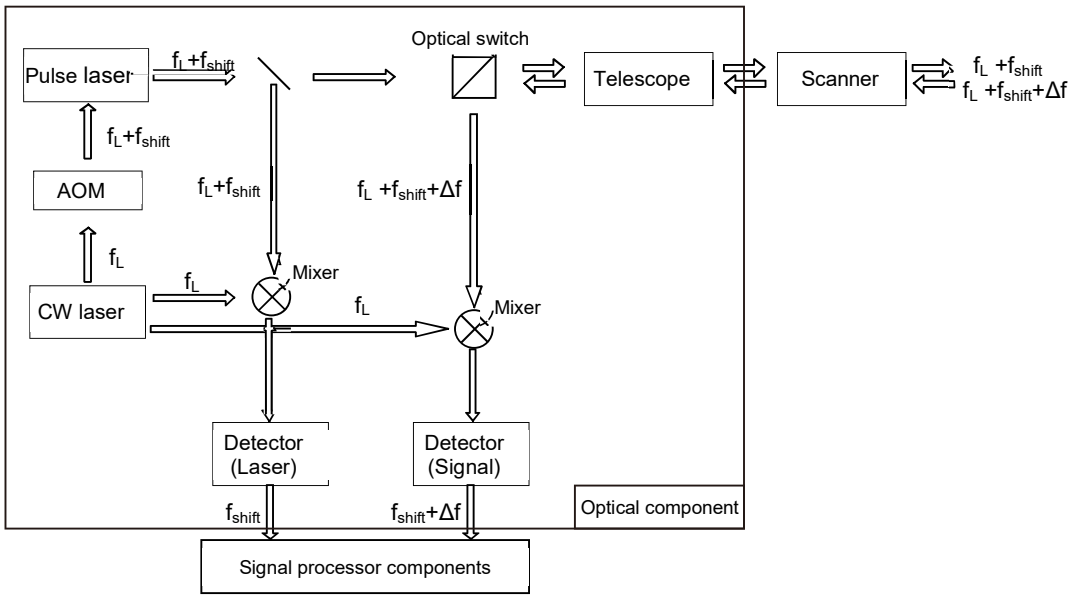

Figure 2.2. Block diagram of NICT's Doppler lidar. Here, f_L is the laser frequency, f_{shift} is the shifted frequency modulated by an acoustic optical modulator (AOM), and Δf is the Doppler-shifted frequency. Two mixers are used to mix a single-frequency CW laser beam with an outgoing laser beam and a backscattered signal.

The mixers convert the frequencies of the pulse laser output and backscattered signals down to intermediate frequencies. After amplification and filtering, the outputs of both detectors are digitized using an 8-bit analog-to-digital (A/D) converter of the signal processor component. From 2002 to 2003, a 100 MHz sampling A/D converter (Signatec, VDA500Digitizer) was used. After 2004, a 500 MHz sampling A/D converter (Gage Applied Technologies, CompuScope 82G) was used. The signal processor component digitized 65536 samples for the detector output of backscattered signals and 4096 samples for the detector output of the pulse laser (called the monitor pulse after this). The 65536 samples of the backscattered signal at a sampling frequency of 500 MHz correspond to a data system limited range of 19.6 km. In 2007 (Chapter 3), the 65536 samples of backscattered signals are divided into 46 segments of 300 samples (corresponding to 90 m lengths), and the segments are called range gates. In 2008 (Chapter 4),

Table 2.1. Specifications of NICT's Doppler lidar.

Parameters	Values
Transmitter	
Wavelength	2.0125 μm
Laser material	Tm,YAG
Pulse energy	7 mJ/pulse
Pulse width (FWHM)	560 ns
Pulse repetition frequency	100 Hz
Polarization	Circular
Receiver	
Telescope type	Mersenne off-axis
Diameter	100 mm
Magnification	10×
Detector	InGaAs
Scanner	(after 2004)
Scanning range	Azimuth −10° to 370°
	Elevation −20° to 200°
Effective clear aperture	0.1 m
Scanning resolution	0.01°
Scanning speed	Up to 60° s^{-1}
Signal processing	
Signal digitization resolution	8 bits
Signal sampling frequency	500 MHz (after 2004)
Points per range gate	300 (at 2007) or 512 (at 2008)
Range resolution	90 m (at 2007) or 153 m (at 2008)
Maximum range	19.6 km (data system limited)
Minimum range	360 m (at 2007) or 537 m (at 2008)

the 65536 samples of backscattered signals are divided into 63 segments of 512 samples (corresponding to 153 m lengths). The monitor pulse is used as a reference for subsequent signal processing steps to calculate ranges and correct pulse-by-pulse frequencies. The frequencies of the transmitted pulse laser (f_{shift}) and backscattered signal ($f_{shift}+\Delta f$) are estimated from their power spectra using the moment method in each range gate. The Doppler-shifted frequency Δf is obtained from the difference between the frequencies of the transmitted pulse laser and the backscattered signal. The radial wind velocity V_r is calculated as

$$V_r = \frac{\lambda \Delta f}{2} \tag{2.1}$$

with the laser wavelength λ (2.0125 μm). The standard deviation of the radial velocity is 0.1–0.2 m s^{-1} (Ishii et al. 2005).

NICT's Doppler lidar simultaneously measures the radial velocity and signal-to-noise ratio (SNR) in each range gate. Here, the range-corrected SNR is defined as

$$SNR(R)R^2 = \frac{P(R)}{P_N}R^2 = \frac{KP_0\beta(R)T^2(R)}{P_N}, \tag{2.2}$$

where R is the distance between the Doppler lidar and the target atmosphere, $P(R)$ is the mean signal power estimate in a range gate, P_N is the noise power, K is a constant determined by several parameters (heterodyne efficiency, detector quantum efficiency, receiver area, and optical efficiency), P_0 is the laser output power, $\beta(R)$ is the backscattering coefficient of aerosol particles and molecules, and $T(R)$ is the atmospheric transmission. In heterodyne detection, the background light power is negligible owing to a narrow detection bandwidth. At the wavelength of 2 μm, the molecular scattering is low; thus, the backscattering by aerosol particles is more important than that by molecules. At optical wavelengths, scattering within the lower atmosphere is primarily by particles of less than 1 μm in diameter (Srivastava et al. 1992), which are sufficiently small to be advected by the wind and serve as an effective tracer of the wind velocity (e.g., Frehlich 1995). From Eq. 2.2, the fluctuation in the range-corrected SNR can substitute for that in the lidar reflectivity βT^2. A high range-corrected SNR is indicative of a higher optical scattering, which is caused by many factors, such as an increase in particle concentration and aerosol swelling (i.e., a shift towards a larger-sized distribution of particles).

2.2 Coherent 2-μm differential absorption and wind lidar

The Co2DiaWiL was developed to measure CO_2 concentration and radial wind speed (Ishii et al. 2010). It was housed in a container, which was stationed on the rooftop of a building at NICT headquarters (Fig. 2.3, 35.71°N, 139.49°E, height 75 m AMSL), 20 m above ground level (AGL). This may serve as a testbed for future airborne and spaceborne lidar missions. A 2-μm conductively cooled, laser-diode-pumped single-frequency Q-switched Tm,Ho:YLF laser (Mizutani et al. 2008; Mizutani et al. 2015) was used in the Co2DiaWiL to perform long-range CO_2 and wind measurements. This laser has an operating wavelength of 2.05 μm, an output energy of 80 mJ, a pulse width of 150 ns (full width at half maximum (FWHM)), and a pulse repetition frequency of 30 Hz. While the previous system described by

Figure 2.3. Photograph of Co2DiaWiL stationed on the rooftop of a building at NICT headquarters from 2010 to 2012. The container houses the transmitter and receiver, and the scanner is installed on its roof. The arrow points to the scanner.

Ishii et al. (2010) had two master oscillators (MOs) that were single-frequency CW Tm,Ho:YLF lasers for injection seeding, the present system had three MOs to perform long-range measurements of CO_2 concentration (Ishii et al. 2012). A block diagram of the present system is shown in Fig 2.4. The system parameters for wind measurements are listed in Table 2.2.

The MO at a wavelength of 2.051250 μm, corresponding to the far wing of the R30 absorption line of CO_2, is used for the wind measurements. The laser is controlled only by adjusting the resonator temperature and the piezoelectric movement of the output coupler element. Part of the laser beam transmitted from the MO is diffracted by a single-crystal, germanium acousto-optic modulator. The

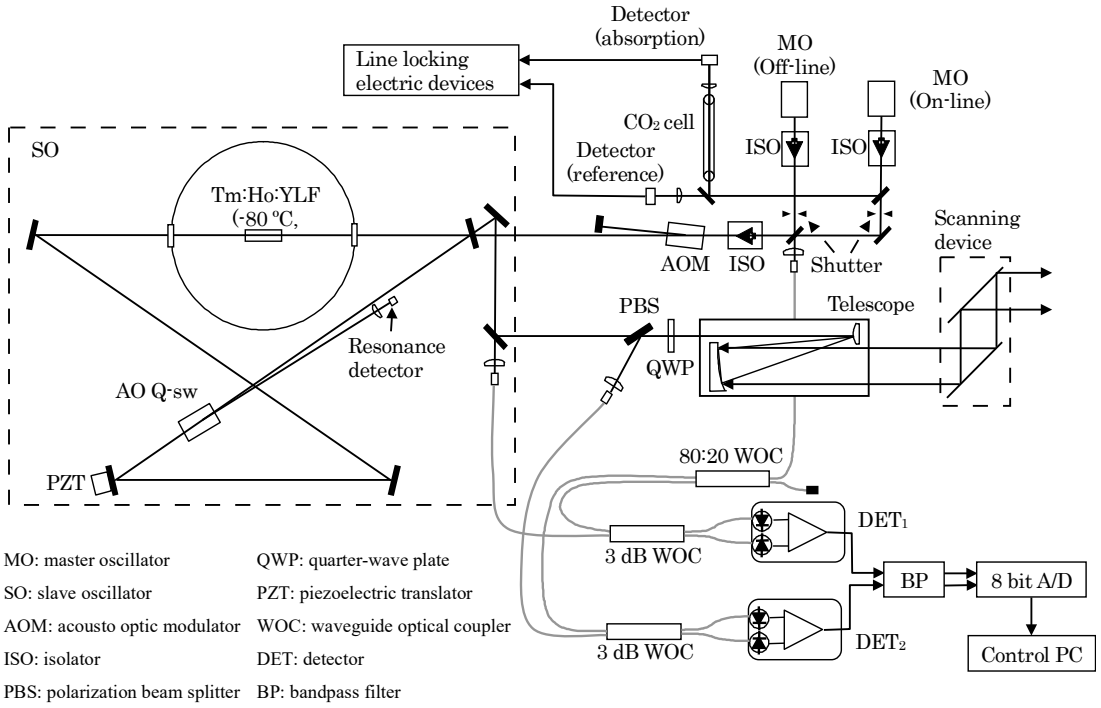

Figure 2.4. Block diagram of Co2DiaWiL (from Ishii et al. 2010).

acousto-optic modulator upshifts the frequency of the MO laser beam by 105 MHz to create an intermediate frequency, and the diffracted beam is injected into the acousto-optic Q-switched (AO Q-sw) slave oscillator (SO) in a ring-configuration resonator. A single-frequency Q-switched laser pulse is obtained by injection seeding with the upshifted MO laser beam matched to the SO with the ramp-and-fire technique (Henderson et al. 1986). The SO ring cavity is swept until a resonance is detected that triggers the AO Q-sw.

The pulsed laser beam is transmitted to the atmosphere by a 0.1-m-diameter off-axis telescope. After being expanded by the telescope, the pulsed laser beam is pointed and scanned with a waterproof two-axis scanner mounted on the container roof. The scanner is capable of full hemispherical coverage, 0.01°

Table 2.2. Co2DiaWiL specifications for wind measurements.

Parameters	Values
Transmitter	
Wavelength	2.051250 μm (2051.250 nm)
Laser material	Tm,Ho;YLF
Pulse energy	50–80 mJ/pulse operationally
Pulse width (FWHM)	150 ns
Pulse repetition frequency	30 Hz
Polarization	Circular
Receiver	
Telescope type	Mersenne off-axis
Diameter	100 mm
Magnification	10×
Detector DET1	InGaAs-PIN photodiode
Detector DET2	Balanced InGaAs-PIN photodiode
Scanner	
Scanning range	Azimuth −10° to 370°
	Elevation −20° to 200°
Effective clear aperture	0.1 m
Scanning resolution	0.01°
Scanning speed	Up to 60° s^{-1}
Signal processing	
Signal digitization resolution	8 bits
Signal sampling frequency	500 MHz
Points per range gate	256
Range resolution	76 m
Maximum range	39.2 km (data system limited)
Minimum range	153 m

precision, and scanning speeds of up to 60° s^{-1}. A scan sequence is downloaded in operation to a motion controller card (NOVA Electronics, MC8043P) housed in a personal computer (PC) that acquires data for the Co2DiaWiL, and the scanner independently executes the scan sequence until it is completed. The elevation and azimuth angles of the scanner are acquired from the PC every single shot, by reading the outputs of an encoder built into a scanner controller.

The signal backscattered by moving aerosol particles is photomixed with a portion of the laser beam transmitted from the MO on an InGaAs-PIN photodiode (DET1). A small portion of the pulsed laser beam is also photomixed with the off-line laser output on a balanced InGaAs-PIN photodiode (DET2) to monitor the frequency of the outgoing laser pulse. The two photoreceivers, DET1 and DET2, convert the frequencies of the laser pulse and backscattered signals into intermediate frequencies for heterodyne detection. The outputs of the photoreceivers are passed through a preamplifier and a bandpass filter.

The outputs of DET1 and DET2 are digitized at a 500 MHz sampling frequency f_{max}, using 8-bit A/D converters starting from a 30-Hz trigger. The current system digitized 131072 samples for the DET1 output (called backscattered signals after this) and 4096 samples for the DET2 output (called the monitor pulse after this). The 131072 samples of backscattered signals at a sampling frequency of 500 MHz correspond to a data system limited range of 39.2 km. The 131072 samples of backscattered signals are divided into 512 segments of 256 samples (corresponding to 76.75 m lengths), and the segments are called range gates. The monitor pulse is used as a reference for subsequent signal processing steps to calculate ranges and correct pulse-by-pulse frequencies. It is necessary to correct frequencies because the pulse-by-pulse frequency jitter of the laser is about 1 MHz (Ishii et al. 2012), corresponding to 1 m s^{-1} at 2 μm, and the goal of velocity performance requires about 0.1 m s^{-1} precision in measurements. The digital signals of backscattered signals and monitor pulses are stored in the PC of the Co2DiaWiL to acquire data, and they are processed in real time using graphics processing units.

The radial wind velocity V_r is calculated as

$$V_r = \frac{\lambda \Delta f}{2} \tag{2.3}$$

with the laser wavelength λ (2.051250 μm) and the Doppler-shifted frequency Δf, which is the difference between the frequencies of backscattered signals and monitor pulses. It is essential to accurately estimate the frequencies of backscattered signals and monitor pulses to achieve highly precise wind measurements. Levin's maximum likelihood discrete spectral peak estimator (Rye and Hardesty 1993; originally presented by Levin (1965) and extended to include spectral accumulation) is used for estimating these frequencies. An algorithm proposed by Frehlich et al. (1997) is used to produce the spectrum of noise-corrected and frequency-corrected backscattered signals at each range gate. The calculations involve four steps:

1) A noise spectrum is produced with the discrete Fourier transform (DFT) from data at the tail of each backscattered signal, where the aerosol signal is negligible. The noise spectrum is accumulated for accurate estimates with K_N pulses.
2) A noise-corrected backscattered signal is produced from the original data sequence of backscattered signals by the whitening algorithm for each lidar pulse. A noise-corrected backscattered signal

spectrum is produced by dividing the DFT of the backscattered signal by the noise spectrum. A noise-corrected backscattered signal is calculated by using the inverse DFT of the spectrum for the noise-corrected backscattered signal.

3) The power spectrum of the monitor pulse is calculated by using a 4096-point DFT. The frequency of the monitor pulse, f_{max}, is that corresponding to the peak of the spectrum, estimated with the maximum likelihood estimator that will be described later. Frequency is corrected pulse by pulse for each lidar pulse using the noise-corrected backscattered signal and frequency of the monitor pulse. This process shifts the zero Doppler-shifted frequency to $f_{max}/4$.
4) The spectrum of the noise-corrected and frequency-corrected backscattered signals is produced with the DFT at each range gate. The spectrum is accumulated for accurate estimates with K_N pulses.

We assume that the spectrum of the monitor pulse and backscattered signal at each range gate has a Gaussian profile, and the spectrum of noise is equal to unity. The spectral model given by Rye and Hardesty (1993) is

$$S(f_i) = \frac{\delta}{(2\pi)^{1/2} f_2} \exp\left[-(f_i - f_1)^2 / (2f_2^2)\right] + 1, \tag{2.4}$$

where S represents an expected value for the spectrum, f_i refers to a frequency normalized to the sampling frequency F_s (500 MHz), $-0.5 \le f_i \le 0.5$, and f_1 and f_2 are the spectral peak and width normalized to F_s, respectively. Here, δ is the wideband signal-to-noise ratio (wideband SNR: ratio of total signal power to noise power over entire spectral bandwidth) and the subscript i indicates the ith spectral component. The maximum likelihood estimator is a promising algorithm to estimate the parameter $\Theta = (\delta, f_1, f_2)$ by maximizing the likelihood function of the spectral data (Rye and Hardesty 1993). The maximum likelihood estimates $\hat{\Theta}$ of the parameters Θ are those values that maximize the following log likelihood function $L(\Theta)$ (Rye and Hardesty 1993):

$$L(\Theta) = C - K_N \sum_{i=1}^{M} \left[P(f_i)/S(f_i, \Theta) - \ln S(f_i, \Theta)\right], \tag{2.5}$$

where C is a constant, M is the total number of spectral estimates, and $P(f_i)$ is the spectrum of the monitor pulse or backscattered signal at each range gate. Here, the spectrum $S(f_i, \Theta)$ is calculated from the spectrum model described in Eq. 2.4. The maximum likelihood estimate $\hat{\Theta}$ is obtained by adjusting Θ until $L(\Theta)$ is maximized. Since the maximum likelihood estimator of signal power (i.e., wideband SNR) cannot be applied to cases of large SNR because of large errors in estimation and numerical instability (Frehlich 1999), wideband SNR is calculated with Eq. 7 of Frehlich et al. (1997).

The accuracy and precision in Doppler velocity measurements of the Co2DiaWiL have been verified by Iwai et al. (2013). Here, bias is the total systematic error in contrast to random error, and precision is the standard deviation of random error. The results of the performance evaluation of the Co2DiaWiL for wind measurements are summarized in Table 2.3.

Table 2.3. Performance evaluation of Co2DiaWiL for wind measurements.

Items	Procedures	Results
Bias	Horizontally fixed beam toward a hard target	-0.0069 m s^{-1}
Random error	Vertically fixed beam	0.12 m s^{-1} (high SNR) 0.4 m s^{-1} (SNR = -15 dB)
Sonic anemometer comparisons	Fixed beam toward a sonic anemometer	correlation coefficient of 0.99 (1-min average time)
Radiosonde comparisons	Horizontal wind velocity retrieved with the velocity azimuth display (VAD) technique	20°-elevation VAD *u*, *v* : correlation coefficients of 0.97 and 0.99 70°-elevation VAD *u*, *v* : correlation coefficients of 0.99 and 0.97

First, the bias in the radial wind velocity measurements of the Co2DiaWiL was investigated to evaluate systematic error in its velocity measurements. The Co2DiaWiL was pointed at the hard target of a stationary building in a range of about 25 km to determine this bias. The bias was calculated from 7200 records of 1-sec averaged radial wind velocities (1-sec average corresponding to 30 laser pulses) starting from 0802 Japan Standard Time (JST) on 12 September 2010 and estimated at –0.0069 m s^{-1} (–0.69 cm s^{-1}), indicating that there was minimal bias in the velocity measurements. The standard deviation of radial wind velocity was 0.081 m s^{-1} (8.1 cm s^{-1}).

Second, random error in the Co2DiaWiL velocity measurements was investigated using the vertically fixed beam mode. The observed standard deviation σ_e of vertical velocity as a function of wideband SNR was evaluated to quantify the random error. Vertical velocity was observed between 0200 and 0400 JST on 23 February 2010. The standard deviation σ_e was calculated from 10-min records of 1-sec averaged vertical velocity by using the velocity-difference method of Frehlich (2001). The theoretical Cramer–Rao lower bound (CRLB) on the standard deviation of radial wind velocity estimate, σ_{CR}, is defined as the following equation from Rye and Hardesty (1993):

$$\sigma_{CR} = \frac{\lambda F_S}{2}\left(\frac{f_2^2}{K_N M}\left\{\int_{-0.5}^{0.5}\frac{(f/f_2)^2}{\left[1+\left(\frac{\delta}{(2\pi)^{1/2} f_2}e^{-f^2/(2f_2^2)}\right)^{-1}\right]^2}df\right\}^{-1}\right)^{1/2}, \tag{2.6}$$

where K_N is the number of accumulated pulses and M is the number of spectral channels. The red circles in Fig. 2.5 are the standard deviations σ_e of vertical velocity estimated by the maximum likelihood method,

for 296 individual, 10-min-long vertical velocity records. The open squares in Fig. 2.5 are standard deviations estimated by the moment method. Here, the σ_e values are plotted versus wideband SNR and compared with the values from the theoretical CRLB calculated from Eq. 2.6. The σ_e values estimated by the maximum likelihood and moment methods are almost the same at a wideband SNR greater than –5 dB. The Co2DiaWiL operates near the theoretical limit under both high and low wideband SNR conditions. Errors are constant (about 0.12 m s^{-1}) in the high-SNR region because of the effect of speckle noise. This noise is derived from the interference of randomly phased backscattered fields from individual aerosol particles, and is independent of wideband SNR. Therefore, speckle noise is the dominant noise source in the high-SNR region (Rye and Hardesty 1993), and it limits the precision of velocity. In the case of using the maximum likelihood method, errors increase with reduced values of wideband SNR, to approximately 0.4 m s^{-1} at a wideband SNR of –15 dB. In the case of using the moment method, errors rapidly increase at a wideband SNR of less than –5 dB.

Third, the radial wind velocities measured with the Co2DiaWiL were compared with the wind speeds measured with a 3-axis ultrasonic anemometer (SONIC SAT-540) mounted on a tower at a height of 59 m AGL to check the fundamental accuracy of the Co2DiaWiL. The term accuracy involves a combination of random components and a bias component. The location for the anemometer was about 120 m south of the Co2DiaWiL. The sonic anemometer measured the three components of wind at a rate of 10 Hz. Wind speed was measured within a range of 0 to 60 m s^{-1}, and with a precision of ±(4% of reading+0.05 m s^{-1}) and a resolution of 0.01 m s^{-1}. The laser beam of the Co2DiaWiL was oriented along an azimuth angle of 191.57° and an elevation angle of 17.94°. The sampling volume was roughly a slant cylinder, 76 m long and 0.08 m in diameter, centered at 153 m from the Co2DiaWiL. The three wind components (u_{SAT}, v_{SAT}, and w_{SAT}) observed using the sonic anemometer were projected onto the direction of the radial wind velocity measured by the Co2DiaWiL with the following equation:

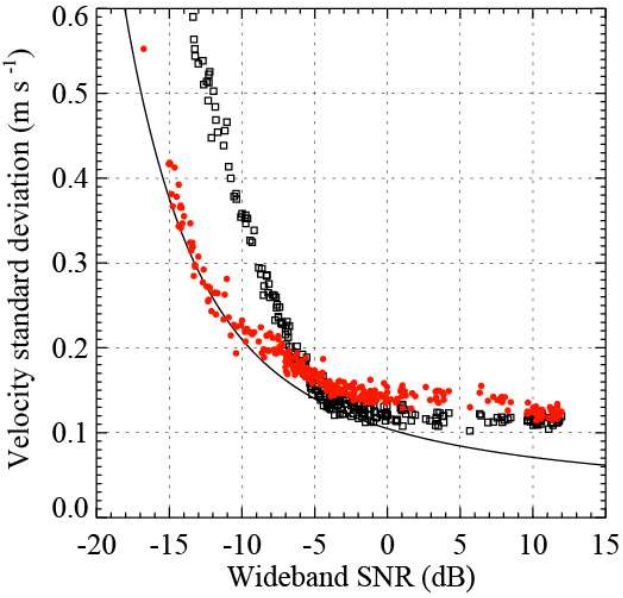

Figure 2.5. Comparison of precision of radial wind velocity of the Co2DiaWiL (red circles and open squares) with theoretical Cramer–Rao lower bound calculated with Eq. 2.6.

$$Vr_{SAT} = u_{SAT}\cos\theta\sin\phi + v_{SAT}\cos\theta\cos\phi + w_{SAT}\sin\theta, \quad (2.7)$$

where Vr_{SAT} is the projected wind speed and ϕ and θ are the azimuth and elevation angles of the Co2DiaWiL laser beam, respectively. Quantitative intercomparisons of 1-min averages between the Co2DiaWiL and a sonic anemometer revealed a correlation coefficient of 0.99. The results reveal that the

two independent wind measurements agree closely, on average, despite the inherent differences between remote, volume-averaged, and point measurements.

Finally, horizontal wind (both *u* and *v* components) under various conditions was determined by comparing the Co2DiaWiL results with conventional radiosonde profiles. 25 Vaisala RS92-SGP radiosondes were used for comparison. The radiosondes were launched from NICT headquarters from 14 February 2010 through 25 February 2010. The radiosonde launch site was about 300 m north-northwest of the Co2DiaWiL. The *u* and *v* components of horizontal wind were computed using changes in GPS location and measured with an accuracy of 0.2 m s^{-1}. The Co2DiaWiL executed 20°-elevation and 70°-elevation conical scans to enable comparison with the radiosondes, and vertical profiles of horizontal wind velocity were retrieved with the velocity azimuth display (VAD) technique described by Browning and Wexler (1968). The VAD technique could retrieve the *u* and *v* components of horizontal wind from radial wind velocity data around horizontal circles centered on the vertical of the lidar scanner. The 20°-elevation and 70°-elevation conical scans took 1 min each to complete, and included about 120 radial wind velocities with 15 pulse accumulations. During a pulse accumulation time of 0.5 sec, the azimuth angle moved through about 3°. The 20°-elevation and 70°-elevation conical scans were carried out alternately. The height resolutions of the conical scans were about 26 m for the former and 72 m for the latter. The intercomparison of *u* and *v* components retrieved from a 20°-elevation conical scan of the Co2DiaWiL and those from radiosondes revealed a correlation coefficient of 0.97 for *u* components and 0.99 for *v* components. The intercomparison of *u* and *v* components retrieved from a 70°-elevation conical scan of the Co2DiaWiL and those from radiosondes revealed a correlation coefficient of 0.99 for *u* components and 0.97 for *v* components.

3. Horizontal convective rolls and near-surface streaks in the sea-breeze layer

In this chapter, we present an observational study on the horizontal convective rolls (HCRs) and near-surface streaks in a convective internal boundary layer (CIBL) formed in the sea-breeze layer. The observation was conducted at Sendai Airport on 18 and 19 June 2007 using two coherent Doppler lidars (CDLs) and a helicopter. On 19 June 2007, the CDLs performed overlapping low-elevation-angle plane position indicator (PPI) scans. The three-dimensional structure of several-hundred-meter-scale HCRs and near-surface streaks was observed using the dual-Doppler lidar. The results of dual-Doppler lidar analysis are compared with those of large-eddy simulations and linear theories. The difference between the wavelengths of the HCRs and near-surface streaks at the north and south of Sendai Airport is discussed. On 18 June 2007, the CDLs performed intersecting range height indicator (RHI) scans. This technique, called “virtual tower”, retrieves vertical profiles of horizontal velocity vectors in the intersecting vertical lines. Spatial variations of vertical wind profiles in the sea-breeze layer and CIBL height at the coastal area could be measured by this technique.

3.1 Introduction

HCRs are counter-rotating horizontal vortices and common features of boundary layer convection (e.g., Brown 1980; Etling and Brown 1993; Atkinson and Zhang 1996; Young et al. 2002). The HCRs form in the convective boundary layer (CBL) with moderately unstable atmospheric condition (e.g., LeMone 1973; Weckwerth et al. 1997). The HCR wavelength and vertical extent are typically scaled by the CBL depth. The orientation of the HCR axes is typically along the mean CBL wind directions. The updrafts and downdrafts of the HCRs provide an efficient means of vertically transporting heat, humidity, and pollutants in the CBL (e.g., LeMone 1976; Weckwerth et al. 1996). Many studies of HCRs have been conducted using linear theories, numerical models, and observations. In particular, the three-dimensional wind fields of kilometer-scale HCRs formed in the CBL have been revealed by dual-Doppler radar observations (e.g., Kropfli and Kohn 1978; Doviak and Berger 1980; Eymard and Weill 1982; Krostivich 1993).

Some previous LES studies (e.g., Deardorff 1972; Moeng and Sullivan 1994; Lin et al. 1996; Khanna and Brasseur 1998; Drobinski and Foster 2003) have shown that the streamwise slow-moving streaks are dominant motions in a neutrally stratified boundary layer. They align with less streaky fast-moving motions and the mean wind near the surface. In a moderately CBL, LES studies (e.g., Deardorff 1972; Sykes and Henn 1989; Moeng and Sullivan 1994; Khanna and Brasseur 1998; Kim and Park 2003) suggest that the HCRs that align with the mean wind are formed by the buoyancy-induced motions in the CBL.

The near-surface streaks, whose wavelength and vertical extent are several hundred meters, are smaller than the often-observed large-scale HCRs that span the entire depth of the boundary layer (Young et al. 2002). The lifetime of streaks is up to 20 min, and a cycle of generation, strengthening, decay, and

reformation repeats. The majority of studies on the streaks have been restricted to numerical simulations owing to their small scale and short lifetime. Recently, Doppler lidars with high spatial and temporal resolution can detect the streaks and measure their properties. Drobinski et al. (2004) and Drobinski et al. (2007) used data from NOAA's High Resolution Doppler Lidar (HRDL; Grund et al. 2001) acquired during CASES-99, to suggest a relationship between the presence of the streaks and the existence of a –1 power law in the velocity fluctuation spectra in the neutral or near-neutral stratified atmospheric surface layer. Newsom et al. (2008) have presented an analysis of dual-Doppler lidar data acquired during Joint Urban 2003, to reveal the structure and evolution of the two-dimensional horizontal velocity fields of the streaks in the surface layer.

We use results from dual-Doppler lidar and heliborne measurements to investigate the three-dimensional structure of the wind field over Sendai Airport and discuss the three-dimensional structure of several-hundred-meter-scale HCRs in the CIBL formed in the sea-breeze layer. Section 3.2 describes the instrumentation used in the study and the dual-Doppler lidar analysis used to retrieve the three-dimensional structure and vertical profiles of the wind field. Section 3.3 presents the data analysis results. A discussion and summary follows in Section 3.4.

3.2 Observation and data analysis

A field investigation on the spatial and temporal structures of the sea breeze around Sendai Airport was conducted in Natori City, Japan (38.14°N, 140.92°E, 5 m mean sea level (MSL)) from 9 to 20 June 2007. From 14 to 19 June, the dual-Doppler lidar observation was conducted using NICT's Doppler lidar and Electronic Navigation Research Institute (ENRI)'s Doppler lidar (Komatsubara and Kaku, 2005). Moreover, the meteorological data at the airport were measured by the heliborne sensors of Japan Aerospace Exploration Agency (JAXA) from 18 to 19 June. The main focus of the present study is on the analysis of the data acquired from the two CDLs and JAXA heliborne sensors on 18 and 19 June.

The specifications of NICT's Doppler lidar (hereafter NICT lidar) are described in Section 2.1. In this study, the radial velocity and signal-to-noise ratio (SNR) in each range were determined as the averages over 50 laser pulses. ENRI's Doppler lidar (hereafter ENRI lidar) is stationed on the rooftop of ENRI's Iwanuma branch building for studying aircraft wake vortices. It operates at a wavelength of 1.54 μm and a PRF of 4 kHz, with a range resolution of 29.9 m and a maximum range of up to 2.5 km. Range-gate radial velocity and SNR were obtained by averaging over 500 pulses. The standard deviations of the radial velocities of the NICT and ENRI lidars are 0.1–0.2 m s^{-1} and 0.5 m s^{-1} at most, respectively. Figure 3.1 shows locations of the NICT and ENRI lidars.

Heliborne in-situ measurements were performed with a research helicopter (MuPAL-ε) of JAXA (Okuno et al. 2002; Matayoshi et al. 2005). The JAXA helicopter was equipped with a three-dimensional ultrasonic velocimeter/thermometer at the tip of the nose boom, pressure transducers connected to pitot-tubes and static pressure holes located at both sides of the forward fuselage, and a hybrid differential Global Positioning System/inertial navigation system. All of the variables were recorded at 40 Hz. The

uncertainties in the wind, temperature, and pressure measurements were approximately 0.1 m s^{-1}, ±1 °C, and ±2 hPa, respectively.

A surface meteorological sensor of the Sendai Aviation Weather Station is composed of a wind sensor and a thermometer. The observed altitudes of the wind sensor and thermometer are 8.3 and 1.5 m above ground level (AGL), respectively. The sampling intervals of the wind sensor and thermometer are 3 and 6 sec, respectively. Surface meteorological data observed using the Automated Meteorological Data Acquisition System (AMeDAS) were also used for the analysis.

Figure 3.1 shows a plan view of the dual-Doppler lidar experimental domain. The *x* direction and *u* component of the wind are parallel to the sea-breeze flow with an azimuth of 135° clockwise from the north, and the *y* direction and *v* component are normal to the sea-breeze flow. The NICT lidar performed 10 sector PPI scans at elevation angles of 0.65°, 1.0°, 1.4°, 1.8°, 2.2°, 2.6°, 3.0°, 3.5°, 4.2°, and 5.0°, in a 120° arc between azimuths 60° and 180°. The ENRI lidar performed 10 full 360° PPI scans at elevation angles from 0.5° to 5.0° in 0.5° increments. The scan rates of the NICT and ENRI lidars were 2° s^{-1} and 6° s^{-1}, respectively. The volume data from each lidar were acquired in 10 min. On 19 June, each lidar performed volume scans every 12 min from 1300 to 1434 JST. The noise-contaminated wind data from each lidar were removed using a threshold level based on the SNR. These edited data from each lidar were interpolated to a three-dimensional Cartesian grid by using a Cressman scheme (Cressman 1959). The horizontal grid spacing was 100 m, and the heights of the horizontal planes were 25, 50, 75, 100, 125, 150, 175, and 200 m AGL. The

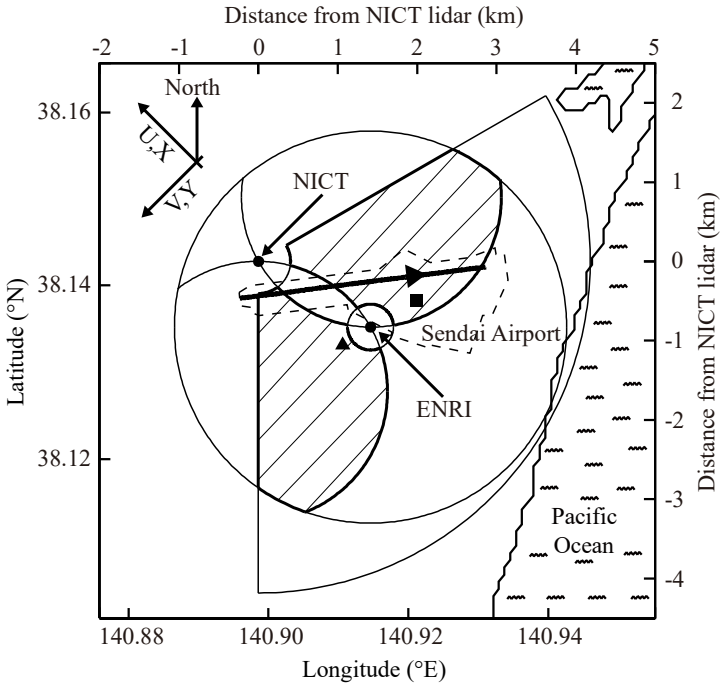

Figure 3.1. Plan view of the dual-Doppler lidar experimental domain. The coordinate system is defined with the NICT lidar located at the origin. The *x*-*y* axes are defined by the arrows in the upper left corner. The hatched areas are the dual-Doppler analysis domains. The borders of Sendai Airport are marked by the dashed line. The flight path of the JAXA helicopter is marked by the thick line over Sendai Airport. The location of the surface meteorological sensor of the Sendai Aviation Weather Station is shown by the black square. The location of the vertical profile of the range-corrected SNR shown in Fig. 3.5b is 135° at 1.5 km from the NICT lidar (displayed by the black triangle).

interpolated velocities at the grid points were combined vectorially to derive the horizontal velocity components u and v. The vertical velocity component w was derived from the upward integration of the anelastic continuity equation with the boundary condition $w = 0$ at the surface. The correction of advection effects is required for the dual-Doppler analysis because the HCRs and streaks have a lateral drift velocity (e.g., Etling and Brown 1993; Drobinski and Foster 2003). A comparison of two consecutive profiles (12-min apart) of the 45°-azimuth radial velocities of the ENRI lidar (mainly cross-stream components) showed that the HCRs and streaks drifted to the northeast at about 0.14 m s^{-1}. Therefore, the correction method introduced by Gal-Chen (1982) was applied to cancel the advection of the HCRs and streaks. The central time of the correction was set as the mid-time of the volume scans.

Figure 3.2 shows the setup of the "virtual tower" (Calhoun et al. 2006) experiment using two CDLs. Between 1300 and 1430 JST on 18 June 2007, the NICT and ENRI lidars performed intersecting RHI scans, and vertical profiles of horizontal velocity vectors in the intersecting vertical lines were retrieved from the radial velocities of the NICT and ENRI lidars. During the experiment, the NICT lidar performed a periodic constant azimuthal RHI at 95° with elevation angles from 0° to 60°. The ENRI lidar performed a series of 6 RHI scans in order to intersect the RHI of the NICT lidar at 6 points. The 6 RHIs had azimuthal angles of –15°, 0°, 15°, 30°, 45°, and 60°. The ENRI lidar scanned with elevation angles from 0° to 90°. The scan rates of the NICT and ENRI lidars were 1° s^{-1} and 1.5° s^{-1}, respectively. The NICT and ENRI lidars took about 1 min to scan from the beginning of an RHI to the beginning of the next RHI. The noise-contaminated wind data from each lidar were removed using a threshold level based on the SNR.

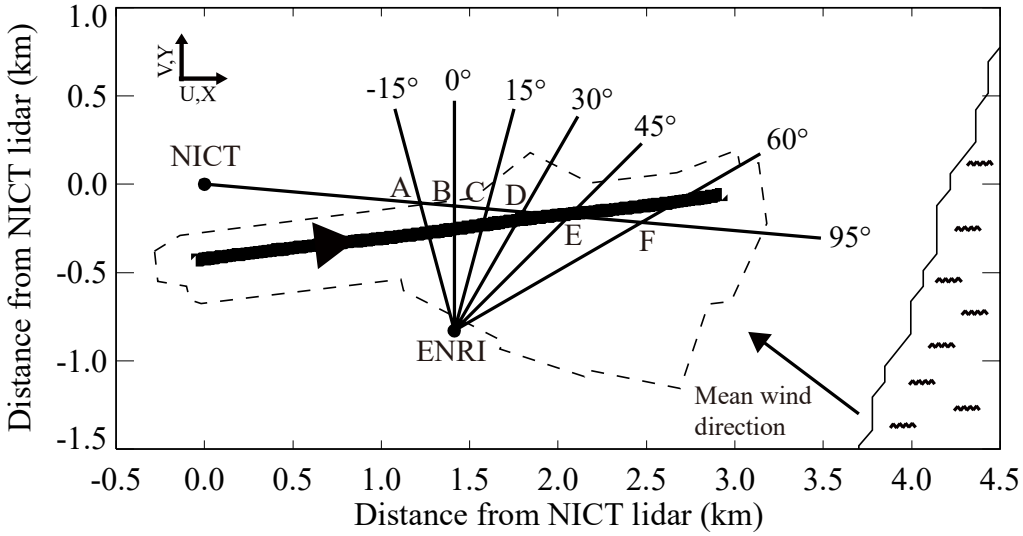

Figure 3.2. Plan view of the dual-Doppler lidar experimental domain. The coordinate system is defined with the NICT lidar located at the origin. The x-y axes are defined by the arrows in the upper left corner. The thin solid lines represent the azimuth direction of the RHI scans of the NICT and ENRI lidars. Alphabetical labels for the intersections are given as A through F in the figure. The borders of Sendai Airport are marked by the dashed line. The flight path of the JAXA helicopter is marked by the thick line over Sendai Airport.

These edited data from each lidar were interpolated to grid points along intersecting vertical lines by using the Cressman scheme. The vertical grid spacing was 25 m. The interpolated velocities at the grid points were combined vectorially to derive the horizontal velocity components *u* and *v*.

3.3 Observed results

3.3.1 Three-dimensional structure of HCRs and near-surface streaks

On 19 June 2007, the thermally induced low-pressure system prevailed over the Japan Islands under fair-weather conditions (not shown). Figures 3.3a–c show the two-hourly surface wind fields and temperature around the Sendai Plain during the daytime on 19 June 2007, obtained from the AMeDAS. The wind fields at 0900 JST (Fig. 3.3a) show the onset of sea breezes at Sendai Airport. At 1100 JST, the sea breeze formed at the Sendai Bay coastal areas and moved inland (Fig. 3.3b). By 1300 JST, the southeasterly sea breeze moved further inland along Sendai Bay (Fig. 3.3c). Cooling by the sea breeze caused a low temperature of 23–25°C at the Sendai Bay coastal areas. Figure 3.4 shows the time series of temperature, dew point, wind speed, and wind direction of the surface meteorological sensor at Sendai Airport. The passage of a sea-breeze front (SBF) was detected at about 0830 JST, which is typical of the statistical meteorological data measured at the Sendai Aviation Weather Station around June. After the sea-breeze frontal passage, a southeasterly sea-breeze flow lasted for the remainder of the daytime.

Figure 3.5a shows vertical profiles of the potential temperature measured by the JAXA heliborne sensors at takeoff (from 0758 to 0814 JST) and landing (from 1000 to 1008 JST). After the sea-breeze frontal passage (0830 JST), a strong capping inversion layer was formed between 150 m and 250 m AGL. This suggests that the cool marine airmass penetrated inland and produced the strong inversion over the Sendai Airport. Figure 3.5b shows the vertical profiles of the range-corrected SNR of the 135°-azimuth

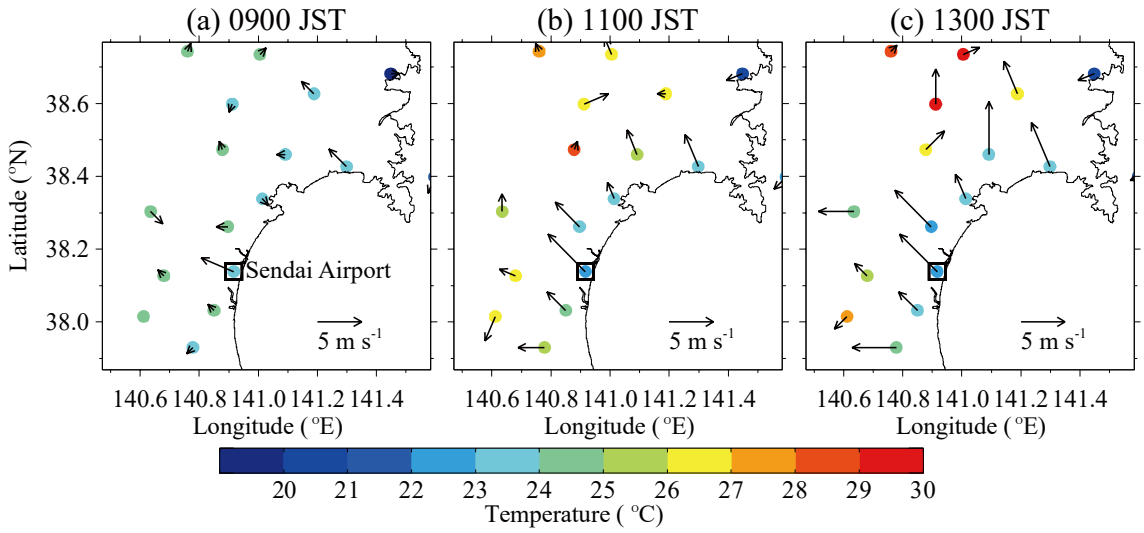

Figure 3.3. Surface wind fields (arrows) and temperature (colored circles) observed by the AMeDAS at (b) 0900 JST, (b) 1100 JST, and (c) 1300 JST on 19 June 2007. The open square indicates the location of the Sendai Airport.

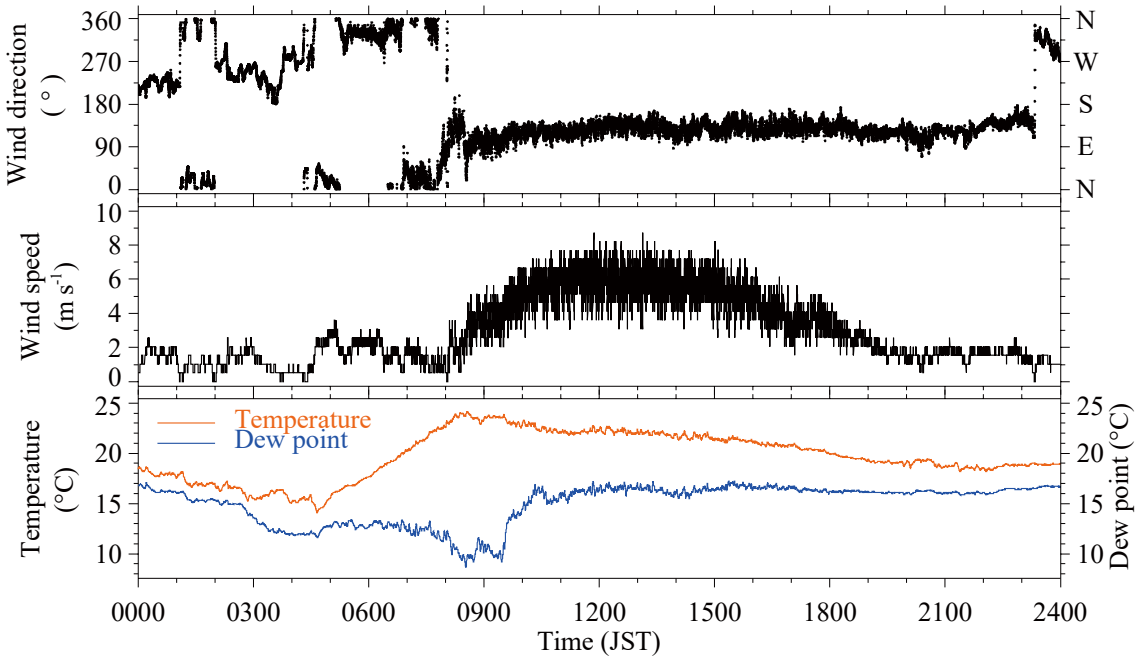

Figure 3.4. Time series of wind direction (°), wind speed (m s^{-1}), temperature (red; °C), and dew point (blue; °C) between 0000 and 2400 JST on 19 June 2007 of the surface meteorological sensor.

(i.e., anti-parallel to the sea-breeze flow) range-height indicator (RHI) scan data of the NICT lidar from 1240 to 1247 JST. The height at which there was a change in the slope of the range-corrected SNR profile was defined as the top of the CIBL (Melfi et al. 1985). Under this definition, the CIBL height z_i was about 220 m. The CIBL height z_i is consistent with the height of the capping inversion layer. Figure 3.5c shows the vertical profiles of the horizontal wind speed and direction obtained using the 20°-elevation velocity azimuth display (VAD) scan (Browning and Wexler 1968) of the NICT lidar from 1221 to 1222 JST and the area-averaged mean wind speed and wind direction retrieved from the dual-Doppler lidar data from 1300 to 1310 JST. Although the wind speed in the CIBL slightly increased during the dual-Doppler lidar observation, the changes in wind direction (about 135°) were small. Although the vertical wind shear in the lowest level (between 25 to 50 m AGL) was approximately 7×10^{-3} s^{-1}, the vertical wind shear in the CIBL was weak (approximately 4×10^{-3} s^{-1}).

The stability parameter z_i/L, where L is the Monin-Obukhov length (Monin and Obukhov 1954), is often used to identify the respective roles played by dynamics and thermal instability in determining the shapes of HCRs and streaks. Here, L was calculated from surface flux measurements using the formulation by Stull (1988),

$$L = -\frac{\overline{\theta_v}\left(\overline{u'w'}_s^2 + \overline{v'w'}_s^2\right)^{3/4}}{\kappa g \overline{w'\theta'_v}_s}, \tag{3.1}$$

where the subscript s represents surface values, θ_v is the virtual potential temperature, $u'w'$ and $v'w'$ are the kinematic momentum fluxes, κ is the von Kármán constant (assumed to be 0.4), g is the gravitational acceleration, and $w'\theta_v'$ is the kinematic buoyancy flux. The surface fluxes were deduced by extrapolating the vertical profiles of the turbulence data measured by the JAXA heliborne sensors just after the helicopter took off from near the ENRI lidar at about 1300 JST, and L was about –123 m. Thus, the stability

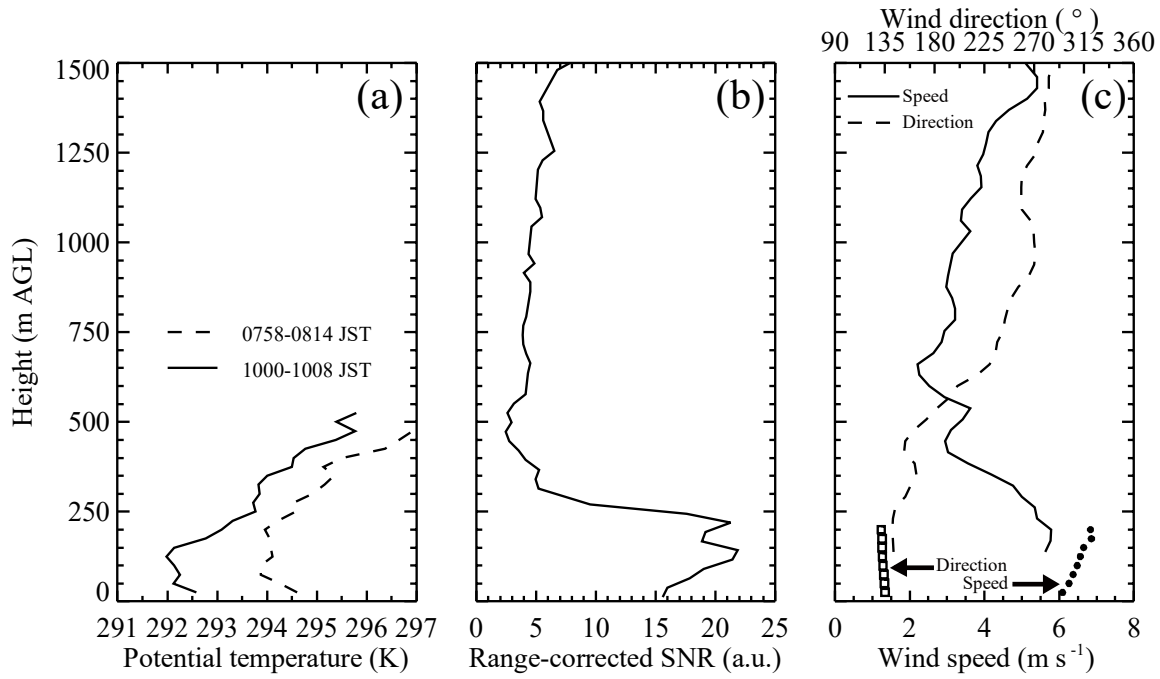

Figure 3.5. (a) Vertical profile of potential temperature measured by the JAXA heliborne sensors at takeoff (from 0758 to 0814 JST on 19 June 2007) and landing (from 1000 to 1008 JST). (b) Vertical profile of range-corrected SNR taken from 135°-azimuth RHI scan data of the NICT lidar from 1240 to 1247 JST. (c) Vertical profile of horizontal wind speed and direction taken from 20°-elevation VAD data of the NICT lidar from 1221 to 1222 JST (solid and dashed lines) and the area-averaged mean wind speed and direction retrieved from the dual-Doppler lidar data from 1300 to 1310 JST (solid circles and open squares).

parameter z_i/L was equal to –1.79, suggesting that the CIBL was slightly unstable.

Figure 3.6 shows the horizontal variability of the radial velocity of the sea-breeze flow near the surface observed by the NICT and ENRI lidars. The southeasterly sea breeze prevailed over the observed region. There are streaky wind perturbations in the mean sea-breeze flow. The direction of the near-surface streaks is approximately parallel to the direction of the mean sea-breeze flow. The near-surface streaks are less organized in the coastal areas, while these structures become clearer over inland areas (Fig. 3.6b). The cross-stream horizontal scale of the near-surface streaky structure is about 400 m (Oda et al. 2010). This structure is very similar to that observed by the NOAA's HRDL (Grund et al. 2001; Drobinski et al. 2004; Drobinski et al. 2007).

Figure 3.7 shows the horizontal cross-sections of perturbations (u', v', and w') from the area-averaged mean wind at 25 m, 50 m, 100 m, and 125 m AGL, retrieved from the dual-Doppler lidar data. It is apparent that there are streaky structures in the streamwise velocity fluctuations u' and the vertical velocity fluctuations w' in the southern region of the dual-Doppler analysis domain; these structures appear elongated in the streamwise direction at near-surface level. The streaks of slow-moving (fast-moving) flows are formed along the upward-moving (downward-moving) regions in the lower level. There are convergence-divergence patterns in the cross-stream velocity fluctuations v' in the same region. The structure is slightly unclear in the northern region of the dual-Doppler analysis domain. The upward and

downward flows gradually strengthen with increasing height, and the convergence and divergence gradually weaken with increasing height. The streamwise extent of the streaky structure was not identified by the dual-Doppler lidar data because the extent was larger than the dual-Doppler lidar analysis domain.

Figure 3.8 shows a vertical cross section of v' and w' components through the straight dashed line A–B indicated in Fig. 3.7a. The cross-stream convergence-divergence patterns of v' and the upward-downward flow patterns of w' at a low level are shown. The HCR structure of the turbulent velocity is indicated by the existence of several counter-rotating vortices.

Figure 3.9 shows the wind velocities and virtual potential temperature measured by the JAXA heliborne sensors for 1 min starting at 1305:37 JST at about 150 m AGL. The helicopter speed was 50 m s^{-1} and the total flight path was 3000 m (Fig. 3.1), with a spatial resolution of about 1.25 m. The JAXA helicopter measurements tended to afford higher streamwise velocities in the regions of downward flow than in the regions of upward flow. This result is consistent with that obtained by the dual-Doppler lidar observations. The updrafts (downdrafts) largely coincide with the perturbations of high virtual potential temperature (low virtual potential temperature). The upward-downward flow pattern is generally spaced over several hundreds of meters. Therefore, it is suggested that the CIBL convection has a HCR-scale mode. The mean streamwise momentum flux ($\overline{u'w'}$) and thermodynamic fluxes ($\overline{w'\theta_v'}$) are calculated by filtering the data to the HCR scale (bold lines in Fig. 3.9) at –0.297 m^2 s^{-2} and 0.032 K m s^{-1}, respectively. The momentum and thermodynamic fluxes account for four-fifths and two-thirds of the fluxes calculated from the total perturbation quantities (thin lines in Fig. 3.9), respectively. The vertical turbulent transport

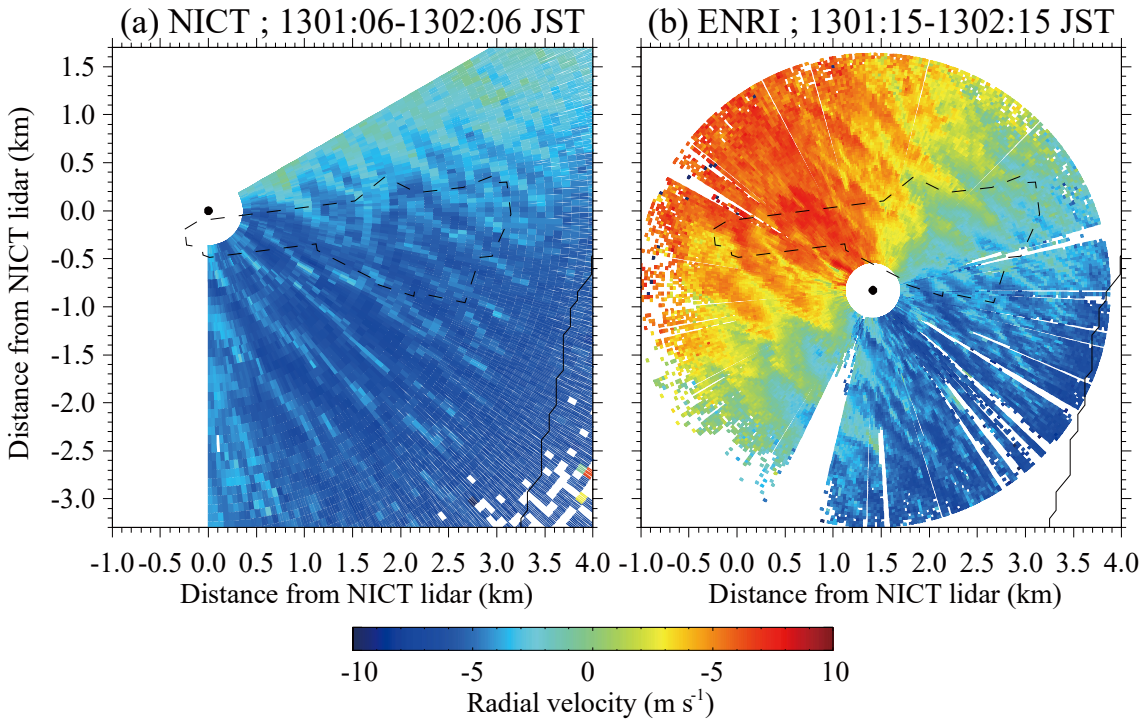

Figure 3.6. (a) NICT lidar 1°-elevation sector PPI scan and (b) ENRI lidar 1°-elevation PPI scan of radial velocity (color bar in m s^{-1}) from 1301 to 1302 JST on 19 June 2007. Negative velocities, represented in blue, indicate flow toward each lidar. Positive velocities, represented in red and yellow, indicate flow away from each lidar. The borders of Sendai Airport are marked by the dashed line.

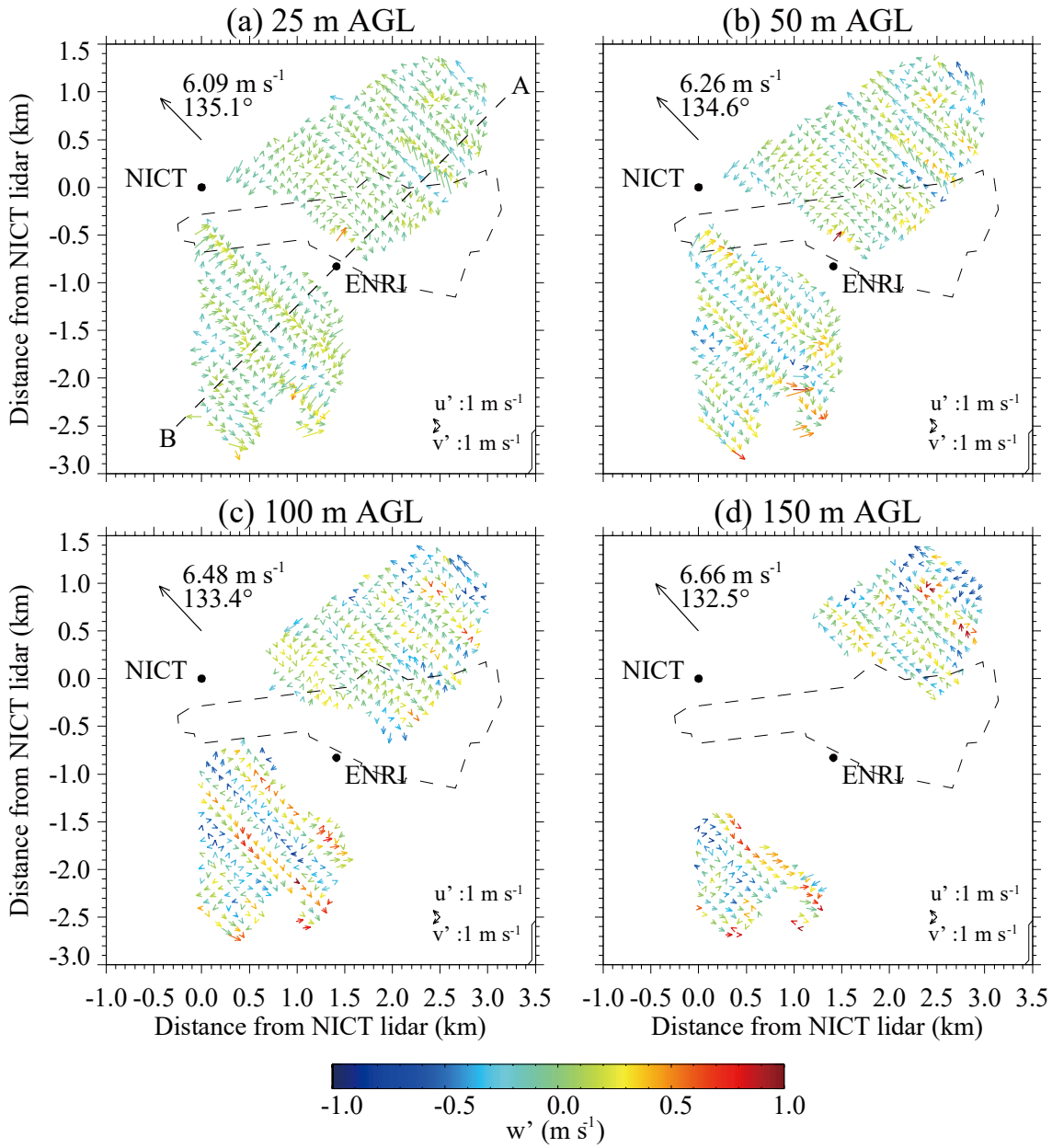

Figure 3.7. Horizontal cross sections of perturbation wind fields retrieved from the dual-Doppler lidar data from 1300 to 1310 JST on 19 June 2007. The horizontal wind perturbations *u'* and *v'* are displayed by arrows and the vertical wind perturbation *w'* is displayed in color. The arrows in the upper left-hand corners of each panel indicate the area-averaged mean wind. The straight dashed line A-B in Fig. 3.7a is the location of the vertical cross section in Fig. 3.8.

of momentum and heat within the CIBL is dominated by HCR convection. Figure 3.9a shows that the updrafts and downdrafts are asymmetric. There are locally restricted updrafts and more extended weaker downdrafts. This asymmetric pattern was identified by the laboratory experiment (Deardorff et al. 1969) and LES study (Raasch and Harbusch 2001).

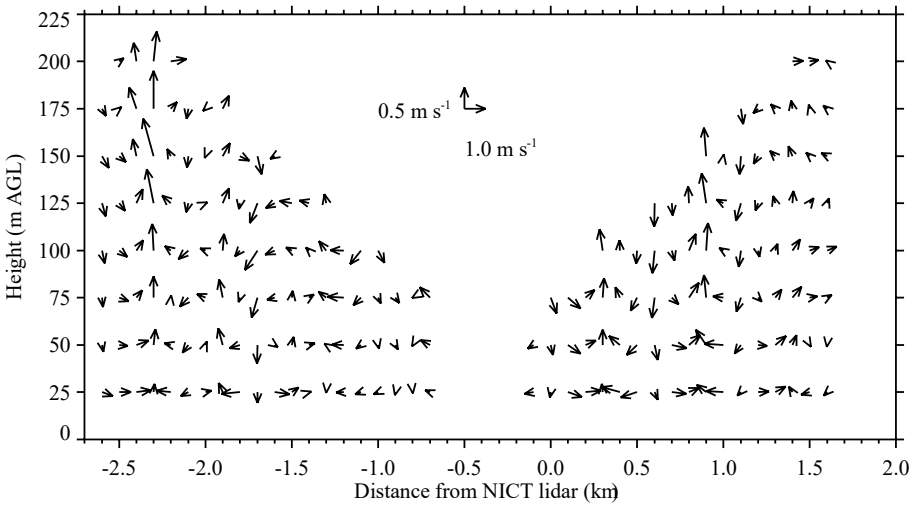

Figure 3.8. Vertical cross section display of *v'* and *w'* components through the straight dashed line indicated in Fig. 3.7a.

Figure 3.10 shows the power density spectra of the vertical wind velocity perturbations of the dual-Doppler lidar and JAXA helicopter. The power density spectra of *w'* in the northern and southern regions of the dual-Doppler analysis domain (Fig 3.10a) showed peaks at wavelengths of about 450 m and 550 m, respectively. In Fig. 3.10b, there are three peaks at about 370 m, 500 m, and 750 m wavelengths. Since the cross angle between the helicopter flight path and the *y* axis was about 38°, the wavelengths obtained from the heliborne measurements were 1.27 (i.e., $(\cos 38°)^{-1}$) times as long as those observed from the dual-Doppler lidar observations. Although there was a difference between the temporal and

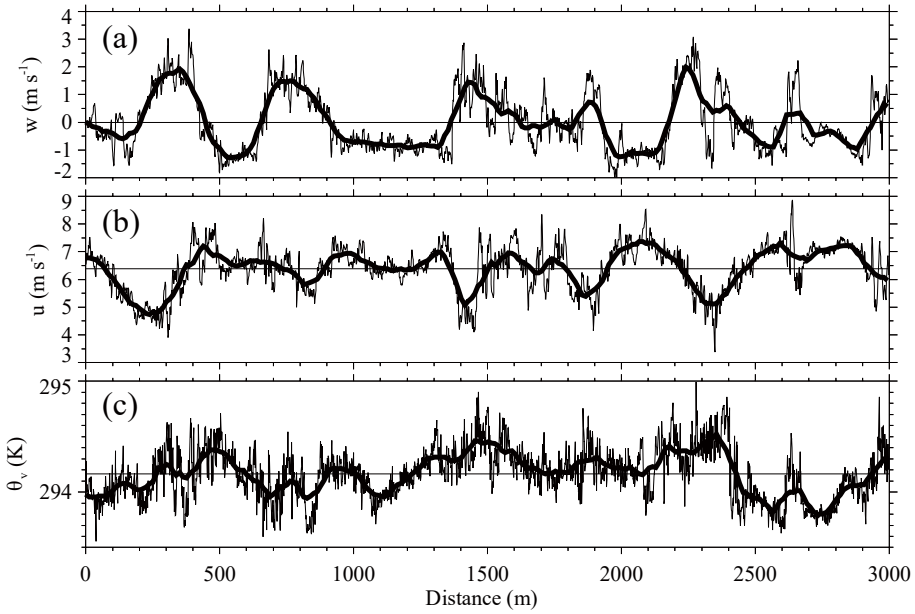

Figure 3.9. Time series of (a) vertical velocity w (m s^{-1}), (b) streamwise velocity u (m s^{-1}), and (c) virtual potential temperature θ_v (K) measured by the JAXA heliborne sensors for 1 min starting at 1305:37 JST on 19 June 2007 at about 150 m AGL. The straight line in each panel is the mean value. The bold line in each panel is a smoothed series by a running window of 100 m.

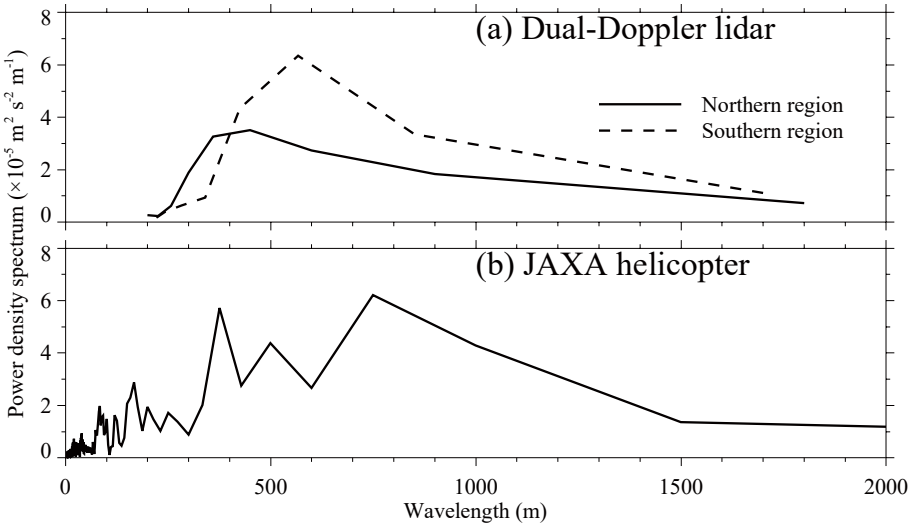

Figure 3.10. Power density spectrum of vertical velocity fluctuations *w'* of (a) dual-Doppler lidar and (b) JAXA helicopter. The spectrum in Fig. 3.10a is calculated at 75 m AGL in the vertical cross section shown by Fig. 3.8. The solid and dashed lines indicate the spectra of the northern and southern regions of the dual-Doppler lidar analysis domain displayed in Fig. 3.1. The spectrum in Fig. 3.10b is calculated from the JAXA helicopter data shown by Fig. 3.9a.

spatial resolutions of the dual-Doppler lidar and the JAXA helicopter measurements, the wavelengths observed by the JAXA helicopter roughly agreed with those observed by the dual-Doppler lidar. The vertical wind velocity perturbations with 370 m wavelengths observed by the JAXA helicopter were not observed by the dual-Doppler lidar, probably because of its lower spatial resolution.

3.3.2 Spatial variations of vertical wind profiles in the sea-breeze layer

Figures 3.11a–c show the two-hourly surface wind fields and temperature around the Sendai Plain during the daytime on 18 June 2007, obtained from the AMeDAS. At 0900 JST, the onset of sea breezes was observed at Sendai Airport (Fig. 3.11a). At 1100 JST, the sea breeze formed at the Sendai Bay coastal areas (Fig. 3.11b). By 1300 JST, the southeasterly sea breeze penetrated inland along Sendai Bay (Fig. 3.11c). The sea breeze flow was weaker than that observed on 19 June 2007. Figure 3.12 shows the time series of temperature, dew point, wind speed, and wind direction of the surface meteorological sensor at Sendai Airport. Between 0730 and 0900 JST, the wind direction shifted gradually from north to southeast. The passage of an SBF was unclear. After 0900 JST, a weak southeasterly sea-breeze flow lasted for the remainder of the daytime.

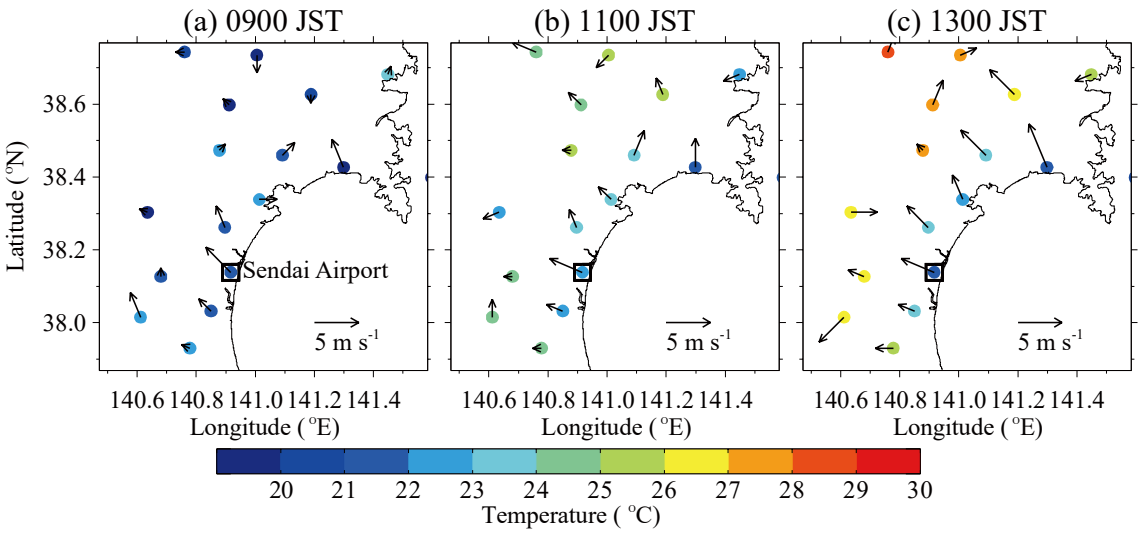

Figure 3.11. Surface wind fields (arrows) and temperature (colored circles) observed by the AMeDAS at (b) 0900 JST, (b) 1100 JST, and (c) 1300 JST on 18 June 2007. The open square indicates the location of Sendai Airport.

Figure 3.13a shows a vertical profile of the virtual potential temperature measured by the JAXA heliborne sensors at takeoff (from 1300 to 1314 JST). A strong capping inversion layer was formed between 300 m and 350 m AGL, and the CIBL height z_i was estimated as about 325 m AGL. The JAXA helicopter passed through the inversion layer at 4 km inland from the coastline. This suggests that the cool marine airmass penetrated inland and produced the strong inversion over Sendai Airport. Figure 3.13b shows the vertical profiles of the horizontal wind speed and wind direction measured by the JAXA heliborne sensors. The sea-breeze layer with the weak southeasterly flow was evident up to the CIBL

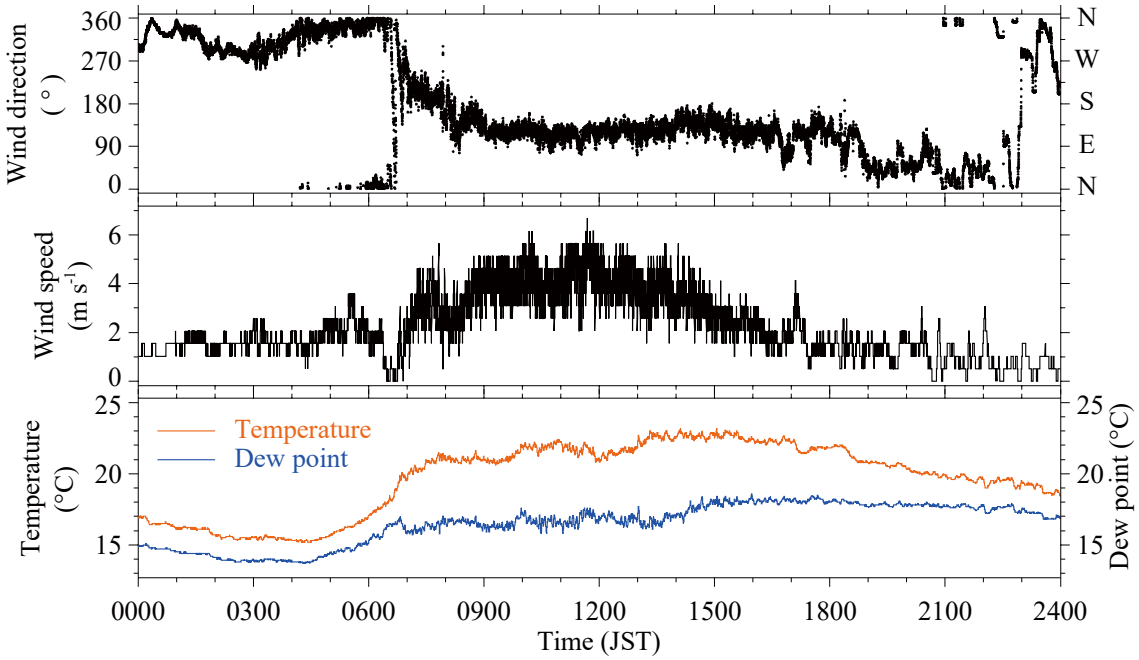

Figure 3.12. Time series of wind direction (°), wind speed (m s^{-1}), temperature (red; °C), and dew point (blue; °C) between 0000 and 2400 JST on 18 June 2007 of the surface meteorological sensor.

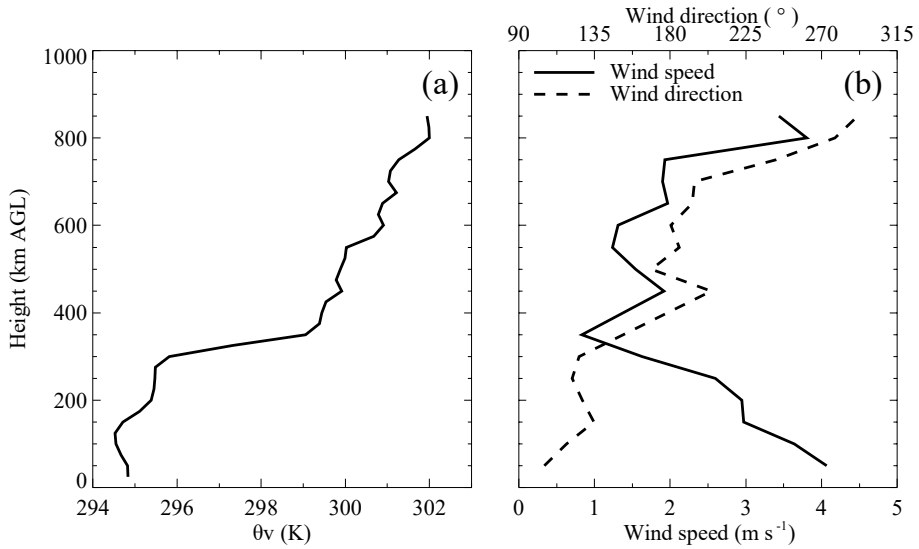

Figure 3.13. (a) Vertical profile of virtual potential temperature and (b) vertical profiles of horizontal wind speed and direction (solid and dashed lines) measured by the JAXA heliborne sensors at takeoff (from 1300 to 1314 JST on 18 June 2007).

height. Between 400 and 700 m AGL, there was a weak southerly flow. Above 700 m AGL, the wind direction shifted from south to west and the wind speed increased with height. The surface fluxes were deduced by extrapolating the vertical profiles of the turbulence data measured by the JAXA heliborne sensors just after the helicopter took off from near the ENRI lidar at about 1300 JST, and L was about –42.3 m. The stability parameter z_i/L was –7.69, suggesting that the CIBL was unstable.

Figure 3.14 shows the wind velocities and virtual potential temperature measured by the JAXA heliborne sensors for 54.36 sec starting at 1410:40 JST at about 210 m AGL. The helicopter speed was 55.2 m s^{-1} and the total flight path was 3000 m (Fig. 3.2), with a spatial resolution of about 1.38 m. There is a different tendency in the vertical velocity data in segment A, compared with that in segment B. In segment A, the upward-downward flow pattern is generally spaced over about 500 m. The updrafts (downdrafts) largely coincide with the perturbations of high virtual potential temperature (low virtual potential temperature). The streamwise slow-moving (fast-moving) flows are formed in the upward-moving (downward-moving) regions. Therefore, it is suggested that the CIBL convection has an HCR-scale mode. The standard deviation σ_w of vertical velocity was larger in segment A than in segment B. It is suggested that the atmosphere in segment B was stable and segment B was outside of the CIBL. The streamwise wind speed in segment B (about 5 m s^{-1}) was higher than that in segment A (3–4 m s^{-1}).

Figure 3.15 displays radial velocity data of nearly simultaneous RHI scans for both the NICT and ENRI lidars from 1401 to 1402 JST. The RHI scans intersected at intersection A (Fig. 3.2). The depth of the sea-breeze flow was estimated as about 400 m from the NICT lidar data (Fig. 3.15a). The radial velocity of the ENRI lidar changed considerably at about 250 m AGL. This suggests that the wind direction changed considerably at 250 m AGL. The height of the JAXA helicopter (210 m AGL) at 1410:40 JST was below the wind shear layer. Figure 3.16 shows the radial velocity data of RHI scans intersecting at intersection E from 1406 to 1407 JST. The depth of the sea-breeze flow was the same as that

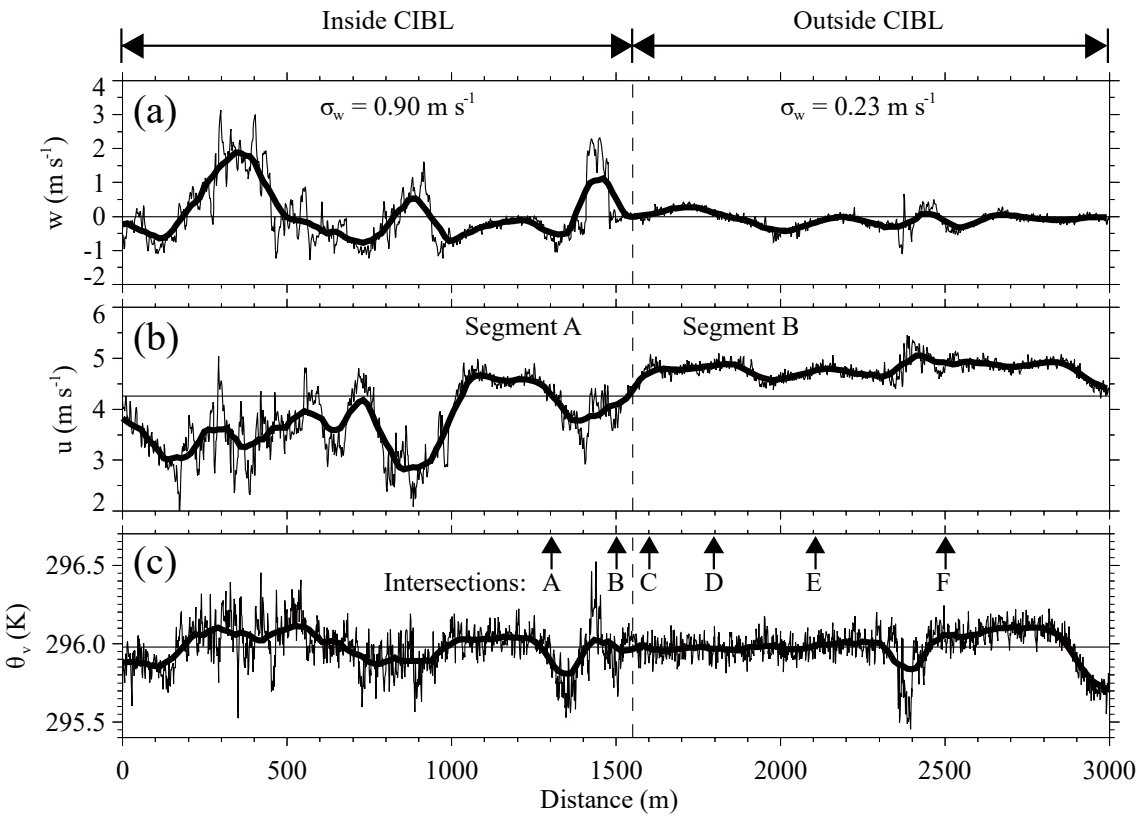

Figure 3.14. Time series of (a) vertical velocity w (m s^{-1}), (b) streamwise velocity u (m s^{-1}), and (c) virtual potential temperature θ_v (K) measured by the JAXA heliborne sensors for 54.36 sec starting at 1410:40 JST on 18 June 2007 at about 210 m AGL. The horizontal straight line in each panel is the mean value. The bold line in each panel is a smoothed series by a running window of 100 m.

estimated in Fig. 3.15a. The azimuth direction of the ENRI lidar's RHI scan was nearly perpendicular to the mean sea-breeze flow (Fig. 3.2). Figure 3.16b shows the cross-stream convergence-divergence patterns of radial velocity below 50 m AGL and several counter-rotating vortices with a depth of about 200 m. This suggests the existence of the HCRs in the CIBL.

Figure 3.17 shows the vertical profiles of the horizontal wind speed and wind direction obtained at intersections A through F from 1401 to 1408 JST. The differences between the wind direction profiles are small. There is a wind speed difference of 1–2 m s^{-1} between the most-upwind (intersection F) and most-downwind (intersection A) profiles below 200 m AGL. This is consistent with the change in streamwise wind speed measured by the JAXA heliborne sensors (Fig. 3.14b). As mentioned in Section 1.1, the CIBL height is proportional to the square root of the downwind distance from shore (e.g., Venkatram 1977; Raynor et al. 1979). The CIBL height estimated from the vertical profiles of the horizontal wind speed is displayed in Fig. 3.17 (dash-dotted line).

3.4 Discussion and summary

HCRs and streaks were observed by dual-Doppler lidar and heliborne sensors in a shallow (z_i = 220 m) and slightly unstable (z_i/L = –1.79 state) CIBL on 19 June 2007. The near-surface horizontal cross section of the perturbation wind fields measured by the dual-Doppler lidar indicated streaky structures of u' and w' and convergence-divergence patterns of v', which were elongated in the streamwise direction. Generally, regions of upward (downward) flows coincided with regions of negative (positive) u' at the lower level. The vertical cross sections of the v' and w' components in the cross-stream direction showed that the upward regions of the HCRs agreed with the upward motions of the streaks. These structures are consistent with the results of the LES study by Khanna and Brasseur (1998). Khanna and Brasseur (1998) argued that coherent sheetlike updrafts form the upward regions of HCRs and they originate near the surface in the streamwise low-speed streaks under moderately convective conditions (i.e., states z_i/L = –3 and –8).

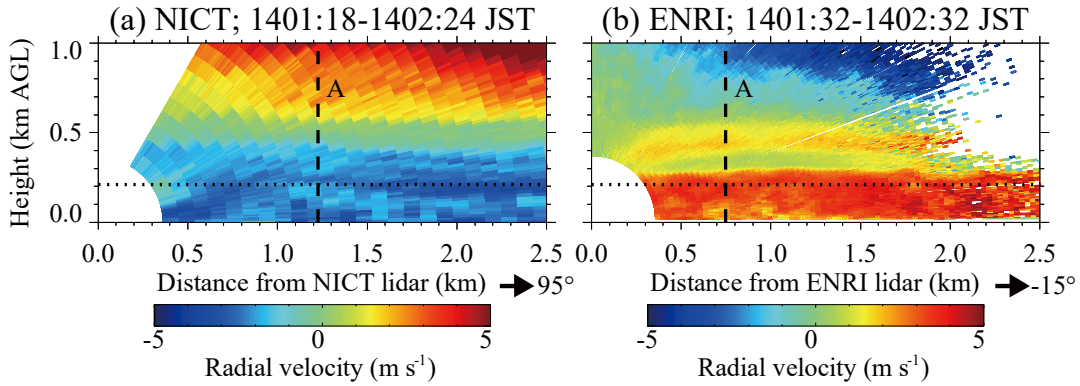

Figure 3.15. (a) NICT lidar 95°-azimuth RHI scan and (b) ENRI lidar –15°-azimuth RHI scan of radial velocity (color bar in m s^{-1}) from 1401 to 1402 JST on 18 June 2007. Negative velocities, represented in blue, indicate flow toward each lidar. Positive velocities, represented in red and yellow, indicate flow away from each lidar. The vertical dashed lines indicate the location of the intersecting vertical column at intersection A. The horizontal dotted lines indicate the height of the JAXA helicopter (210 m AGL) at 1410:40 JST.

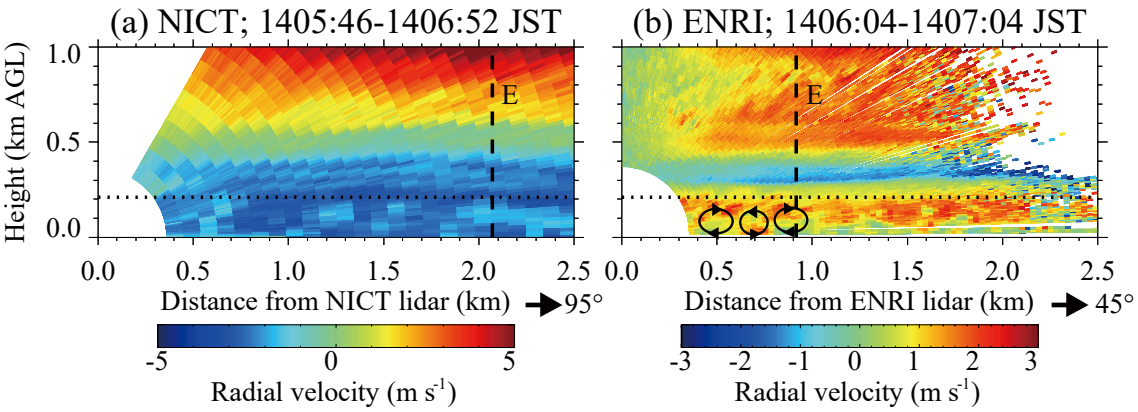

Figure 3.16. (a) NICT lidar 95°-azimuth RHI scan and (b) ENRI lidar 45°-azimuth RHI scan of radial velocity (color bar in m s^{-1}) from 1406 to 1407 JST on 18 June 2007. The vertical dashed lines indicate the location of the intersecting vertical column at intersection E. The horizontal dotted lines indicate the height of the JAXA helicopter (210 m AGL) at 1410:40 JST.

The spacing between the HCRs (wavelength) observed by the dual-Doppler lidar was 450–550 m, which was supported by the JAXA helicopter data, and the height of the CIBL was about 220 m. Thus, the aspect ratio was 2.05–2.50, which is close to the value (2.83) predicted by linear theories (e.g., Kuettner 1971). Weckwerth et al. (1997) observed the HCRs with wavelengths longer than 1 km and boundary-layer heights larger than 500 m and derived empirical linear regressions between the wavelength and the boundary-layer height. If smaller-scale HCRs were observed in their experiment, our results would probably agree with these linear approximations.

There is a difference between the wavelengths of the HCRs and streaks to the north and south of Sendai Airport. Although cultivated land is found to the north of the airport, an industrial complex exists to the south. Kropfli and Kohn (1978) suggested that the buoyancy resulting from urban heat islands affects the HCR structure. Lin et al. (1997) demonstrated by LES that the structure of streaks is affected by surface roughness. Thus, the difference between the structures of the HCRs and streaks may be explained in terms of surface-heating conditions and surface roughnesses. It is, however, very difficult to verify the effects of these parameters on the structures of HCRs and streaks using only limited observational data.

Using a building-resolving computational fluid dynamics (CFD) model nested in an advanced forecast system with a data assimilation scheme, Chen et al. (2015a) succeeded in reproducing the HCRs observed in this case realistically. The characteristics of the reproduced HCRs agreed well with those

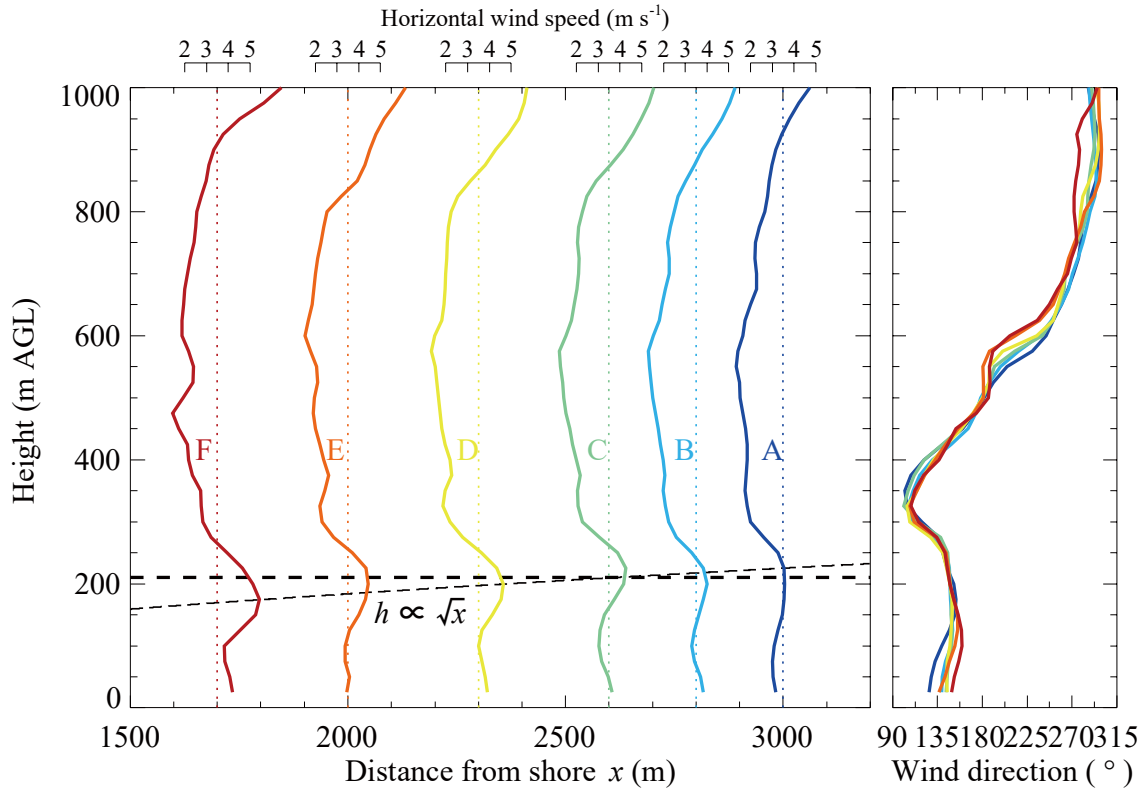

Figure 3.17. Vertical profiles of horizontal wind speed and direction obtained at intersections A through F from 1401 to 1408 JST on 18 June 2007. The horizontal dotted lines indicate the height of the JAXA helicopter (210 m AGL) at 1410:40 JST. The dash-dotted line indicates the estimated CIBL height.

observed by dual-Doppler lidar and heliborne sensors. Moreover, Chen et al. (2015b) conducted several sensitivity experiments to investigate the impacts of land use and buildings on HCRs using the same CFD model. Chen et al. (2015b) clarified that variations in land use and the presence of buildings affected the positions, intensities, and structures of HCRs.

On 18 June 2007, the CDLs performed intersecting RHI scans, and vertical profiles of horizontal velocity vectors in the intersecting vertical lines were retrieved. Spatial variations of the vertical wind profiles in the sea-breeze layer at the near-shore coastal area could be measured by this technique. The CIBL height estimated from vertical profiles of horizontal wind speed was roughly proportional to the square root of the downwind distance from shore. The ENRI lidar's RHI scan perpendicular to the mean sea-breeze flow showed the existence of the HCRs in a shallow and unstable (z_i/L = –7.69 state) CIBL.

4. STRONG UPDRAFT AT A SEA-BREEZE FRONT AND ASSOCIATED VERTICAL TRANSPORT OF NEAR-SURFACE DENSE AEROSOL

In this chapter, we present an observational study on a strong updraft at a sea-breeze front (SBF) and the associated vertical transport of a near-surface dense aerosol occurred in the Tokyo metropolitan area. The observation was conducted on 27 May 2008 using NICT's Doppler lidar, a collocated ceilometer, and an in-situ surface meteorological sensor. The vertical and horizontal wind structures at and around the SBF penetrating from Sagami Bay were observed by the Doppler lidar. A modified two-dimensional variational method to retrieve the updraft from the Doppler lidar radial velocities is described. The hypothesis that the observed SBF is the leading edge of a density (or gravity) current is verified by using Doppler lidar and in-situ surface meteorological sensor data. The relation between the updraft and vertical aerosol transport over the nose of the SBF is discussed by using observed results of the Doppler lidar and ceilometer. The effect of the interaction between the SBF and the prefrontal thermal on the formation of the updraft is also discussed.

4.1 Introduction

Metropolitan Tokyo comprises a mega-city, with about 35 million inhabitants. Facing the Pacific Ocean, through Tokyo Bay and Sagami Bay, it is frequently under the influence of a sea-breeze circulation (SBC), mainly during the summer. In order to investigate the local wind system and the influence of air pollution, the Japan Meteorological Agency (JMA) and the Environment Agency conducted intensive observations of the lower atmosphere (below 2 km) over the southern Kanto Plain using pilot-balloons and radiosondes from 1974 to 1976. Analyzing the observed data, Fujibe and Asai (1979) found that the land and sea breeze over the Kanto Plain was classified into two types: small-scale wind system and regional-scale wind system. The small-scale wind system is corresponding to the small-scale sea breeze around noon. In the afternoon, the regional-scale wind system (sea breeze) with a horizontal scale of about 200 km and a vertical extent of 1–1.5 km covers the whole Kanto Plain (Fujibe and Asai 1984). The regional-scale sea breeze plays an important role in the long-range transport of pollutants from the coastal region to the inland region (e.g., Kurita et al. 1990). However, the field measurements of the vertical transport of pollutants at the SBF have been rare in the Tokyo metropolitan area.

There have been several studies of interactions between sea breezes and urban heat islands (UHIs) in the Tokyo metropolitan area. Yoshikado (1990) and Yoshikado (1992) found that the vertical velocity at the SBF and the vertical scale of the SBC were increased due to interactions between sea breezes and the heat-island circulation induced by the UHI. The inland penetration speed of the sea breeze initially increased rapidly and then decreased because of the interactions. The SBFs that penetrate to the Tokyo metropolitan area are also known as a key factor in cumulus convection initiation. For example, it is

known that a cumulus cloud line formed just above the Kanpachi Street during calm summer conditions. The cumulus cloud line generally formed over a convergence zone of SBFs moving inland from Tokyo Bay and Sagami Bay (Kai et al. 1995; Kanda et al. 2001). The width of the cloud line is about 500 m, with the cloud-base height of about 500 m and the cloud-top height of about 800 m.

The updraft at the SBF is an important factor in the vertical transport of pollutants and cumulus convection initiation. The magnitude of the updrafts at the SBF depends on the intensity of gradients at the front zone and the speed and direction of the ambient flow (Helmis et al. 1987). As mentioned in Chapter 1, the interactions between the SBF and other meteorological phenomena have a crucial contribution to variations in the SBF structure. When the SBF interacts with horizontal convective rolls (HCRs), the strong updrafts form at the SBF (Wakimoto and Atkins 1994; Atkins et al. 1995). The interactions between the SBF and the pre-frontal convective cells with a horizontal scale of a few kilometers have a crucial influence on the SBF structure. By using a two-dimensional numerical model, Ogawa et al. (2003) showed that when the SBF approaches the updraft region of the convective cell, the vertical velocity at the SBF is intensified.

The fine-scale structure (several 100-m scale) of SBFs in the Tokyo metropolitan area has not been revealed since the observation techniques, such as pilot-balloons and radiosondes used in many previous studies (e.g., Yoshikado and Kondo 1989; Yoshikado 1990), have provided poor horizontal sampling. Nakane and Sasano (1986) used backscatter data from scanning aerosol lidar to observe the fine-scale structure of an SBF as it moved inland from the Pacific Ocean, but the lidar did not directly observe wind velocity. Ohno and Suzuki (1993) using a Doppler radar have shown the fine-scale structure of an SBF as it moved inland from the Pacific Ocean. But the performance of radar is not optimal for observing the near-surface wind structure of SBFs due to ground clutter from buildings in dense urban areas. Aircraft measurements are widely recognized as providing detailed information on the SBFs with high spatial resolution (several meters along the flight track) (e.g., Kraus et al. 1990; Finkele et al. 1995; Stephan et al. 1999; Wood et al. 1999), but there are restrictions on research aircraft measuring low-level meteorological data over dense urban areas such as Tokyo.

In this case study, we illustrate the vertical and horizontal wind structure, and the temporal evolutions, of an SBF and the SBF-related vertical aerosol transport over the Tokyo metropolitan area. This study utilizes data collected on 27 May 2008 from NICT's Doppler lidar, a ceilometer, and an in-situ surface meteorological sensor. Section 4.2 describes the instrumentation used in the study. Section 4.3 describes the method used to retrieve the vertical air motion from Doppler lidar data on vertical scans. Section 4.4 presents the data analysis results, with discussion provided in Section 4.5 and a summary in Section 4.6.

4.2 Observational data

Using NICT's Doppler lidar (hereafter Doppler lidar), observations of the wind field within the atmospheric boundary layer (ABL) were performed from 14 May to 15 June 2008 at the NICT headquarters (35.71°N, 139.49°E, height 75 m above mean sea level; denoted by the black square in Fig.

4.1) located in the Tokyo metropolitan area. The Doppler lidar was stationed on the rooftop of a building at the NICT headquarters (23 m above ground level (AGL)). The specifications of the Doppler lidar are described in Section 2.1. In this study, the radial velocity and signal-to-noise ratio (SNR) in each range were determined as the averages over 50 laser pulses. In this experiment, the Doppler lidar range gates had a length of about 153 m with the first gate's center at 537 m. With 63 range gates per beam, the maximum range was about 10 km. The Doppler lidar performed range height indicator (RHI) scans along the north-south and east-west, plane position indicator (PPI) scans at an elevation angle of 1°, 20°-elevation and 70°-elevation velocity azimuth display (VAD) scans (Browning and Wexler 1968), and zenith stares. The scan rate and angular resolution of RHI/PPI scans were 1° s^{-1} and 1°, respectively. The RHI scans showed the vertical structure of the sea-breeze flow from the surface to several kilometers (usually 1–3 km) above the surface. The PPI scans provided information about the horizontal variability of the sea-breeze flow. Since it took 3 and 6 min for each RHI and PPI scan, respectively, the observed SBF had travelled 1–2 km during the scanning time. The 20°-elevation and 70°-elevation VAD scans were used to determine the vertical profiles of the horizontal wind velocity above 184 m AGL. The zenith stares provided vertical wind velocities above 537 m AGL, meaning that they observe the updraft over the nose of the SBF (see Fig. 4.8). The Doppler lidar data were acquired by a computer whose time was synchronized by the network time protocol (NTP).

A Vaisala single-lens ceilometer CT25K was deployed on the ground and placed about 50 m north-west of the Doppler lidar. The ceilometer is used primarily for the retrieval of cloud heights, but also for boundary-layer studies based on its demonstrated ability to provide vertical profiles of backscatter light intensity from particulate matter in the lower troposphere (e.g., Emeis et al. 2004; Münkel et al. 2007). It measures the optical backscatter coefficient of the air at a wavelength of 905 nm by a built-in algorithm (Vaisala 1999). To calibrate the backscatter coefficient, a correction factor was calculated by comparison

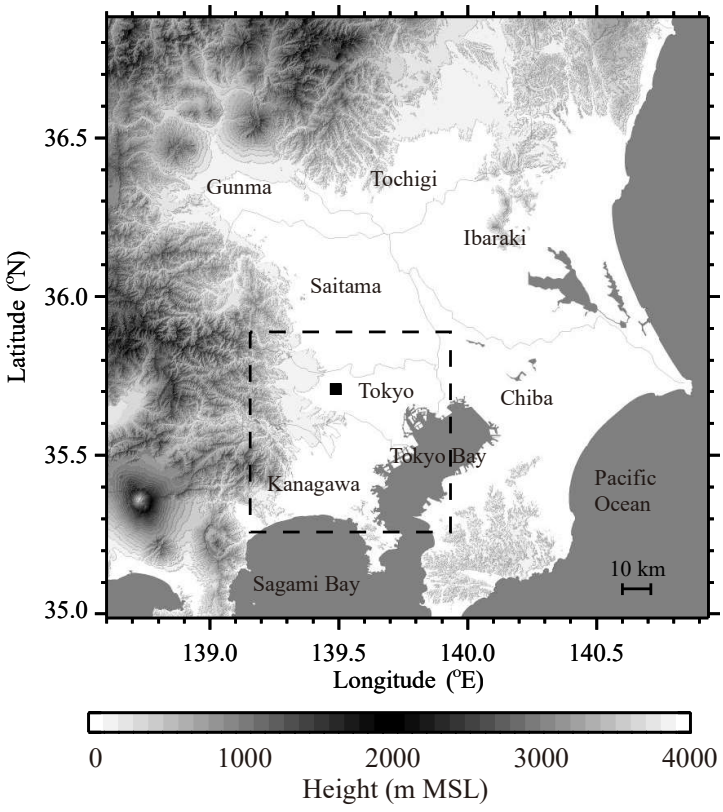

Figure 4.1. Map and topography of the Kanto District. The black square indicates the location of the NICT headquarters. The grayscale bar shows the height of the topography in m MSL. The dashed rectangle delineates the area displayed in Fig. 4.6.

with a 532-nm Mie lidar and ceilometer observations of dense clouds (M. Yasui, NICT, personal communication, 2010). It was assumed that the wavelength dependence of the backscatter coefficient was nearly negligible since the backscattering was in the geometric optical region where the wavelengths of the Mie lidar and ceilometer were much smaller than the particle diameter at dense clouds. The Mie lidar was placed about 6 m north-east of the ceilometer and its backscatter coefficient was calibrated by a method described in Yasui et al. (2005). For the ceilometer, the wavelength of the transmitted beam is on the same order as the scattering particle matter (e.g., aerosol, fog, mist, cloud, and precipitation). Therefore, Mie backscattering is the dominant mechanism producing the scattering. The ceilometer can retrieve cloud heights every 15 sec up to 7.5 km above the ground with a vertical resolution of 30 m. The minimum measurable vertical visibility is 30 m.

A Vaisala WXT510, deployed on the building roof (18 m AGL), is an in-situ surface meteorological sensor for measuring wind speed and wind direction, liquid precipitation, barometric pressure, temperature, and relative humidity. Data are recorded every 1 min. This study utilizes the data on wind speed, wind direction, temperature, relative humidity, and barometric pressure. Wind speed is measured with a range of 0 to 60 m s^{-1} and a precision of 0.3 m s^{-1} or 2% (whichever is greater) with a resolution of 0.1 m s^{-1}. Wind direction is measured with a range of 0° to 360° and a precision of ±2 % with a resolution of 1°. The precisions of the values of temperature and relative humidity are better than 0.3°C (at a temperature from –52°C to 60°C) and 3% (at a relative humidity in the range 0% to 90%), respectively. The barometric pressure is measured within a range of 600 to 1000 hPa and a precision of ±0.5 hPa (at a temperature from 0°C to 30°C).

The surface wind data obtained from ambient air pollution monitoring stations, MTSAT-1R data, upper sounding data at Tateno (36.05°N, 140.13°E), and weather charts published by the JMA were also used for the analysis.

4.3 Two-dimensional variational wind retrieval method

Since radial velocities observed by the Doppler lidar contain contributions from both the vertical and horizontal wind components for a slant-beam direction, it is necessary to use specific techniques and assumptions to retrieve the vertical air motion from the Doppler lidar data of RHI scans. Intrieri et al. (1990) and Darby et al. (2002) reported that the vertical velocities associated with a gust front can be calculated from the Doppler lidar data of RHI scans normal to the front using the equation of continuity. Since this technique uses a radial velocity divided by the cosine of the elevation angle as the horizontal wind component, only radial velocities at low-elevation angles can be used. Moreover, assumptions that (i) the density variation with height can be ignored and (ii) the flow is two-dimensional (Wakimoto 1982) must be valid. We show in the appendix Section 4.7 that the two assumptions were valid in this case.

We used a modified two-dimensional variational method, based on the three-dimensional variational method introduced by Gao et al. (1999), to retrieve two-dimensional wind fields. Retrievals are performed by finding the control variables $(\mathbf{v}, \mathbf{w})$ in a meridional cross section (i.e., y – z plane) that minimize the

so-called cost function, defined as:

$$J = J_O + J_B + J_D + J_S, \tag{4.1}$$

$$J_O = \frac{1}{2}\sum_m \lambda_O \Delta_m^2, \tag{4.2}$$

$$J_B = \frac{1}{2}\left[\sum_{j,k} \lambda_{vb}\left(\mathbf{v}-\mathbf{v}_b\right)^2 + \sum_{j,k} \lambda_{wb}\left(\mathbf{w}-\mathbf{w}_b\right)^2\right], \tag{4.3}$$

$$J_D = \frac{1}{2}\sum_{j,k} \lambda_D \mathbf{D}^2, \tag{4.4}$$

$$J_S = \frac{1}{2}\left[\sum_{j,k} \lambda_{vs}\left(\nabla^2\mathbf{v}\right)^2 + \sum_{j,k} \lambda_{ws}\left(\nabla^2\mathbf{w}\right)^2\right]. \tag{4.5}$$

The first term J_O in Eq. 4.1 is the difference between the retrieved and observed radial velocities, and m is the number of observations, the Δ_m is given by

$$\Delta_m = \overline{\mathbf{V}}_m \cdot \hat{\mathbf{r}}_m - \mathbf{V}_{rm}^{obs}. \tag{4.6}$$

Here, $\mathbf{v}_{rm}^{obs}$ is the observed radial velocity and $\hat{\mathbf{r}}_m = (y/r, z/r)$ is the unit vector from the Doppler lidar to the mth observation. The velocity field generated by the retrieved wind velocities $\mathbf{V}(\mathbf{r}) = (\mathbf{v}, \mathbf{w})$ is denoted by $\overline{\mathbf{V}}_m$, where the overbar implies interpolation to the coordinates of the mth observation. When interpolating $\mathbf{V}(\mathbf{r})$ to the coordinates of the mth observation, $\overline{\mathbf{V}}_m$ takes the following form:

$$\overline{\mathbf{V}}_m = \sum_{\mathbf{r}} C(\mathbf{r}-\mathbf{r}_m)\mathbf{V}(\mathbf{r}), \tag{4.7}$$

where $\mathbf{r}$ is a position vector to a grid point (j,k), and thus $\Sigma_\mathbf{r}$ implies summation over all grid points. The coefficient C in Eq. 4.7 is a Cressman weighting function depending on the distance between the grid point and observation point (Cressman 1959). The radius of influence in the Cressman interpolation step used in the calculation in Eq. 8 is 1.5 times as large as the grid spacing.

The second term J_B in Eq. 4.1 is the background term, and $(\mathbf{v}_b, \mathbf{w}_b)$ is the background velocity estimated from the VAD profile. The third term J_D in Eq. 4.1 imposes a weak anelastic mass constraint on the retrieved wind field,

$$D = \frac{\partial \overline{\rho} v}{\partial y} + \frac{\partial \overline{\rho} w}{\partial z}, \tag{4.8}$$

where $\overline{\rho}$ is the mean air density in the horizontal level. The last term J_S in Eq. 4.1 is the smoothing term.

Figure 4.2 shows a flow diagram describing the two-dimensional variational wind retrieval method. The cost function is minimized using a conjugate gradient method based on the Polak–Ribiere algorithm (Press et al. 1988). The wind retrieval method can be calculated in the following steps, with the calculating flow almost same as that described in Gao et al. (1999):

1) Choose the first guess of the control variables $\mathbf{Z} = (\mathbf{v}, \mathbf{w})^{\mathrm{T}}$; for this study, all first guesses are zero.

2) Calculate the cost function J according to Eqs. 4.1–4.5.

3) Calculate the gradients of the cost function $\partial J/\partial \mathbf{Z}$ with respect to the control variables.

4) Use a conjugate-gradient method based on the Polak–Ribiere algorithm to obtain updated values of the control variables,

$$\mathbf{Z}_{j,k}^{n} = \mathbf{Z}_{j,k}^{n-1} + \alpha f\left(\frac{\partial J}{\partial \mathbf{Z}}\right)_{j,k}, \tag{4.9}$$

where n is the number of iterations, α is an optimal step size, and $f(\partial J/\partial \mathbf{Z})_{j,k}$ is the optimal descent directions obtained by combining the gradients from the former iteration.

5) Check if the change in the cost function $\Delta J = J^n - J^{n-1}$ is less than a predefined tolerance, where we choose $\Delta J = 10^{-9}$. If the convergence criterion is not satisfied, repeat steps 2 and 3 using the updated control variables as the new guess. The iteration process is continued until meeting the predefined convergence criterion or reaching a maximum iteration number (100 here, because the horizontal and vertical wind remained essentially unchanged).

The parameter settings used are: $\lambda_O = 1/0.6^2$, $\lambda_{vb} = 0.1$, $\lambda_{wb} = 0$, $\lambda_D = 1/0.002^2$, $\lambda_{vs} = 5\times10^6$, and $\lambda_{ws} = 3\times10^5$, and chosen empirically in this study to ensure that the constraints are of roughly the same order of magnitude. The analysis domain and grid spacing were set up on a case-by-case basis. Times and elevation angles of the radial velocities of RHI scans, analysis domain and grid spacing in y and z used for the retrieval are listed in Table 4.1. The analysis domains were determined taking into account the relative spatial relationship between the Doppler lidar and SBF. When the SBF moved in the Doppler lidar observable domain (cases C and D), the correction method introduced by Gal-Chen (1982) was applied to cancel the SBF advection. The central time of the correction was set as the mid-time of the radial velocities used for the retrieval. From the SBF propagation speed (about 4.5 m s^{-1}; Section 4.4.2), the horizontal and vertical grid spacings were set to 400 m and 100 m, respectively. In cases A and B the correction for the SBF advection effects is not required and the horizontal and vertical grid spacings were set to 200 m and 100 m, respectively. The free-slip boundary conditions were imposed at the analysis domain top and bottom for v, whereas the Dirichlet boundary condition $w = 0$ is used for w. Open boundary conditions were used at the lateral boundaries.

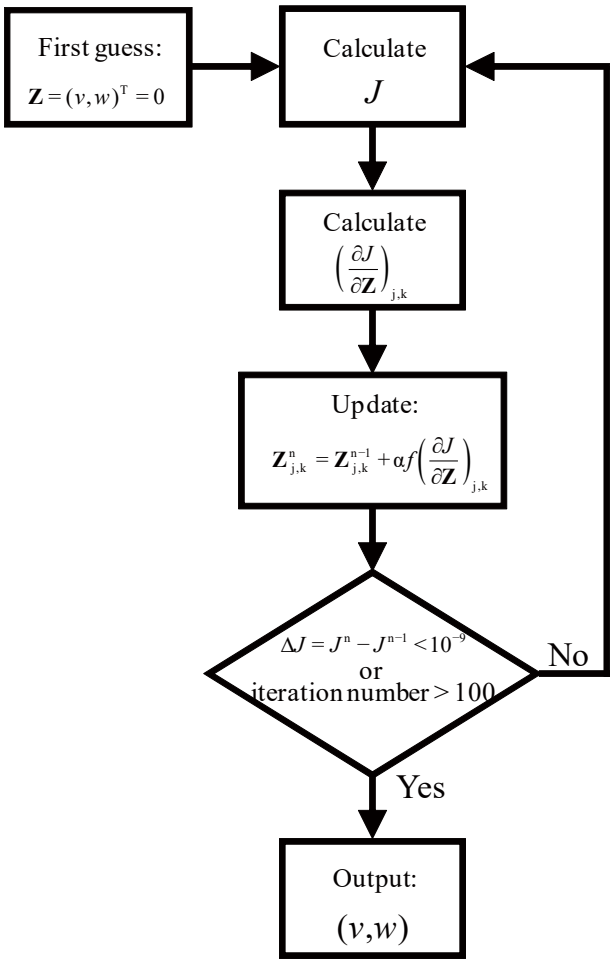

Figure 4.2. Flow diagram of the two-dimensional variational wind retrieval method.

Table 4.1. Times and elevation angles of the radial velocity of RHI scan, and analysis domain and grid spacing in y and z used for the two-dimensional variational wind retrieval method.

Case	Time	Elevation angle	Analysis domain / grid spacing	
			y	z
A	1524:59–1526:29 JST (90 seconds)	90°–180°	–4800 to 400 m / 200 m	0 to 3000 m / 100 m
B	1540:58–1542:28 JST (90 seconds)	90°–180°	–4800 to 400 m / 200 m	0 to 3000 m / 100 m
C	1553:38–1555:08 JST (90 seconds)	90°–180°	–4800 to 400 m / 400 m	0 to 3000 m / 100 m
D	1608:07–1609:37 JST (90 seconds)	0°–90°	–400 to 4000 m / 400 m	0 to 3000 m / 100 m

Before the start of the wind retrieval method, noise-contaminated wind data from the Doppler lidar were removed using a threshold level based on the SNR, with a predefined SNR threshold level (–17 dB) used to identify weak signals. The threshold level corresponded to the standard deviation of radial velocities being less than 1 m s^{-1} and was determined taking into account the result described in Ishii et al. (2005). Radial velocities below the threshold level were not used for the retrieval.

The mean error in the wind velocity was evaluated using the root-mean-square error (RMSE) between the retrieved radial velocities interpolated to the coordinates of the observation and observed radial velocities, which is defined as follows:

$$RMSE = \sqrt{\frac{\sum_{n=1}^{N}\left(V_{rn}^{obs} - \overline{\mathbf{V}}_n \cdot \hat{\mathbf{r}}_n\right)^2}{N}}. \tag{4.10}$$

Here, N is the total number of radial velocity measurements. In this study the RMSE was roughly 0.7 m s^{-1}, indicating that the retrieved wind is recovered with reasonable precision, because the parameter setting $\lambda_O = 1/0.6^2$ implies that the estimated mean error in the retrieved radial velocity is 0.6 m s^{-1}. The retrieved wind speed exhibits larger errors in regions of larger vertical wind shear (e.g., the boundary between the sea-breeze air and ambient air) or lower SNR.

4.4 Observed results

4.4.1 Meteorological situation

The surface synoptic chart at 0900 Japan Standard Time (JST) on 27 May 2008 (Fig 4.3; provided by the JMA) showed an eastward-drifting anticyclone over the Sea of Japan, a low-pressure system near the Kurile Islands, and a low-pressure system lying to the south of Japan. The synoptic situation resulted in both a north-south and east-west pressure gradient. At 0900 JST, the geostrophic wind was from 63.4° at 5.5 m s^{-1}.

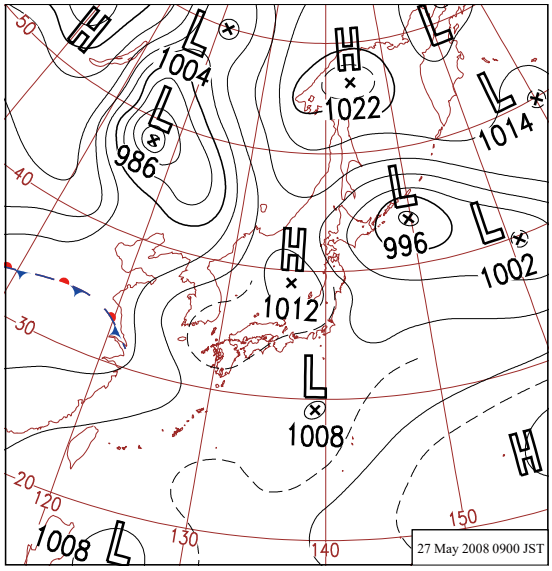

Figure 4.3. Synoptic situation: JMA surface weather chart for 0900 JST on 27 May 2008.

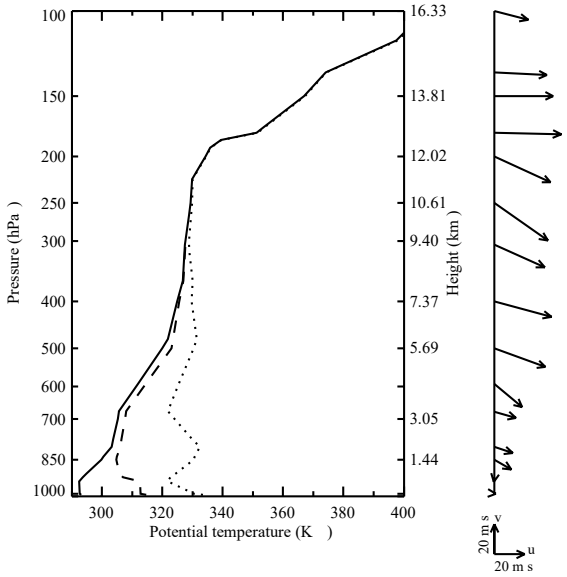

Figure 4.4. Vertical profiles of potential temperature (solid lines), equivalent potential temperature (dashed lines), saturated equivalent potential temperature (dotted lines), and horizontal wind vector (arrows) at 0900 JST on 27 May 2008 at Tateno.

Upper sounding data observed at Tateno at 0900 JST on 27 May 2008 (Fig. 4.4) showed that the atmosphere below 500 hPa was in a state of stable. Because the convective available potential energy (CAPE) was 0 J kg^{-1} and the low-level atmosphere was dry, the atmospheric condition did not favor the development of convection.

Figure 4.5 shows a Multifunctional Transport Satellite-1R (MTSAT-1R) satellite image in the visible channel at 1600 JST on 27 May 2008 when the SBF passed at the observation site (see Section 4.4.2). The satellite image showed no cloud cover over the Tokyo metropolitan area, while images at 1500 and 1700 JST (not shown) also showed no cloud cover over the Tokyo metropolitan area.

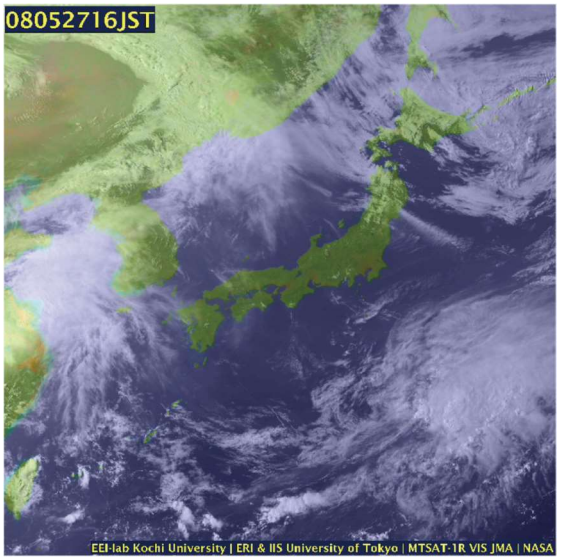

Figure 4.5. MTSAT-1R satellite image in visible channel at 1600 JST on 27 May 2008; provided by Kochi University (information online at http://weather.is.kochi-u.ac.jp/) and JMA.

Figures 4.6a–d show the two-hourly surface wind fields around the Tokyo metropolitan area during the daytime on 27 May 2008, obtained from ambient air pollution monitoring stations. The northerly winds cover the Tokyo metropolitan area at 1000 JST (Fig. 4.6a). The wind fields at 1200 JST (Fig. 4.6b) and 1400 JST (Fig. 4.6c) show the

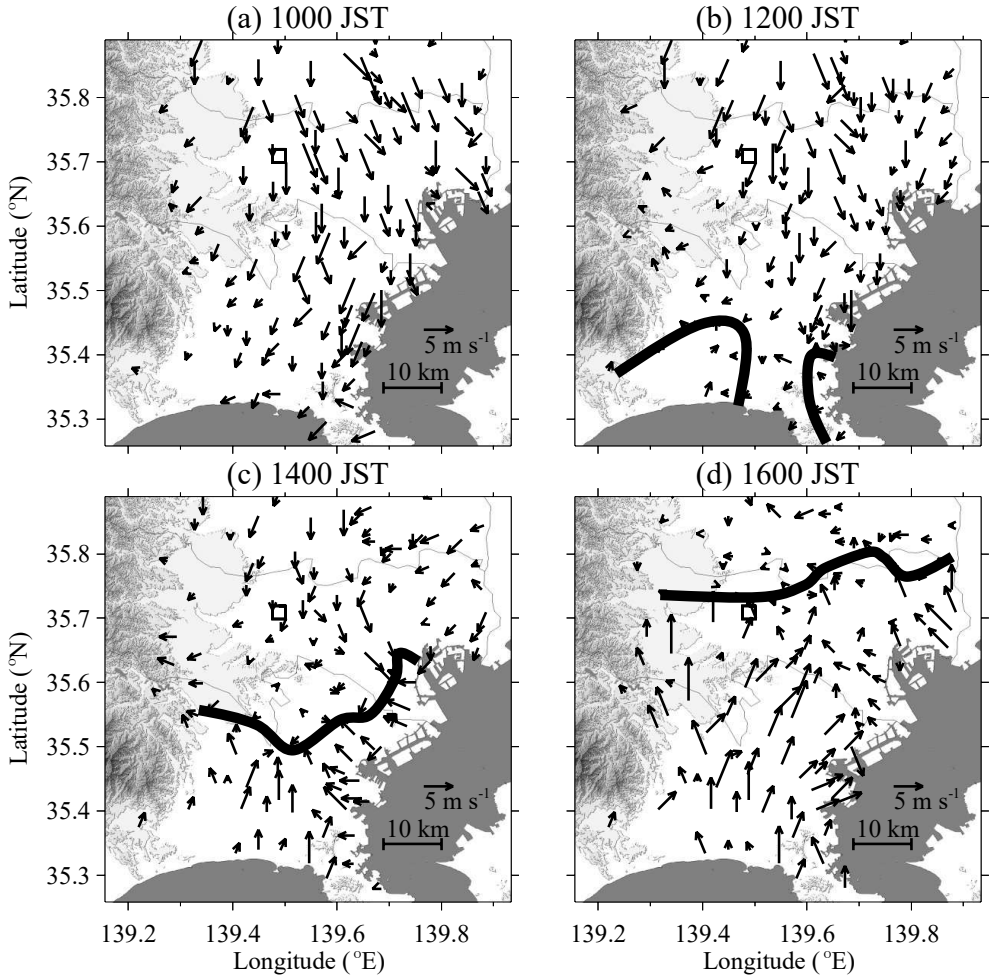

Figure 4.6. Surface wind fields (arrows) observed by ambient air pollution monitoring stations at (b) 1000, (b) 1200, (c) 1400, and (d) 1600 JST on 27 May 2008. The open square indicates the location of the NICT headquarters. The solid line at each panel indicates the location of the SBF.

onset of sea breezes at Sagami Bay and Tokyo Bay, respectively, which converge over the Tokyo area (Kai et al. 1995; Kanda et al. 2001). The arrival of the sea breeze from Sagami Bay at the observation site can be recognized in the wind field at 1600 JST (Fig. 4.6d).

Vertical profiles of horizontal winds observed by the Doppler lidar on 27 May 2008 (Fig. 4.7) show the temporal evolution of the wind field, as depicted in Fig. 4.6. The profiles were taken from 20°-elevation and 70°-elevation VAD data of the Doppler lidar. A strong northerly to easterly flow is evident up to 3000 m AGL until 1300 JST, after which the horizontal wind speed below 2000 m gradually decreased. At 1500 JST, just before the arrival of the sea breeze at the Doppler lidar site, the horizontal wind speed below 2000 m was 1–3 m s^{-1}. The vertical profiles of the horizontal winds show the sea-breeze layer with about 800-m depth starting at 1600 JST and growing slowly for the next three hours to about 1200-m depth.

The mixing heights estimated from the 70°-elevation VAD scans taken by the Doppler lidar are also represented by open triangles in Fig. 4.7. Here, according to Seibert et al. (2000) the mixing height is defined as “the height of the layer adjacent to the ground over which pollutants or any constituents emitted

within this layer or entrained into it become vertically dispersed by convection or mechanical turbulence within a time scale of about an hour." The mixing height was determined by locating the height of the maximum negative gradient in the SNR profiles, corresponding to the height where the aerosol concentration decreases most rapidly. Newsom et al. (2008) showed that there was reasonably good agreement between the mixing heights derived from the Doppler lidar data using this technique and the heights of the capping inversion observed by radiosondes. Before 0800 JST and after 1400 JST, the mixing heights were not estimated because of the absence of the distinct maximum negative gradient in the SNR profiles. According to Fig. 4.7, the mixing height at 0800 JST is about 1000 m, increasing rapidly after 0900 JST and reaching a maximum height of about 1900 m at 1300 JST to 1400 JST.

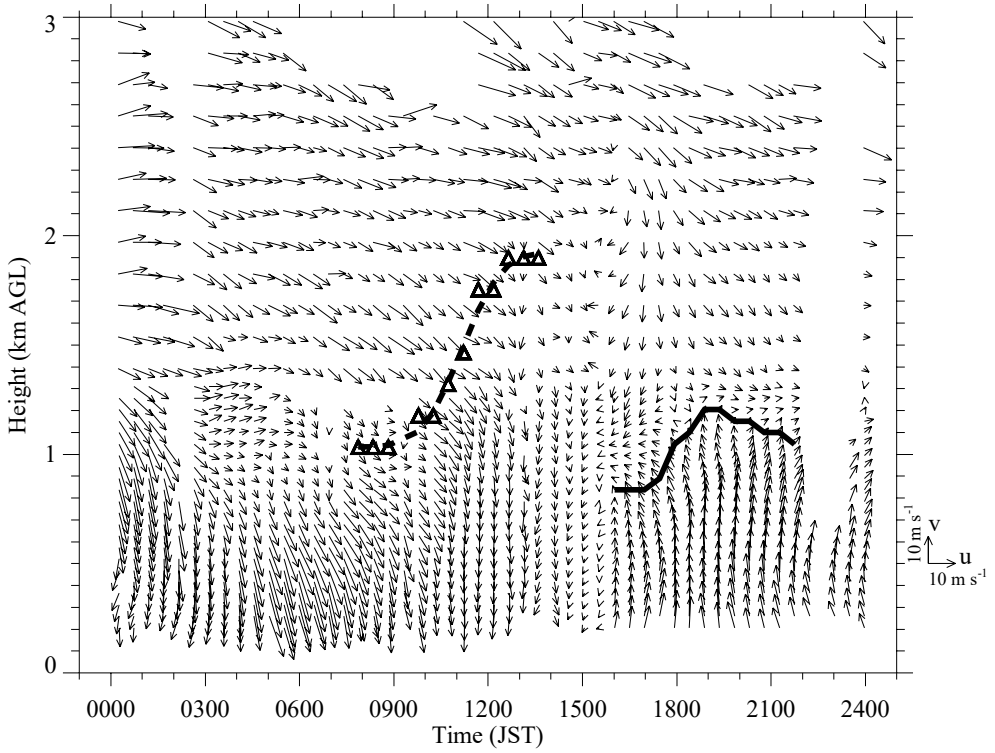

Figure 4.7. Time-height cross section of horizontal winds on 27 May 2008 taken from the 20°-elevation and 70°-elevation VAD data of the Doppler lidar. The horizontal winds below and above 1300 m were retrieved from the 20°-elevation and 70°-elevation VAD data, respectively. Open triangles display the mixing heights estimated from 70°-elevation VAD scans taken by the Doppler lidar. The solid line indicates the height of the sea-breeze layer.

4.4.2 Sea-breeze frontal structure

Figure 4.8 shows the time series of ceilometer optical backscatter coefficient and collocated surface meteorological data. We find a different tendency in the surface data after roughly 1600 JST, compared with data before 1600 JST, while relative humidity shows the most sudden change at 1556 JST, from 20% to 40%, together with temperature, for which the decrease trend starts at 1556 JST. At the same time, the surface wind speed increased from 1.0 m s^{-1} to 2.5 m s^{-1}, and wind direction changed gradually from

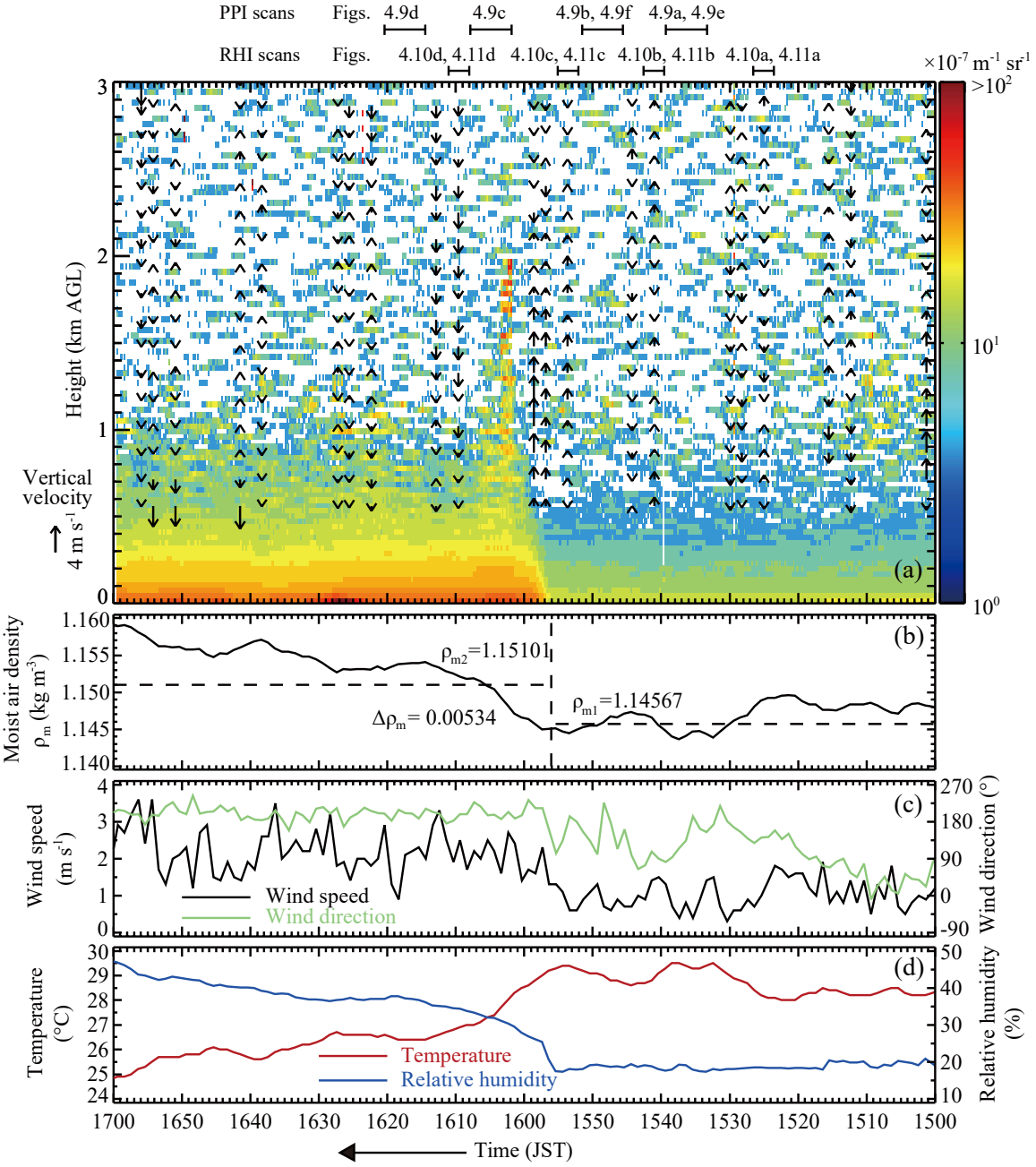

Figure 4.8. (a) Time-height cross section of ceilometer optical backscatter coefficient between 1500 and 1700 JST on 27 May 2008. The vertical wind velocities observed by the Doppler lidar are superimposed as arrows on the ceilometer data. (b–d) Time series of (b) moist air density (kg m^{-3}), (c) wind speed (m s^{-1}) and wind direction (°), and (d) temperature (°C) and relative humidity (%). The dashed horizontal lines in Fig. 4.8b represent the 30-min averages before and after the changes in temperature and relative humidity. Temporal coverage of the Doppler lidar PPI scans and RHI scans is shown at the top of the figure.

north-east to south. In-situ temperature, relative humidity, and pressure data were used to calculate the moist air density (Fig. 4.8b), which was calculated according to equations described in Appendix A of Mayor (2011). The dashed horizontal lines in Fig. 4.8b represent the 30-min averages before and after the

changes in temperature and relative humidity. The 30-min average moist air density increased from 1.146 to 1.151 kg m^{-3} (Fig. 4.8b). Those changes around 1556 JST suggest the passage of a sea-breeze gravity current with a distinctive front structure, and at about 1557 JST, the optical backscatter coefficient showed a sudden increase mainly below 1 km AGL. The Doppler lidar observed a weak updraft at 1553:38 JST and a strong updraft (maximum w equal to 4.2 m s^{-1}) at 1558:34 JST, up to about 2 km. After the strong updraft, intense optical backscatter, up to 2 km AGL, was observed by the ceilometer from 1602:01 to 1603:46 JST. The interpretation of the backscatter coefficient enhancement observed by the ceilometer is mentioned in Section 4.5.2. The relationship between the updraft and the intense optical backscatter is discussed in Section 4.5.3.

Figure 4.9 shows the horizontal variability of the radial velocity of the sea-breeze flow near the surface observed by the Doppler lidar with the 1°-elevation PPI scan. Before the sea-breeze frontal passage at the lidar site (panel center; Fig. 4.9a), the pattern of the observed radial wind velocities showed disorganized currents of air in the lower atmosphere with a horizontal scale of a few km. This pattern can reasonably be interpreted as the presence of thermals (Stull 1988). Figure 4.9e shows the locations where radial convergences (R_C) exceed 8×10^{-3} s^{-1} for the same time as in Fig. 4.9a. Here, R_C was calculated as

$$Rc = -\left(\frac{\partial V_r}{\partial r} + \frac{V_r}{r} \right), \tag{4.11}$$

where V_r is the radial velocity and r is the range. There is a convergence area at about 1 km south of the lidar site, and it is expected that the thermal existed at the convergence area. At 1545 JST (Fig. 4.9b), a southerly flow dominated in the south to south-west region of the plot, while the disorganized currents of air dominated in the northern part. The SBF propagating northward may have reached about 1.5 km south of the lidar site. Figure 4.9f shows the locations where radial convergences exceed 8×10^{-3} s^{-1} at the same time as in Fig. 4.9b. There are convergence areas at about 1 km south of the lidar site and along the SBF, and it is suggested that the prefrontal thermal existed about 500 m ahead of the SBF at that time. The sea breeze was southerly with a wind speed of about 8 m s^{-1} and the SBF propagation speed was about 4.5 m s^{-1} as estimated from the change in the position of the SBF between Figs. 4.9b and 4.9c. After the sea-breeze frontal passage at the lidar site (Figs. 4.9c and 4.9d), the sea breeze (i.e., southerly wind) prevailed over the observed region. A near-surface streaky structure with a cross-stream horizontal scale of about 1 km was observed in the sea breeze. This structure may be caused by the presence of horizontal convective rolls (e.g., Brown 1980; Etling and Brown 1993) and is very similar to that presented in Chapter 3. But the cross-stream horizontal scale in this case is larger. It is thought that one of the reasons for the difference of the cross-stream horizontal scale is the height of the sea-breeze layer. The characteristic scale of the streaky structure is also affected by atmospheric stability (Newsom et al. 2008) and surface roughness (Lin et al. 1997).

Figure 4.10 displays four panels of north-south vertical cross sections of Doppler lidar radial velocity showing the evolution of the vertical structure of the sea breeze. The cross section baseline is mostly perpendicular to the front line of the observed sea breeze. The wind vectors representing the vertical and meridional wind velocities retrieved by the two-dimensional variational method are superimposed on the

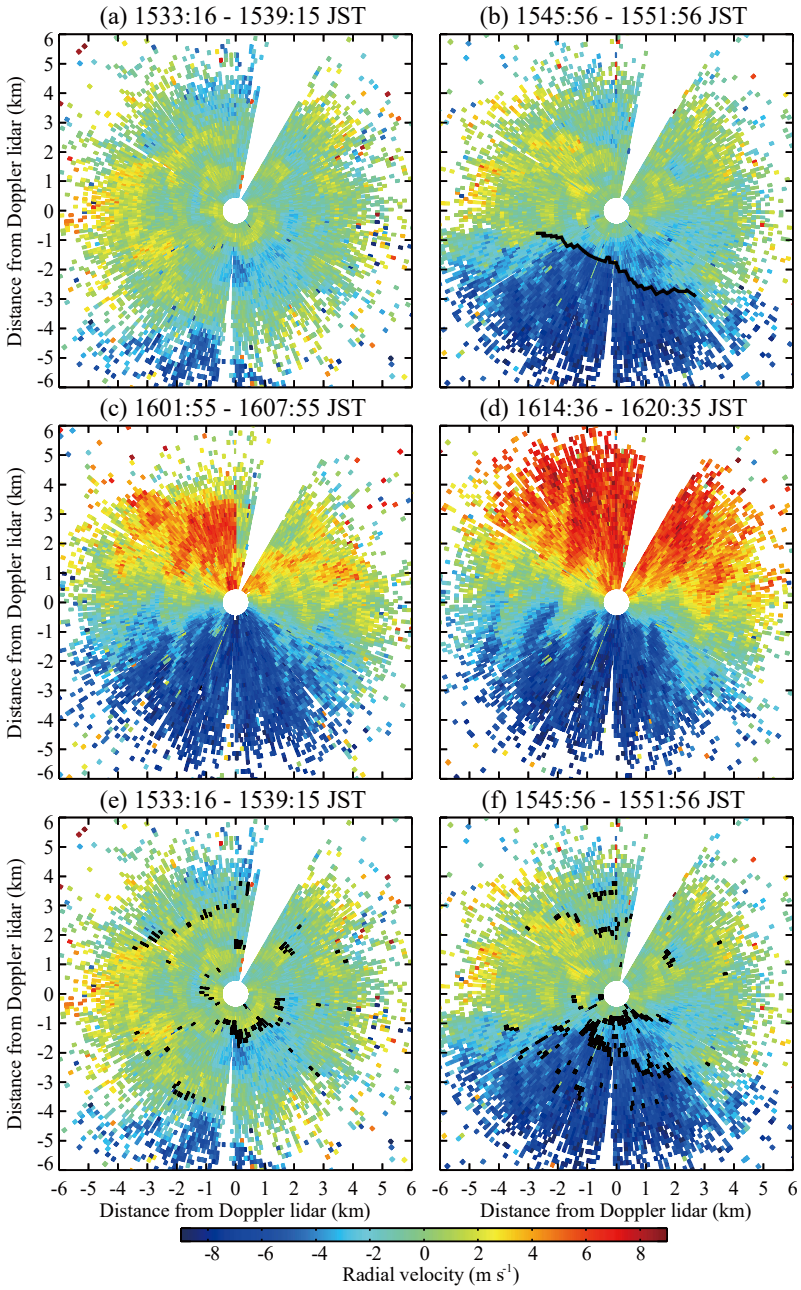

Figure 4.9. Doppler lidar 1°-elevation PPI scans of radial velocity (color bar in m s^{-1}) at (a) 1533, (b) 1545, (c) 1601, (d) 1614, (e) 1533, and (f) 1614 JST on 27 May 2008. Negative velocities, represented in blue, indicate flow toward the Doppler lidar. Positive velocities, represented in red and yellow, indicate flow away from the Doppler lidar. The thick black line in Fig. 4.9b indicates the location of the SBF as determined by the location of the maximum positive gradient along the radial direction in the range-corrected SNR data, corresponding to the location where the aerosol concentration increases most rapidly. The black overplotted radial velocity in Figs. 4.9e and 4.9f indicates the locations where the radial convergences exceed 8×10^{-3} s^{-1}.

radial velocity. Before the sea-breeze frontal passage at the Doppler lidar site (Figs. 4.10a and 4.10b), a thermal with a horizontal scale of about 500 m existed about 1 km south of the Doppler lidar site. Its location corresponds to the location of the convergence area displayed in Figs. 4.10e and 4.10f. Since

thermals generally have three-dimensional structures (Stull 1988), the wind velocity derived from the two-dimensional variational method probably includes uncertainty. Therefore the wind velocity in Fig. 4.10 may be used to depict general features of *w* for the observed thermal. In Fig. 4.10b, the SBF reached about 4 km south of the lidar site and an updraft (maximum *w* approximately equal to 2 m s^{-1}) was observed over the nose of the SBF. The SBF propagation speed was about 4.7 m s^{-1} as estimated from the change in position of the SBF between Figs. 4.10c and 4.10d. This value is close to the estimate of 4.5 m s^{-1} derived from the Doppler lidar data of PPI scans. The vertically averaged horizontal wind speed in the trailing body of the sea breeze was about 8 m s^{-1}, thus the sea-breeze flow behind the SBF was moving toward the SBF faster than the SBF itself. At the arrival of the SBF at the Doppler lidar site (Fig. 4.10c), a strong updraft (maximum *w* approximately equal to 5 m s^{-1}) with a horizontal scale of about 500 m and vertical scale of 2 km was observed over the nose of the SBF. This updraft intensified during the time between Fig. 4.10b and Fig. 4.10c. The spatial relationship between the thermal and the strong updraft over the nose of the SBF suggests that there was a contribution from the interaction between the SBF and the thermal to the intensification of the updraft. Using a high-resolution numerical model, Ogawa et al. (2003) showed that SBFs sometimes interact with prefrontal convective cells and intensified frontal updrafts are formed. After the sea-breeze frontal passage at the Doppler lidar site (Fig. 4.10d), the height of the sea-breeze head increased from about 800 m to 1000 m. A closed vortex roll with a diameter of about 500–1000 m can be found around the top of the sea-breeze head.

Figure 4.11 displays four panels of north-south vertical cross sections of Doppler lidar range-corrected SNR. In Figs. 4.11a and 4.11b, there was no relatively higher range-corrected SNR zone related to the prefrontal thermal. In Figs. 4.11c and 4.11d, there was a relatively higher SNR region around and below the estimated location of the maximum gradient of the radial velocity in the azimuthal direction. Especially noteworthy is that there was little signature of the relatively higher range-corrected SNR related to the strong updraft over the nose of the SBF (Fig. 4.11c). The interpretation of the range-corrected SNR enhancement observed by Doppler lidar is mentioned in Section 4.5.2 below.

4.5 Discussion

4.5.1 Propagation speed of SBF

The propagation speed of the SBF was found to be about 4.5 m s^{-1} as estimated from the change in position of the SBF between Figs. 4.9b and 4.9c (Section 4.4.2). Simpson and Britter (1980) determined that the propagation speed of an SBF (V_{front}) is slowed by about three-fifths the speed of the opposing flow (V_{wind}; positive when the ambient flow opposes the sea breeze), using

$$V_{front} = k\sqrt{\frac{\rho_{m2} - \rho_{m1}}{\rho_{m1}} gd} - 0.62V_{wind}, \tag{4.12}$$

where *k* is the Froude number, ρ_{m1} is the mean moist air density of the ambient warm and lighter air, ρ_{m2} is the mean moist air density of the cool and heavier advancing air (i.e., marine air mass), *d* is mean depth of

the marine air mass, and g is the gravitational acceleration. Here, it is assumed k = 0.72, as reported by

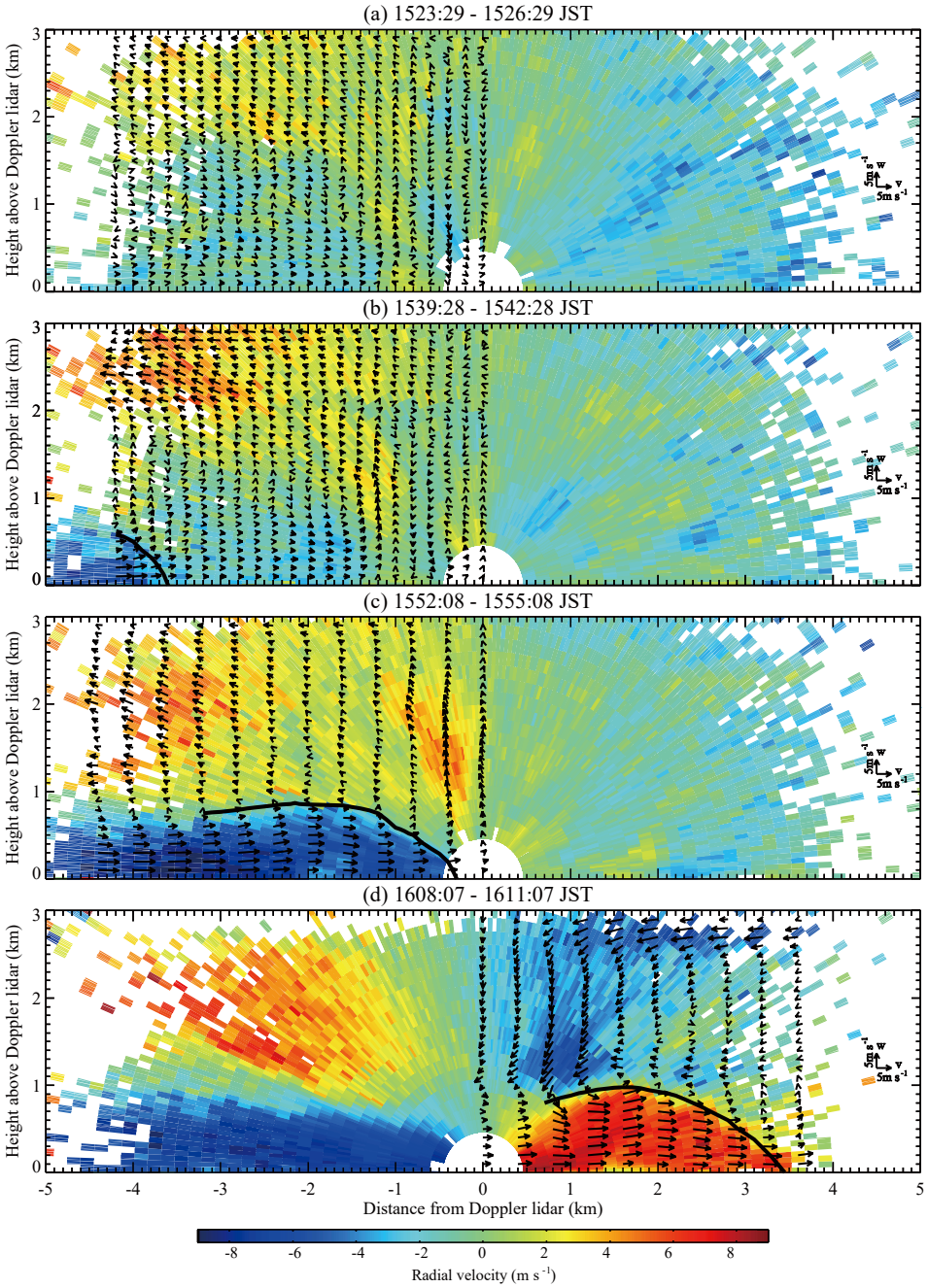

Figure 4.10. North-south vertical cross sections of Doppler lidar radial velocity (color bar in m s^{-1}) with positive values indicating flow away from the Doppler lidar. The horizontal axis is the distance in km from the Doppler lidar with positive values pointing toward 0° azimuth (northward), and the vertical axis is the height above the Doppler lidar in km. Times of RHI scans were as follows: (a) 1523, (b) 1539, (c) 1552, and (d) 1608 JST on 27 May 2008. The vertical and meridional wind velocities retrieved by the two-dimensional variational method are superimposed on the color map as indicated by black arrows. The thick black lines in Figs. 4.10b, 4.10c, and 4.10d denote the boundary separating air masses. The boundary was estimated by location of the maximum gradient of the radial velocity in the azimuthal direction.

Simpson (1969) for SBF observations. The values ρ_{m1} and ρ_{m2} were 1.146 kg m^{-3} and 1.151 kg m^{-3}, respectively (derived from 30-min average moist air density before and after the changes in temperature and relative humidity; Fig. 4.8b). The mean depth of the marine air mass was estimated to be about 700 m from the location of the maximum gradient of the radial velocity in the azimuthal direction at about 5–6 km to the rear of the leading edge (Fig. 4.10d). The speed of the opposing flow was estimated to be about 0.59 m s^{-1} derived from the Doppler lidar data of the VAD scan below 700 m AGL at about 1530 JST (see Fig. 4.7). Thus the theoretical value of the propagation speed of SBF is 3.70 m s^{-1}, and smaller than the observed value of 4.5 m s^{-1} but largely matches the observed value. This discrepancy may be due to the difficulty in accurately determining the mean moist air density and mean depth of the sea-breeze layer.

It is well known that the SBF is typical example of a density (or gravity) current (Simpson 1994) and the dynamical similarity between the SBFs and density currents was examined through comparison of the Froude number. For comparison with other previous studies, the value of k was calculated using the observed values of ρ_{m1}, ρ_{m2}, d, and V_{wind} and observed value of the propagation speed of SBF (4.5 m s^{-1}). The calculated k value was 0.86. The value of k is close to the previously reported k of 0.5–1.0 with an average of 0.7 for SBFs in opposing flow cases (Atkins and Wakimoto 1997), and 0.70–1.08 for atmospheric density currents such as gust fronts (e.g., Wakimoto 1982). It is suggested that density current theory may be applicable to the sea breeze observed in this study.

4.5.2 Interpretation of ceilometer backscatter and Doppler lidar range-corrected SNR enhancement

Before and after the sea-breeze frontal passage, significant enhancement of the backscatter coefficient and range-corrected SNR was observed by the ceilometer and Doppler lidar, respectively (see Fig. 4.8a and Fig. 4.11). In order to explain the enhancement we need to consider the contribution of relative humidity to the lidar reflectivity, which is the product of a backscatter coefficient and the square of atmospheric transmission, and whose fluctuations correspond to the fluctuations of range-corrected SNR (Section 2.1). The lidar reflectivity is influenced by increasing the size of hygroscopic aerosol particles under high relative humidity conditions.

Since we have only the relative humidity measured near the ground (at 18 m AGL), we estimated the variations in relative humidity with height in SBFs from previous field measurements. Previous aircraft-based observations of SBFs (Kraus et al. 1990; Finkele et al. 1995; Stephan et al. 1999; Wood et al. 1999) provided specific humidity and potential temperature at different heights. The variations in relative humidity with height estimated from these data are about 10%. Since the relative humidity at 18 m AGL in the SBF was about 40% in this study (see Fig. 4.8d), the maximum value of relative humidity in the SBF may be up to 50%. Earlier Fitzgerald (1989) showed that when relative humidity rises above 50%, particle sizes and optical properties are substantially affected. Gibert et al. (2007) showed that the relative humidity variation of 10% in the range between 45% and 70% accounts for 10% to 20%, and nearly 5% of the lidar reflectivity variation at 2 and 0.5 μm wavelength. The two-way atmospheric transmission (i.e., square of atmospheric transmission) near ground level is –1.3 dB km^{-1} in a mid-latitude summer clear atmosphere

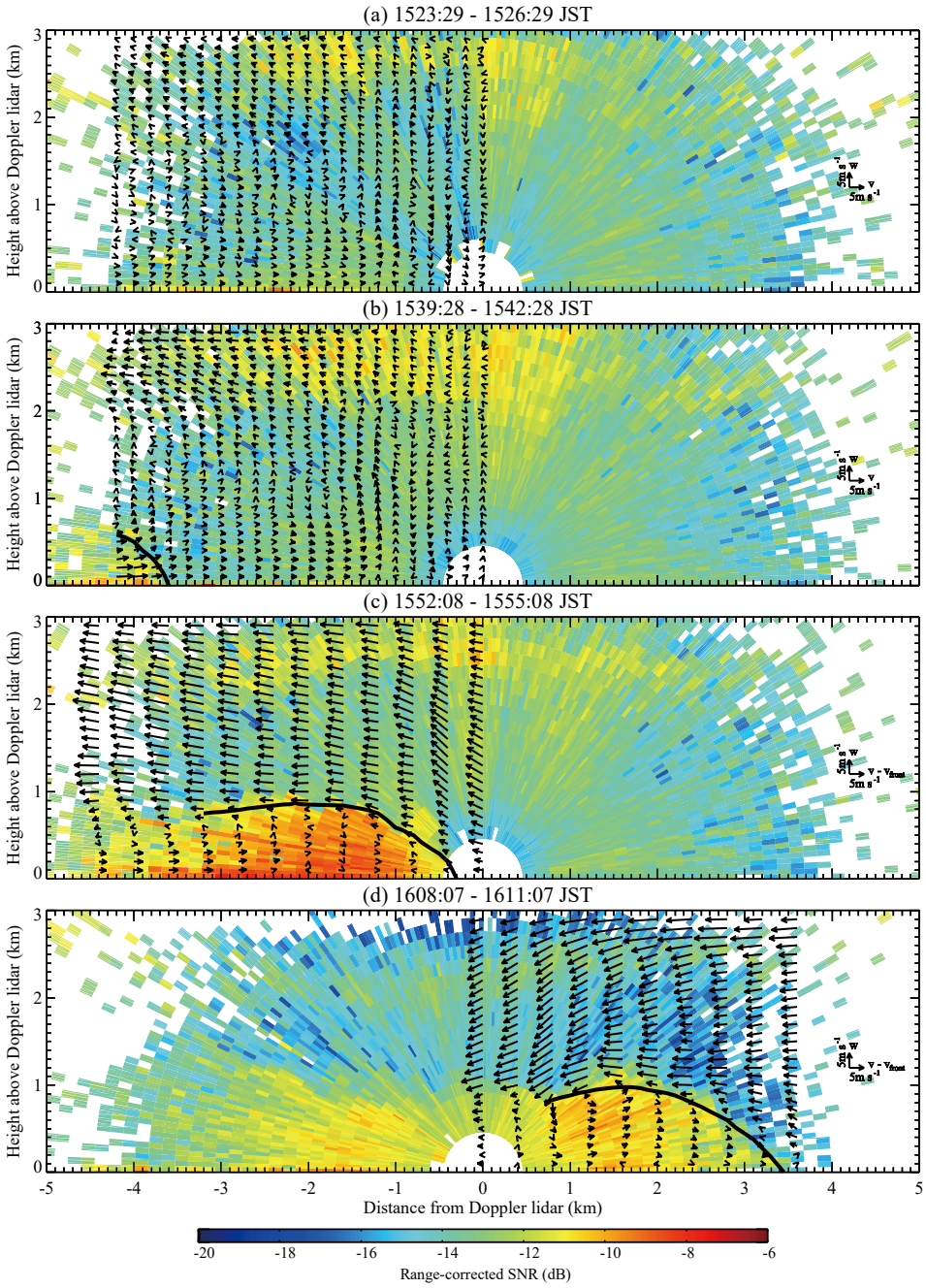

Figure 4.11. North-south vertical cross sections of Doppler lidar range-corrected SNR (color bar in dB). The horizontal axis is the distance in km from the Doppler lidar with positive values pointing toward 0° azimuth (northward), and the vertical axis is the height above the Doppler lidar in km. Times of RHI scans were as follows: (a) 1523, (b) 1539, (c) 1552, and (d) 1608 JST on 27 May 2008. In Figs. 4.11a and 4.11b, the vertical and meridional wind velocities retrieved by the two-dimensional variational method are superimposed on the color map, indicated by black arrows. In Figs. 4.11c and 4.11d, the vertical and SBF relative meridional wind velocities retrieved by the two-dimensional variational method are superimposed on the color map, indicated by black arrows. The thick black lines in Figs. 4.11b, 4.11c, and 4.11d denote the boundary separating air masses. The boundary was estimated by location of the maximum gradient of the radial velocity in the azimuthal direction.

and –3.1 dB km^{-1} in a mid-latitude summer hazy atmosphere at 2.0125 μm Tm:YAG wavelength

(Henderson et al. 1993). Since the atmospheric transmission at these wavelengths decreases slightly with relative humidity in the range between 45% and 70%, an increase in lidar reflectivity with relative humidity results from an increase in backscatter coefficient. The ceilometer backscatter coefficient and Doppler lidar range-corrected SNR in the SBF was at least 4 dB higher than in the ambient air (see Fig. 4.8a and Fig. 4.11c). For the above reasons, the contribution of relative humidity variation to the enhancement of the ceilometer backscatter coefficient and Doppler lidar range-corrected SNR was small. This implies that the enhancement mainly resulted in the aerosol concentration enhancement and the air mass containing relatively denser aerosol was behind the SBF. A circulation behind the SBF may have been responsible for maintaining a high aerosol concentration zone (e.g. Ueda et al. 1988).

Because we do not have the relative humidity profile, it is difficult to estimate the influence of the relative humidity on the intense optical backscatter up to 2 km AGL observed by the ceilometer quantitatively. Our discussion here is on whether the intense optical backscatter is a signature of clouds. There is one possibility that the increased backscatter for the ceilometer is due to a cloud passing overhead, reducing the amount of background light and thus making it possible to observe more aerosol return aloft. Another possibility is that fair-weather cumulus clouds were formed over the SBF and “curtains” of cloud were formed along the slope of the SBF (Simpson 1994; Wallington 1959). The satellite image (Fig. 4.5) showed no cloud cover over the Tokyo metropolitan area at almost the same time as the sea-breeze frontal passage at the observation site. The Doppler lidar range-corrected SNR of RHI scans (Fig. 4.11) and 70°-elevation VAD scans (not shown) before and after the time of the sea-breeze frontal passage showed no signature of clouds from 1000 to 2000 m AGL. For the above reasons, the intense optical backscatter up to 2 km AGL observed by the ceilometer is probably a signature of aerosols. The horizontal advection of the aerosols from a farther range cannot explain the observation results at the short time scale of 105 sec (from 1602:01 to 1603:46 JST). It is probably an appropriate interpretation that the aerosols were vertically transported from the lower level. If so, why did the Doppler lidar not observe some portion of the enhanced aerosol backscatter that the ceilometer observed (Fig. 4.11c)? One simple interpretation is a difference in wavelength (2 and 0.9 μm), that is only the smaller aerosols provided the backscatter. Because the influence of gravity on the aerosols with diameters less than 1 μm, which can be detectable by both the Doppler lidar and ceilometer, is negligible, it cannot be assumed that only the smaller aerosols were transported selectively. It is considered that the vertical transport of aerosols occurred after the time of the RHI scan, from 1552 to 1555 JST (Fig. 4.11c). In the next section we discuss the relationship between the updraft and the intense optical backscatter.

4.5.3 Relationship between updraft and intense ceilometer optical backscatter

Figure 1.1 illustrates a model of a sea-breeze gravity current front. There are two scenarios of prominent updrafts associated with the front; the primary updraft is in the ambient warm air immediately ahead of the front, with another updraft is in the sea-breeze cold air behind. In Fig. 4.8a, there is no intense optical backscatter associated with a weak updraft at 1553:38 JST and a strong updraft at 1558:34 JST up to about 2 km AGL observed by the Doppler lidar. In Fig. 4.11c, the range-corrected SNR in the region of

the strong updraft formed over the nose of the SBF is considerably weaker than that in the sea-breeze layer. These observations indicate that the strong updraft is the primary updraft in the ambient warmer and clearer air.

One question of interest here is: what is the intense optical backscatter up to 2 km height observed by the ceilometer from 1602:01 to 1603:46 JST after the commencement of the strong updraft over the nose of the SBF (Fig. 4.8a)? We speculate three scenarios for interpretation. The intense optical backscatter is a signature of:

1) A raised sea-breeze head due to the rapid temporal development of the SBF;
2) Translocation, in which a plume system encountering an updraft immediately ahead of the SBF is vertically advected to large elevations;
3) Escape and vertical transport of the near-surface denser aerosols trapped in the head region of the SBF.

The first interpretation is similar to the process described by Bastin and Drobinski (2006). Using numerical simulations of the free troposphere in southern France on 25 June 2001, they showed that convergence at an SBF forms a raised sea-breeze head extending up to 1.2 km AGL, with strong updrafts. From 1552:08 to 1555:08 JST the height of the SBF was about 700 m (Figs. 4.10c and 4.11c), and from 1608:07 to 1611:07 JST about 900 m (Figs. 4.10d and 4.11d). If this interpretation is correct, the sea-breeze head began to deepen rapidly after about 1555 JST, reached a height of about 2 km at 1602 JST and declined from about 1608 JST. This implies that frontogenesis (FG) and frontolysis (FL) phenomena occurred for only 6–7 min. Using high-resolution numerical modelling, Ogawa et al. (2003) showed that the temporal scale of FG and FL phenomena due to the interaction of an SBF with prefrontal convective cells is several tens of minutes. Therefore, explanation that the intense optical backscatter observed by the ceilometer is a signature of a raised sea-breeze head could be difficult. However, the increase of the height of the SBF from about 700 m to 900 m (i.e., the FG phenomenon) can be explained by the interaction between the SBF and the prefrontal thermal, and this is consistent with the result of Ogawa et al. (2003).

The first interpretation is also checked evaluating the nose slope of the observed SBF. Given that the frontal surface of the SBF moved from south to north at the observation site with constant SBF propagation speed (about 4.5 m s^{-1}, see Section 4.4.2), the slope of the SBF nose can be calculated from the ceilometer data. The timing between the first ceilometer measurement of the SBF at ground level (1557:16 JST) and the time of the backscatter enhancement at 400 m AGL (1559:16 JST) is 120 sec. The time scale of 120 sec translates into a 540-m horizontal scale using a 4.5 m s^{-1} SBF propagation speed. Therefore, the slope of the SBF below 400 m AGL is around 36.5° ≈ arctan(400/540) to the horizontal. The timing between the first ceilometer measurement of the SBF and the time of the high backscatter at 2 km (1602:01 JST) is 285 sec. Given that the high backscatter is a signature of a raised sea-breeze head, there is a 1280 m horizontal distance between these two times. Thus the slope of the SBF at 2 km AGL is around 57.3° ≈ arctan(2000/1280) to the horizontal, implying that the SBF has much a steeper slope aloft. Theoretical studies (e.g., Xu 1992), laboratory tank experiments (e.g., Simpson 1994), and field measurements (e.g., Nakane and Sasano 1986; Mayor 2011) indicate that the frontal slopes are steep near

the surface and decrease at higher points on the frontal surface. Thus, from the viewpoint of the head slope, the first interpretation is inconsistent with the results of the previous studies.

The second interpretation is similar to the process described by Lyons et al. (1995) and Thompson et al. (2007). Using numerical simulations, Lyons et al. (1995) showed that a tracer plume as a whole was vertically translocated to as high as 1600 m by the updrafts associated with the lake-breeze front at Lake Michigan. Thompson et al. (2007) showed that a SBF travelling over New York City has a significant impact on transport and diffusion of simulated tracer plumes, and, in particular, the strong updraft at the head of the sea breeze advects tracer material to higher levels. In our study, no prefrontal plume containing denser aerosol was observed by the Doppler lidar or ceilometer. Moreover, if the prefrontal plume is translocated by the strong updraft over the nose of the SBF, there should be higher range-corrected SNR in the region of the strong updraft was observed by the Doppler lidar as in Fig. 4.11c, or the intense optical backscatter at the same time the strong updraft was observed by the ceilometer as in Fig. 4.8a.

For the third interpretation, if aerosols escaped from the nose of the SBF (about 300 m AGL) at 1555 JST and the strong updraft over the nose transported the aerosols up to the mixing height (about 2000 m height) to 1602 JST, an updraft of approximately 4 m s^{-1} might transport aerosols. The rising speed of the aerosols is reasonably consistent with the strong updraft formed over the nose of the SBF (maximum w approximately equal to 5 m s^{-1}, see Section 4.4.2). The time scale of 105 sec (from 1602:01 to 1603:46 JST) of the intense optical backscatter up to 2 km observed by the ceilometer corresponds to the spatial scale of 472.5 m due to the SBF propagation speed of about 4.5 m s^{-1}. The spatial scale is reasonably consistent with the horizontal scale of the strong updraft formed over the nose (about 500 m, see Section 4.4.2).

The last interpretation implies that the vertical transport of the near-surface denser aerosols trapped in the head region of the SBF occurred not continuously but intermittently. If the vertical transport occurred continuously, the Doppler lidar would detect the signature of denser aerosol particles in the range-corrected SNR data. We surveyed dozens of cases in which the ceilometer observed the sudden increase in the optical backscatter coefficient at a low level associated with the sea-breeze frontal passage, from August 2003 to August 2008. The survey consequently found no case similar to this study. This means that the vertical transport does not always occur. Although it is suggested that the escape of aerosols from the SBF head was triggered by interaction between the SBF and the prefrontal thermal, the Doppler lidar contained no observational result to identify the mechanism of SBF-thermal interaction and aerosol escape. Lyons and Olsson (1973) showed “suspected trajectories” of gases and various size aerosols at the lake-breeze front from pilot balloon, tetroon, and aircraft measurements. They suggested that these gases and aerosols ascend at the rear of the head of the front, mostly at about 1–2 km from the leading edge. The process is similar to that suggested by this study. Yet it has not been revealed how the ambient air and the uplifted gases and aerosols mix.

4.6 Summary

We used data acquired by a Doppler lidar, ceilometer, and meteorological surface station on 27 May 2008 to document the vertical and horizontal structure of a well-developed SBF over the Tokyo metropolitan area and the SBF-related vertical aerosol transport. The study applied a modified two-dimensional variational method to the Doppler lidar data of RHI scans to retrieve a two-dimensional flow structure at and around the SBF in north-south vertical cross sections.

The observations showed that the SBF had the characteristics of gravity currents. The observed propagation speed of the SBF was largely close to that calculated from the Doppler lidar and in-situ surface meteorological sensor data using a gravity-current model. It was found that the Froude number for the observed sea-breeze event compares favorably with those previously reported for SBFs in opposing flow cases and different atmospheric density currents such as gust fronts.

From the discussion based on an influence of relative humidity to the lidar reflectivity, significant enhancement of the ceilometer backscatter coefficient and Doppler lidar range-corrected SNR at lower levels mainly resulted in the aerosol concentration enhancement. It is probably an appropriate interpretation that the intense optical backscatter up to 2 km AGL observed by the ceilometer was a signature of the vertically transported aerosols from the lower level.

The Doppler lidar observed a strong updraft (maximum w approximately equal to 5 m s^{-1}) with a horizontal scale of about 500 m and a vertical scale of 2 km that formed over the nose of the SBF. Since a thermal existed about 1 km south of the Doppler lidar prior to the sea-breeze frontal passage, it is suggested that there was a contribution of the interaction between the SBF and thermal to the intensification of the updraft. After commencement of the updraft, the ceilometer observed an intense aerosol backscatter up to 2 km. Several minutes before and after this observation, the Doppler lidar detected no signature by which denser aerosol particles near the surface were vertically transported by the strong updraft over the nose of the SBF. The relationship between the strong updraft observed by the Doppler lidar and the intense optical backscatter observed by the ceilometer is discussed in every possible aspect. The observational results suggest that the near-surface denser aerosols trapped in the head region of the SBF escaped from its nose, then the aerosols was vertically transported up to the mixing height by the strong updraft over the nose. The results also imply that these phenomena occurred not continuously but intermittently. The escape of the near-surface denser aerosols trapped in the head region of the SBF may have been triggered by interaction between the SBF and the prefrontal thermal. Unfortunately, the Doppler lidar obtained no observations that identify the escape mechanism of the aerosols trapped in the head region of the SBF.

4.7 Appendix: Test for validity of two-dimensional flow assumptions

To retrieve the vertical air motion associated with the SBF from Doppler lidar data of RHI scans normal to the front using the equation of continuity, we made the following two assumptions: first, the variation of density with height is negligible; second, the flow can actually be considered two-dimensional.

Based on Wakimoto (1982), we have tested the validity of the two assumptions in this case.

4.7.1 Density variation with height

If the horizontal density variations are considered small and the flow is assumed to be two-dimensional (see next section) in a meridional cross section (i.e., $y - z$ plane), Eq. 2 of Wakimoto (1982) is modified to

$$\frac{\partial v}{\partial y}+\frac{\partial w}{\partial z}+\frac{1}{\rho}\frac{\partial \rho}{\partial z}w=0. \tag{4.13}$$

In order to assess the magnitude of the terms, the following scale analysis for the SBF is used: $V \approx 10$ m s^{-1}, $W \approx 5$ m s$^{-1} \approx V/2$, L ≈ 5 km, H ≈ 3 km $\approx 3L/5$, $\rho = \rho_0$, where V, W, L, and H are characteristic velocity and length scales estimated from Doppler lidar data of PPI and RHI scans (Figs. 4.9 and 4.10) and ρ_0 is a mean density. Applying these values to Eq. 4.13,

$$\frac{\partial v}{\partial y}=\frac{V}{L}, \tag{4.14a}$$

$$\frac{\partial \mathrm{w}}{\partial z}=\frac{5}{6}\frac{V}{L}, \tag{4.14b}$$

$$\frac{1}{\rho}\frac{\partial \rho}{\partial z}w=\frac{5}{6}\frac{\Delta\rho}{\rho_0}\frac{V}{L}. \tag{4.14c}$$

In this study, the vertical velocity is nearly zero at 2 km, which approximately corresponds to 800 hPa. Since the temperature differences in the vertical can be considered smaller than the pressure differences,

$$\frac{\Delta\rho}{\rho_0}\approx\frac{\Delta p}{p_0}\approx\frac{1}{5}, \tag{4.15}$$

where p_0 is a mean pressure and approximately equal to 1000 hPa in this study. Therefore, the scale analysis of Eq. 4.14c becomes

$$\frac{1}{\rho}\frac{\partial \rho}{\partial z}w=\frac{1}{6}\frac{V}{L}. \tag{4.16}$$

It is concluded from Eq. 4.16 that for a good approximation the density variation with height can be ignored. Previous aircraft-based observations of SBFs (Kraus et al. 1990; Finkele et al. 1995; Stephan et al. 1999; Wood et al. 1999) provided specific humidity and potential temperature at different heights. The variations between near the SBF top and the near surface of moist air density estimated from these data are about 10%. Using an instrumented tethered kite balloon, Lapworth (2000) also mentioned that a maximum variation between the top and the surface of air density is around 10%. Thus 10% variation of density with height in the SBF is accepted by these previous observational results. Although Eq. 4.15 overestimates the variation of density with height to the observational results, the fact remains that it is a valid assumption that density variation with height is negligible.

4.7.2 Two-dimensional assumption

The horizontal divergence can be calculated in the natural coordinate system shown in Fig. 2 of

Wakimoto (1982) using

$$\nabla_h \cdot \mathbf{V} = \frac{\partial V}{\partial s} + V \frac{\partial \theta}{\partial n}. \tag{4.17}$$

The first term $\partial V/\partial s$ is the longitudinal divergence and exceeds 8×10^{-3} s^{-1} at the SBF (Fig. 4.9e). The second term $V\partial\theta/\partial n$ is the transversal divergence and a measure of the diffluence of the wind. To assess the effect of the transversal divergence, we have estimated the following values: V = 9 m s^{-1}, $\Delta\theta$ = 12°, δ = 3 km (refer to Fig. 2 of Wakimoto (1982)). This leads to a value of $V\partial\theta/\partial n$ = 6.28×10^{-4} s^{-1}, for the transversal divergence. This is an order of magnitude smaller than the longitudinal divergence at the SBF. Thus, the flow can actually be considered two-dimensional.

5. CONVECTION INITIATION ASSOCIATED WITH AN ISOLATED CONVECTIVE STORM TRIGGERED BY A SEA-BREEZE FRONT

In this chapter, we present an observational study on a convection initiation associated with an isolated convective storm triggered by a sea-breeze front (SBF) in the Tokyo metropolitan area on 17 August 2012 using different remote sensing instruments. The Co2DiaWiL (hereafter Doppler lidar) and a C-band radar detected convergence line organized as an SBF moving inland from Tokyo Bay. The convergence at the convergence line and near-surface air parcel uplifting to its lifting condensation level (LCL) are discussed using Doppler lidar data. The Doppler lidar and wind profiler radar (WPR) data are applied to track the trajectory of the air parcel from the surface to its level of free convection (LFC). The role of the boundary layer thermals in an additional lifting for the air parcel from LCL to LFC is presented. The effect of the interaction between an SBF moving inland from Sagami Bay and the preexisting convective cell is discussed.

5.1 Introduction

Localized heavy rainfall can often cause flash flooding in densely populated urban areas of Japan. Although the Kanto Plain experiences relatively few thunderstorms in summer in comparison with mountainous areas lying to the north and west of the Kanto Plain (e.g., Horie and Tomine 1998), strong isolated thunderstorms develop occasionally and are particularly responsible for localized heavy rainfall and flooding in the Tokyo metropolitan area. For example, a thunderstorm that developed on 21 July 1999 in the southern Kanto Plain produced torrential rainfall in the Tokyo metropolitan area (Kobayashi et al. 2001; Kawabata et al. 2007; Seko et al. 2007). The maximum 1-hour rainfall amount was 111 mm at Nerima, and the flash flooding caused by this rainfall drowned one person in a basement. The flash flooding at Zoshigaya on 5 August 2008 was caused by isolated thunderstorms with localized heavy rainfall (Kato and Maki 2009; Hirano and Maki 2010; Kim et al. 2012; Ishihara 2012a, b). The flooding drowned five persons. Fujibe et al. (2002) have shown that a converging airflow pattern, which consists of easterly wind from Kashima-nada and southerly wind from Tokyo Bay and Sagami Bay, often tends to precede the onset of heavy rainfall in Tokyo. In the above cases of localized heavy rainfall at Nerima and Zoshigaya, deep convection was triggered by low-level convergence lines.

Convergence lines (regions of low-level convergence of air arranged along a line; Bennett et al. 2006) are sometimes precursors to convection initiation in the absence of large-scale forcing. Using Doppler radar data in the plains of eastern Colorado, Wilson and Schreiber (1986) showed that convergence lines could be identified as lines of enhanced radar reflectivity and that convection initiation was closely related to the convergence lines. Examples of convergence lines include outflow boundaries (e.g., Kingsmill 1995), drylines (e.g., Ziegler et al. 1997), cold fronts (e.g., Koch and Clark 1999), and sea breezes (e.g., Lhermitte and Gilet 1975). SBFs are boundaries between the warm air over the land and the cool marine air, and the

associated convergence lines can sometimes trigger convection along SBFs. There have been a large number of studies on sea-breeze-induced convection initiation in the United States. In the Convection and Precipitation/Electrification (CaPE) project, which was carried out in Florida during the summer of 1991, Wakimoto and Atkins (1994) and Atkins et al. (1995) showed that intersections of horizontal convective rolls with SBFs were preferential areas of convection initiation.

The Kanto Plain is known for sea breezes resulting in convergence lines, and the SBFs are important triggering mechanisms of deep convection. However, only a few detailed observational studies of convection initiation associated with sea breezes have been reported. Kobayashi et al. (2007) observed an isolated cumulonimbus initiation using an X-band Doppler radar and Doppler sodars in the Tokyo metropolitan area in the summer of 2004. They showed that convection initiation triggered by a surface wind shear line formed in a heat low, and a radar echo was intensified by a stationary SBF. Kusunoki et al. (2012) reported a case study of convection initiation using a C-band Doppler radar in the Tokyo metropolitan area in the summer of 2011. They showed that several convections initiated along convergence lines organized as an SBF moving inland from Tokyo Bay. The above studies showed that sea breezes play an important role in the initiation and development of convection in the Kanto Plain.

The prediction of small-scale convective storms with weak forcing is still a challenge in numerical weather prediction (Kawabata et al. 2011). A major difficulty in predicting convective storms is in predicting the timing and location of new convection. The mechanisms leading to convection initiation are inadequately understood in the Kanto Plain because it is difficult to observe the mesoscale pre-storm environment, particularly for features such as convergence lines. Field experiments were performed on convection initiation in the Great Plains of the United States (the International H_2O Project (IHOP); Weckwerth et al. 2004), the southern United Kingdom (the Convective Storm Initiation Project; Browning et al. 2007), and the southwestern Germany and eastern France (the Convective and Orographically-induced Precipitation Study (COPS); Wulfmeyer et al. 2008). Although there are similarities between the mechanisms leading to convection initiation in the Kanto Plain and those described in the previous studies, the dominant factors may be different because the Kanto Plain is a highly developed and urbanized area with a relatively flat topography and fronts the Pacific Ocean, Tokyo Bay, and Sagami Bay.

This study is based on data from a field program called the Tokyo Metropolitan Area Convection Study for Extreme Weather Resilient Cities (TOMACS; Nakatani et al. 2015). The aim of TOMACS is to collect data to help improve the monitoring and prediction of extreme weather as a step toward decreasing the damage caused by severe local weather phenomena such as wind gusts and floods (Maki et al. 2012). In this paper, we present an observational case study of an isolated convective storm that formed over the southern Kanto Plain on 17 August 2012. The structure and evolution of isolated convective storms are important topics of active research; however, in this study, we focus only on the early stages of the convective storm. The goal of this study is to clarify the dynamics leading to the convection initiation of the storm using different remote sensing instruments. The key measurement systems used in this study were a Doppler lidar, a WPR, a Ku-band radar, and a C-band radar. The Ku-band radar provided the

detailed features of the initiation and development of deep convection. The Doppler lidar and C-band radar detected convergence lines caused by the initiation of deep convection. Using a vertical beam, the WPR directly and continuously observed an air parcel that reached its lifting condensation level (LCL) and level of free convection (LFC) and then rose with a significant updraft. Direct and continuous observations of rising air parcels resulting in convection initiation have been rarely made in previous studies. Although Karan and Knupp (2006) and Demoz et al. (2006) observed vertical velocities at convergence lines using WPRs during IHOP, they could not observe the vertical velocities at locations of convection initiation. In situ aircraft and airborne Doppler radar observations of vertical velocities at convergence lines were conducted during IHOP and COPS (e.g., Wakimoto et al. 2006; Behrendt et al. 2011). Although airborne instruments yield a spatially detailed description of the convergence line structure, continuous measurements at locations of convection initiation are difficult. Therefore, observational data and knowledge at the location of convection initiation obtained by the present case study are important and valuable.

Section 5.2 describes a summary of observational data. Section 5.3 presents the synoptic conditions and the evolution of deep convection based on the C-band and Ku-band radar data. Section 5.4 presents observational results leading to convection initiation, with discussion provided in Section 5.5. A summary follows in Section 5.6.

5.2 Observational data

The arrangement of observational instruments used in this study is shown in Fig. 5.1. The Doppler lidar was stationed on the rooftop of a building at the NICT headquarters (35.71°N, 139.49°E, height 75 m above mean sea level (AMSL), denoted by the open square in Fig. 5.1), 20 m above ground level (AGL). The specifications of the Doppler lidar are described in Section 2.2. In this experiment, the range gates had a length of about 76 m with the center of the first gate at 150 m. With 80 range gates per beam, the maximum range was about 6 km depending on the

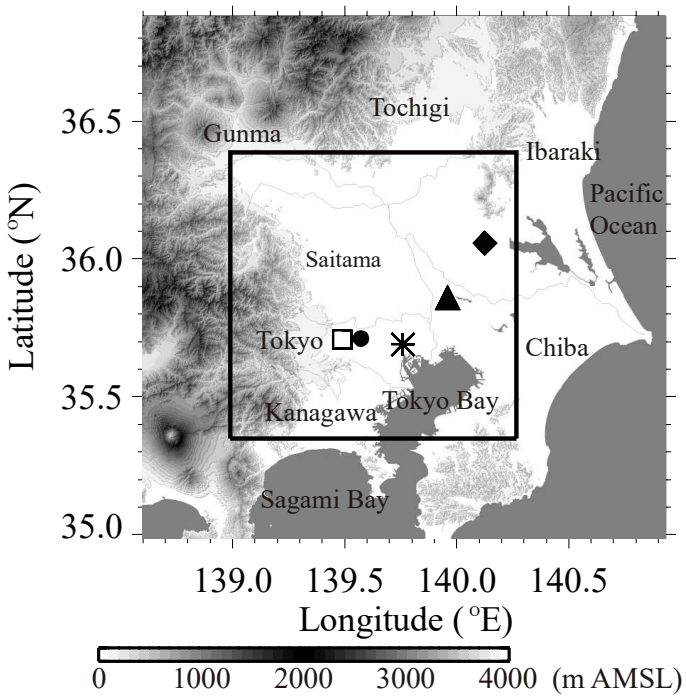

Figure 5.1. Map and topography of the Kanto District. The grayscale bar indicates height in meters above mean sea level (m AMSL). The open square, closed circle, closed triangle, closed diamond, and asterisk indicate the locations of the Doppler lidar (NICT headquarters), Ku-band radar, C-band radar, upper-air sounding station (Tateno), and AMeDAS Tokyo site, respectively. The rectangle delineates the area displayed in Fig. 5.5.

aerosol load present. Plan position indicator (PPI) and range height indicator (RHI) scans were alternately performed.

The WPR was developed on the base of the 1.3-GHz WPR referred to as LQ-7 (Imai et al. 2007). The location of the WPR was about 450 m south of the Doppler lidar. The WPR has a phased array antenna composed of four Luneburg lenses of 800 mm diameter. The center frequency is 1357.5 MHz and the peak output power is 1600 W. Each lens has five feeds directed toward the vertical direction and four inclined directions (north, east, south, and west) with a zenith angle of 14°. The WPR measured radial velocities at each beam direction with a range resolution of 100 m every 1 min. The maximum range is 8 km with 80 range gates per beam. The horizontal winds are estimated by the Doppler beam swinging (DBS) technique from four inclined beams. WPRs are sensitive to refractive index fluctuations in clear air. In the boundary layer, humidity mainly affects the refractive index.

The Ku-band radar was installed on the roof of a building of Seikei University, Musashino, Tokyo, Japan (35.62°N, 139.36°E, height 65 m AMSL denoted by the closed circle in Fig. 5.1) and operated by the Meteorological Research Institute (MRI; Sato et al. 2013). In order to achieve a high range resolution (2.38 m), the Ku-band radar transmits and receives wideband (80 MHz (max)) signals at 15.75 GHz using pulse compression (Mega et al. 2007; Yoshikawa et al. 2010). The Ku-band radar has a bistatic antenna system composed of two primary feeds and two 450-mm-diameter Luneburg lenses with a beamwidth of 3°. The Ku-band radar was operated in the spiral scan mode to observe radar reflectivities and Doppler velocities in the whole sky with an update rate of about 1 min. Although the maximum observation range (19.5 km) is limited due to strong precipitation attenuation in the Ku band, the Ku-band radar can observe the precipitation with high temporal and spatial resolution. The observed radar reflectivities and Doppler velocities are interpolated in a Cartesian grid system with a horizontal and vertical spacing of 200 m using a Cressman weighting function (Cressman 1959).

The Japan Meteorological Agency (JMA) C-band operational radar is located in Kashiwa, Chiba, Japan (35.86°N, 139.96°E, height 74 m AMSL denoted by the closed triangle in Fig. 5.1). The range and azimuthal resolutions are 500 m and 0.7°, respectively. Doppler velocity and radar reflectivity data were collected at 13 and 26 elevations every 10 min, respectively. The C-band radar, which has high sensitivity, provided the observations of optically-clear-air echoes in the boundary layer. Convergence lines are typically formed as lines of enhanced radar reflectivity with a width of 1–3 km (e.g., Wilson and Schreiber 1986). The clear-air echoes have radar reflectivity values of over 0 dBZ and typical values are 10–20 dBZ over the Kanto Plain (Kusunoki and Matsumura 1999; Kusunoki 2002).

An in-situ surface meteorological sensor (Vaisala WXT520) was mounted on a tower at the NICT headquarters (55 m AGL) for measuring wind speed, wind direction, barometric pressure, temperature, and relative humidity. The location of the sensor was about 120 m south of the Doppler lidar. Data are recorded every minute. A ceilometer (Vaisala CT25K) was deployed on the ground and placed about 50 m north-west of the Doppler lidar. It measures the optical backscattering coefficient of the air at a wavelength of 905 nm. It can retrieve cloud base heights every 15 sec up to 7.5 km above the ground with a vertical resolution of 30 m.

Surface meteorological data observed using the Automated Meteorological Data Acquisition System (AMeDAS) Tokyo site (35.69°N, 139.76°E, height 6.1 m AMSL denoted by the plus sign in Fig. 5.1), MTSAT-1R data, upper sounding data at Tateno (36.05°N, 140.13°E, height 31 m AMSL; denoted by the asterisk in Fig. 5.1), mesoscale objective analysis (MANAL) data, and weather charts published by the JMA were also used for the analysis. Geolocation errors in the MTSAT-1R visible images were corrected by match-ups comparing coastlines indicated in the images with their known geographic locations (Saito et al. 2013).

5.3 Overview of the event

5.3.1 Synoptic conditions

Figure 5.2 shows the surface weather chart at 0900 JST on 17 August 2012. The Japanese archipelago was subject to a weak pressure gradient that stretched from a Pacific high over the northern Pacific Ocean to a typhoon over the South China Sea. The location of the typhoon is out of the display range of the weather chart. A stationary front was situated in the Tohoku area. Thus, the Kanto Plain was subjected to the effect of the Pacific high, and weak surface pressure gradients allowed the formation of thermally induced wind systems in the area of interest. The 500-hPa weather chart (not shown) at 0900 JST shows that a trough with cold air of –6 °C was present over the Japan Sea, which was moving eastward at 2100 JST. It is suggested that the Kanto Plain was covered with air at about –6 °C at the 500-hPa level at 1500 JST.

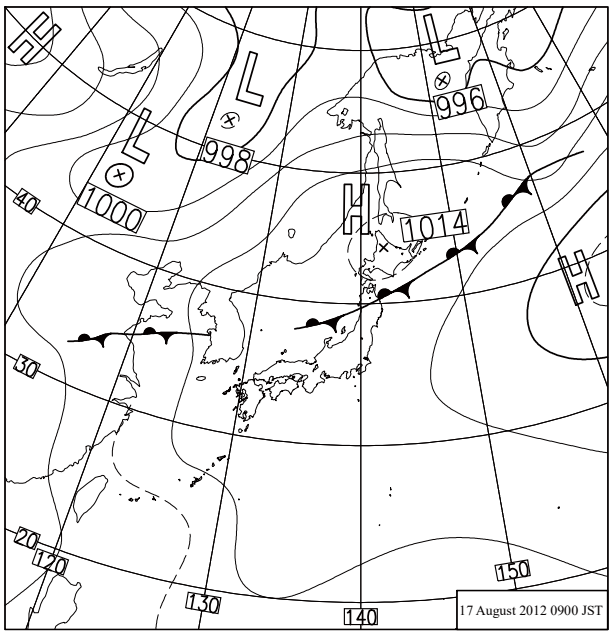

Figure 5.2. Surface weather map at 0900 JST on 17 August 2012 (from JMA monthly report).

Upper sounding data observed at Tateno at 0900 JST on 17 August 2012 (Fig. 5.3a) showed that the atmosphere below 500 hPa was in a state of conditional instability. The estimated LCL and LFC of lifting air parcel originating from the lowest 500 m of the atmosphere were at approximately 800 m and 2 km, respectively. The convective available potential energy (CAPE) and convective inhibition (CIN) calculated from this originating level were 1291 J kg^{-1} and 67 J kg^{-1}, respectively. Chuda and Niino (2005) reported that the monthly median CAPE at Tateno at 0900 JST in August from 1990 to 1999 was 1168 J kg^{-1}. Thus, the above CAPE had an ordinary value. The equilibrium level was at about 14 km. Figure 5.3b shows vertical profiles of potential temperature, equivalent potential temperature, and saturated equivalent potential temperature at the NICT headquarters calculated from MANAL data about 40 min before the storm developed over the NICT headquarters (1500 JST). The atmosphere below the 500-hPa level was in a state of conditional instability. By this time, the CAPE had increased to approximately 2000 J kg^{-1} and the CIN was approximately 100 J kg^{-1}. While the LCL ascended to approximately 1.5 km, the LFC slightly descended to approximately 1.8 km. Although the CAPE became high, a strong trigger is necessary for the occurrence of storms over a flat terrain to lift low-level moist air to the LFC. The equilibrium level was at about 14 km, which is the same as that at 0900 JST at Tateno. If convection reached the LFC, it would have been possible for deep convective clouds to develop. The wind profile at 0900 JST at Tateno was characterized by moderate east-northeasterly flow below 3 km, and the vertical wind shear between the lowest layer and 1 km was approximately 5×10^{-3} s^{-1}. Between 3 and 7 km, there was weak wind. At 1500 JST at the NICT headquarters, a weak east-southeasterly to east-northeasterly flow blew below 2 km, and

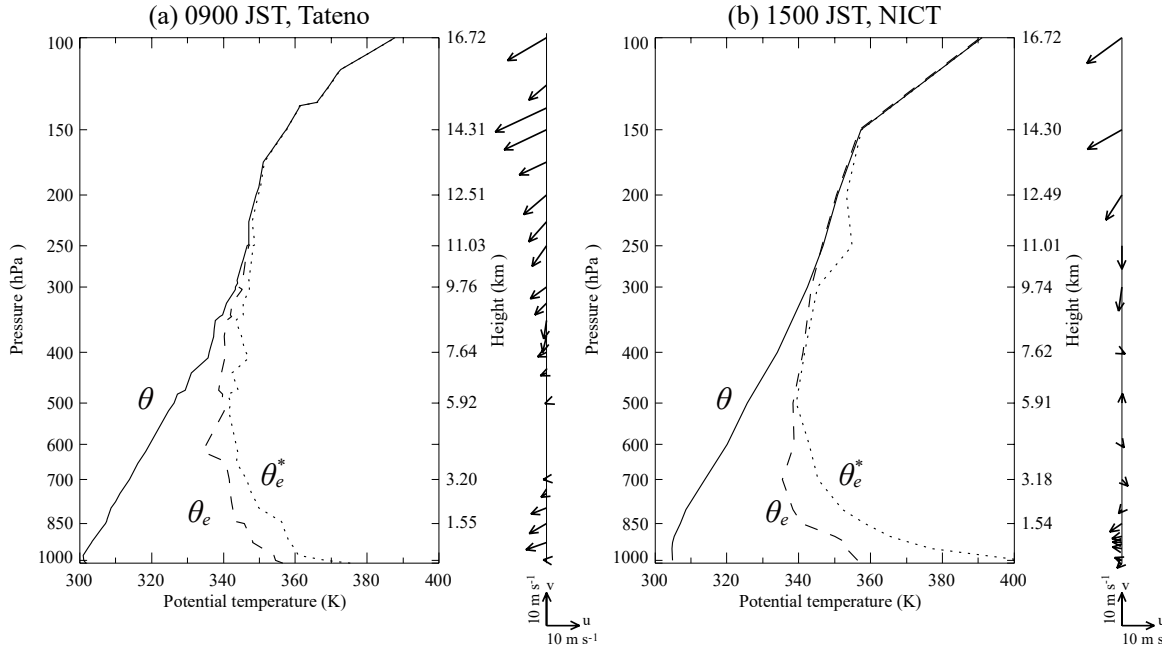

Figure 5.3. Vertical profiles of potential temperature (solid lines), equivalent potential temperature (dashed lines), saturated equivalent potential temperature (dotted lines), and horizontal wind vector (arrows) at (a) 0900 JST on 17 August 2012 at Tateno derived from upper sounding data and (b) 1500 JST on 17 August 2012 at NICT headquarters calculated from MANAL data.

the vertical wind shear between the lowest layer and 1 km was approximately 2×10^{-3} s^{-1}. Between 2 and 8 km, there was weak wind. Therefore, the vertical wind shear was weak.

Figure 5.4 shows the horizontal distribution of equivalent potential temperature (θ_e) and horizontal wind near the surface at 0900 JST (Fig. 5.4a) and 1500 JST (Fig. 5.4b) on 17 August 2012, which were obtained using the MANAL data. At 0900 JST, weak northerly wind was dominant around the southern Kanto Plain (Fig. 5.4a). At 1500 JST, a high-θ_e airmass moved into the southern Kanto Plain from Tokyo Bay and Sagami Bay (Fig. 5.4b). The southeasterly winds from Tokyo Bay covered the observation site, and the southerly winds from Sagami Bay moved further inland.

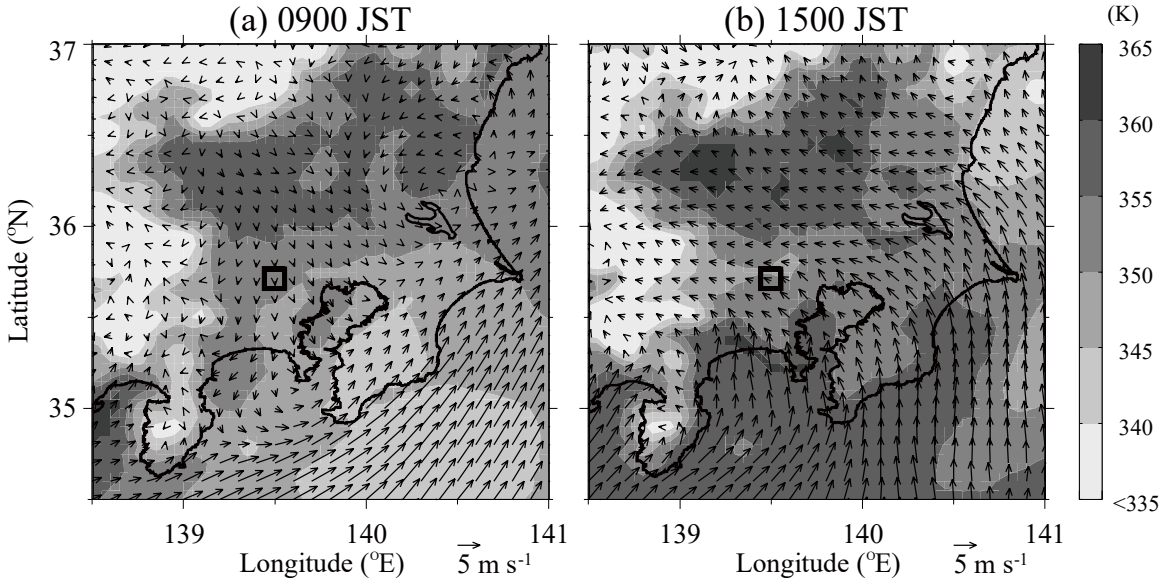

Figure 5.4. Horizontal distributions of equivalent potential temperature (shading) and horizontal wind (arrows) around the surface at (a) 0900 and (b) 1500 JST on 17 August 2012 given by the MANAL data. The open square indicates the location of the Doppler lidar (NICT headquarters).

5.3.2 Evolution of deep convection

On 17 August 2012, convective rainfall had already begun in the morning in the surrounding mountainous areas lying to the north and west of the Kanto Plain. At 1400 JST, convective rainfall also began in the northern part of the Kanto Plain (Fig. 5.5a). Clear-air echoes were detected within the 30-km range of the C-band radar. The radar reflectivity field showed no echoes around the Doppler lidar site. At 1450 JST, a weak radar echo formed at 2 km west of the Doppler lidar site (Fig. 5.5b), but it had dissipated 10 min later (not shown). An examined isolated convective storm was initiated at 1545 JST (Fig. 5.5c) and slowly moved to the west. The storm rapidly became enhanced, having a diameter of 10 km, with a maximum radar reflectivity of 57 dBZ (Fig. 5.5d).

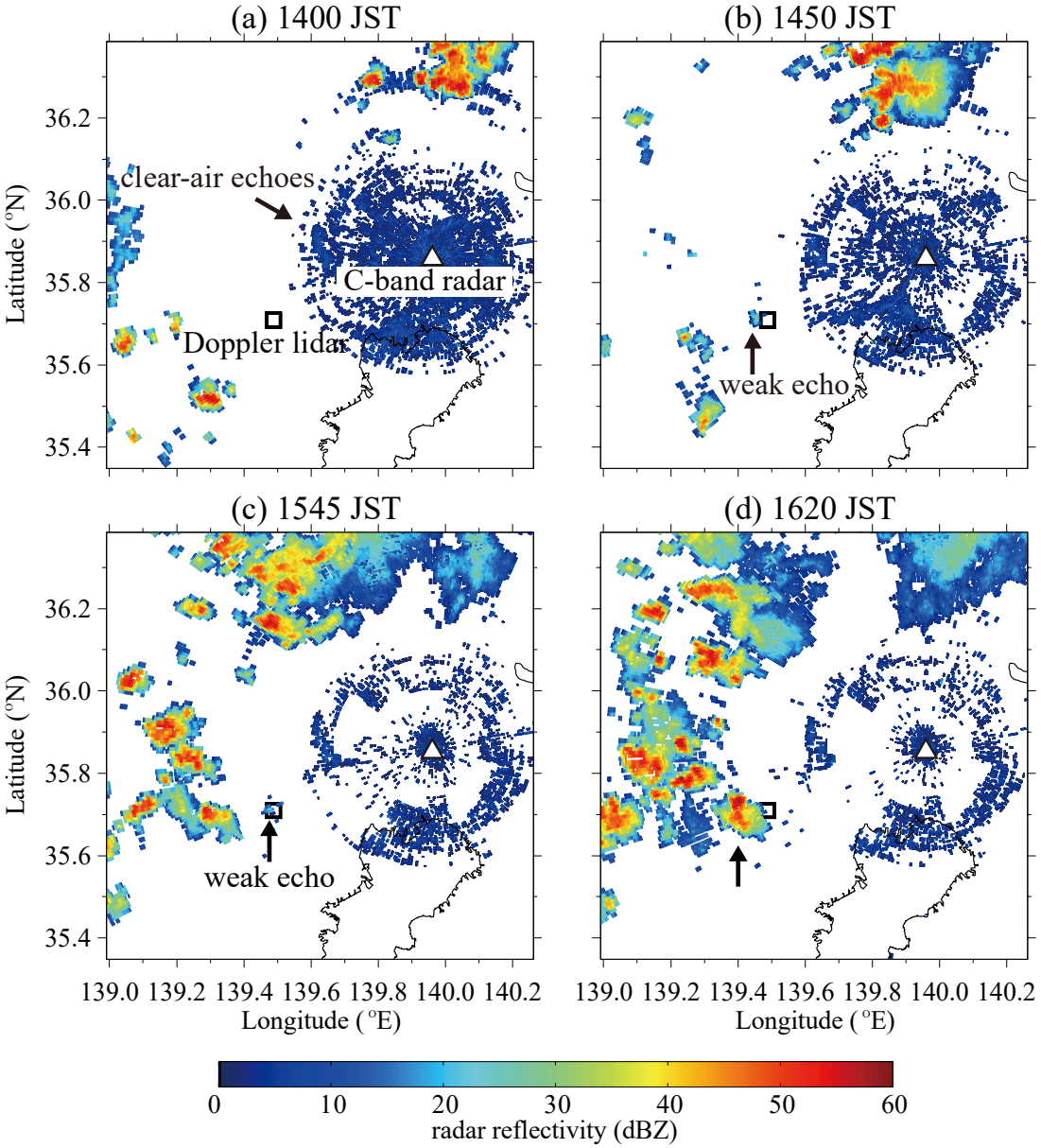

Figure 5.5. Radar reflectivity (dBZ) at 2.0° elevation angle from the C-band radar at (a) 1400, (b) 1450, (c) 1545, and (d) 1620 JST on 17 August 2012. The open square and open triangle indicate the locations of the Doppler lidar and C-band radar, respectively.

Figure 5.6 shows the evolution of the radar reflectivity observed by the Ku-band radar. At 1541:30 JST, the Ku-band radar detected the first weak echo of hydrometeors about 1 km north-northeast of the Doppler lidar at 4 km AGL (Fig. 5.6a). The precipitation cell grew quickly and the radar reflectivity of the precipitation core reached 40 dBZ at 1546:50 JST (Fig. 5.6b). At 1552:10 JST, the convective cell

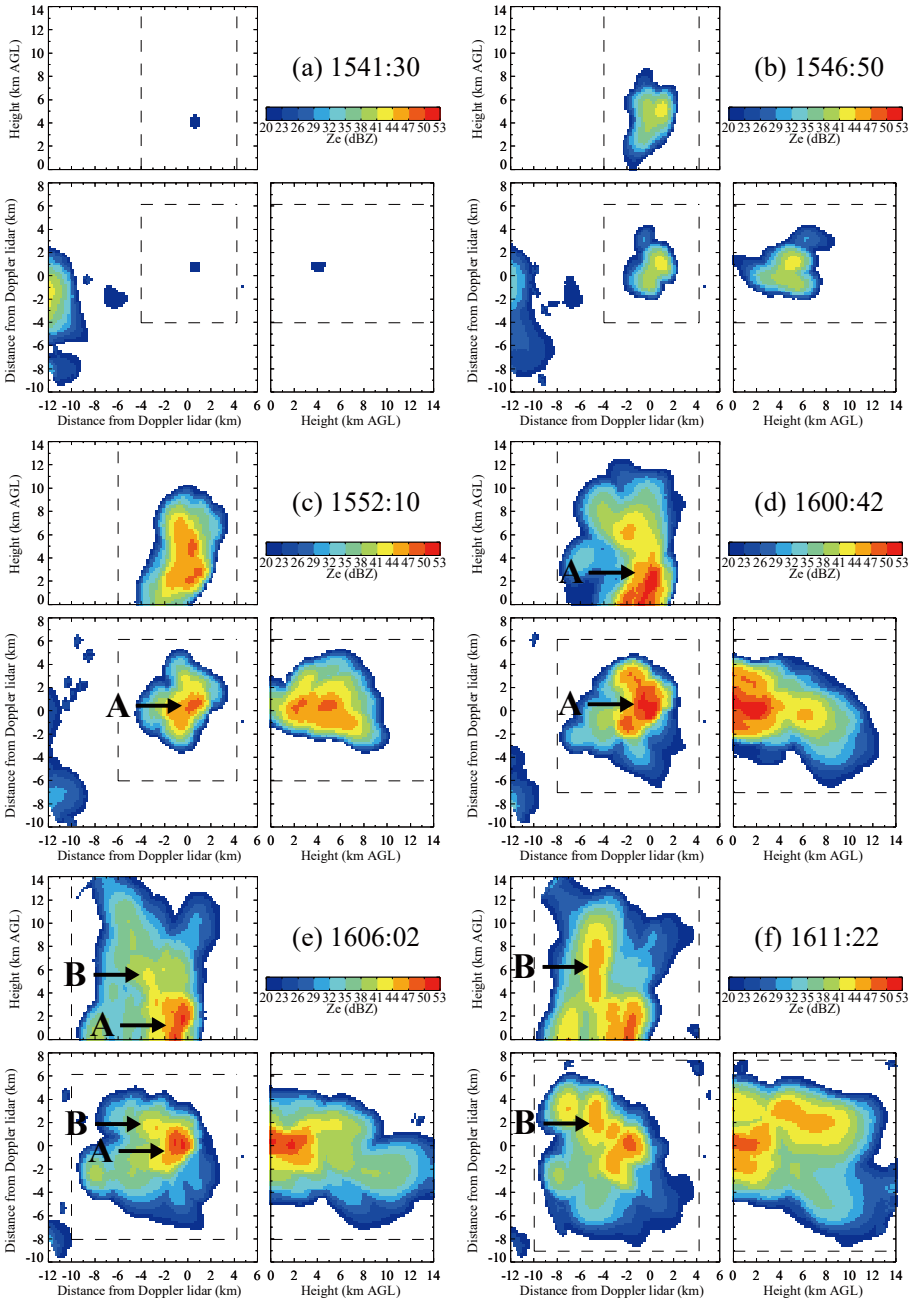

Figure 5.6. Radar reflectivity (dBZ) measured by the Ku-band radar at (a) 1541:30, (b) 1546:50, (c) 1552:10, (d) 1600:42, (e) 1606:02, and (f) 1611:22 JST on 17 August 2012. The images display the (bottom left) maximum radar reflectivity inside the dashed rectangle observed in a vertical column projected on the x-y-plane, (top left) the maximum radar reflectivity observed in a north-south slice projected on the x-z-plane, and (bottom right) the maximum radar reflectivity observed in an east-west slice projected on the y-z-plane. The arrows labeled A and B indicate precipitation cells.

developed up to a height of 10 km AGL, and two precipitation cores with a radar reflectivity of about 50 dBZ were formed at 2.5 and 5 km altitudes (Fig. 5.6c). The precipitation cores merged and descended to a 2 km altitude at 1600:42 JST (Fig. 5.6d). At 1606:02 JST, while precipitation cell A decayed, a new precipitation cell B with a radar reflectivity of over 40 dBZ developed at an altitude of 5–6 km about 2 km

north and 3 km west of the Doppler lidar (Fig. 5.6e). The 20-dBZ echo-top height is over the equilibrium level of about 14 km (Section 5.3.1). This means that a rising air parcel was not cut off at the equilibrium level and implies a strong updraft. At 1611:22 JST, precipitation cell B rapidly grew, had a radar reflectivity of over 45 dBZ, and extended up to 10 km AGL (Fig. 5.6f). Then cell B grew rapidly (not shown). After about 30 min (1650 JST), precipitation cell B dissipated (not shown).

5.4 Convection initiation by boundary layer processes

A combination of surface meteorological sensors, C-band radar, Doppler lidar, and WPR observational results were used to evaluate the precursors to convection initiation. The convection initiation occurred directly above the Doppler lidar and WPR at 1541:30 JST (Fig. 5.6a). Before the convection initiation, the C-band radar detected a convergence line in the form of an SBF moving inland from Tokyo Bay. The Doppler lidar detected a convergence zone that formed the west edge of the convergence line. The near-surface air parcel was lifted to its LCL by the updraft in the convergence zone. The rising air parcel from the LCL to the LFC and above the LFC was directly and continuously observed by the WPR. After the convection initiation, another convergence line, which formed an SBF moving inland from Sagami Bay, passed through the NICT headquarters (1554 JST). When the SBF passed under the precipitation cell, the updraft over the nose of the SBF triggered a new precipitation cell (Fig. 5.6e).

5.4.1 Surface and boundary layer conditions

Figures 5.7a and 5.7b show the time series of surface meteorological data at the AMeDAS Tokyo site and NICT headquarters. Until 1400 JST, the weak northerly flow gradually veered to the east accompanied by an increase in temperature and a decrease in mixing ratio at the AMeDAS Tokyo site and NICT headquarters. At the AMeDAS Tokyo site, the temperature decreased from 35.3 to 34.8 °C and the mixing ratio increased from 18.4 to 19.7 g kg^{-1} at 1430 JST. Then the temperature gradually decreased, and the mixing ratio had an increase tendency until 1510 JST. 10 min after the change of temperature and mixing ratio, the surface wind speed increased. These time series suggest the passage of a frontal structure. The time lag between changes in the temperature/mixing ratio and the wind speed is probably the difference between locations of the thermodynamic and kinematic fronts (Atkins et al. 1995). At the NICT headquarters, between 1500 and 1545 JST, the mixing ratio increased from 15 to 16 g kg^{-1}, the surface wind speed increased from 2 to 4 m s^{-1}, and the wind direction shifted from east to southeast. This suggests that the southeasterly flow transported moist air. A distinct surface wind shift and wind speed increase accompanied a cold frontal passage at 1554 JST.

Figure 5.7c shows vertical profiles of the horizontal flow (30-min averages) observed by the WPR from 0800 to 1800 JST at the NICT headquarters. Vertical profiles of horizontal wind observed by the WPR portray a small change in the wind direction and weak vertical wind shear. Just before the storm developed over the NICT headquarters (1500 JST), a weak east-southeasterly to east-northeasterly flow blew below 2 km. The cumulus cloud base heights were observed by the ceilometer between 1000 and

1600 JST. The cumulus cloud base heights increased from 1 km AMSL at 1000 JST to 2 km AMSL at 1500 JST and got lower to 1.5 km at 1520 JST.

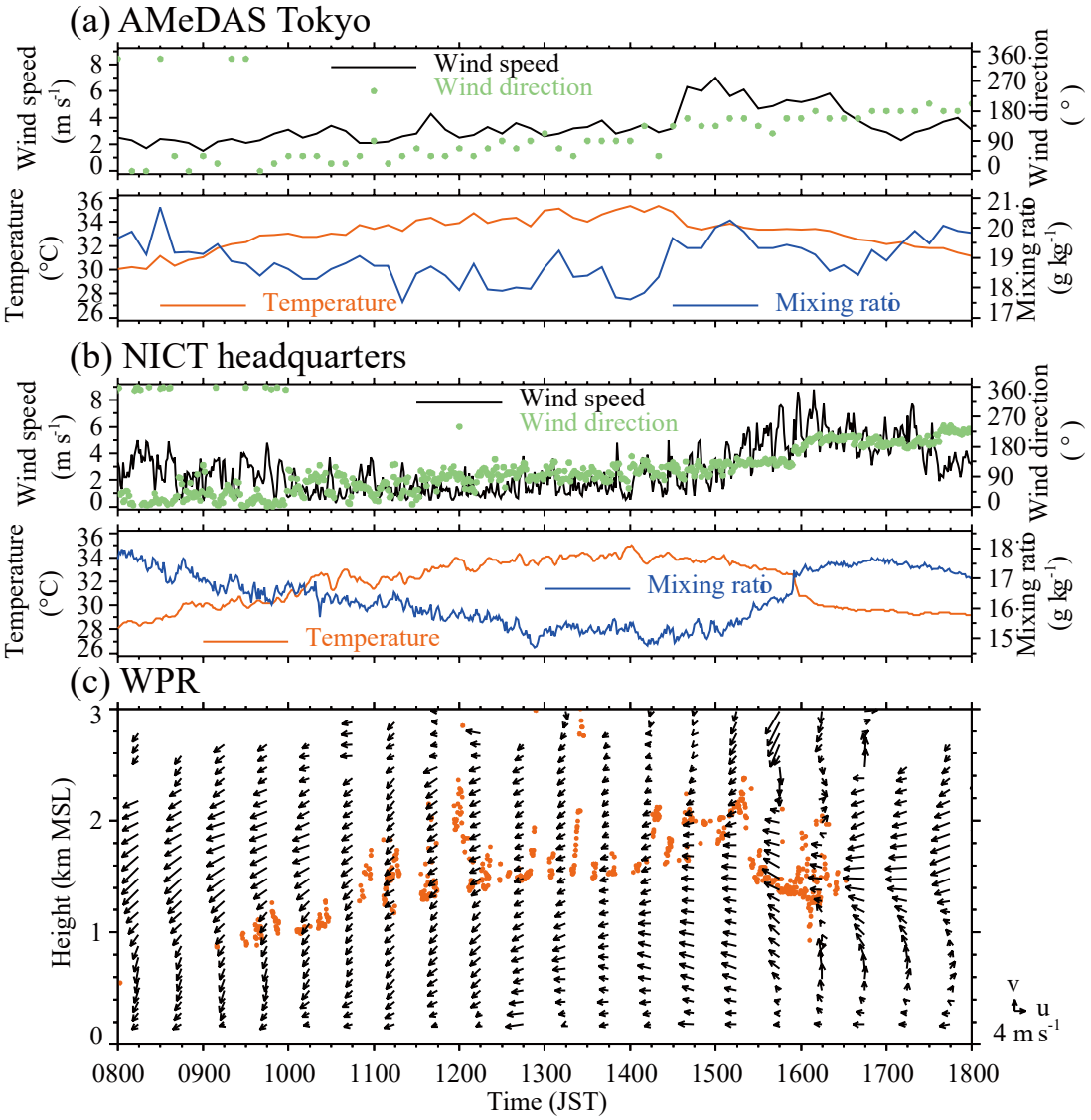

Figure 5.7. Time series of wind speed (m s^{-1}), wind direction (green; °), temperature (red; °C), and mixing ratio (blue; g kg^{-1}) between 0800 and 1800 JST on 17 August 2012 (a) at the AMeDAS Tokyo site and (b) at the NICT headquarters. (c) The 30-min averaged horizontal wind (arrows) in a vertical profile observed by the WPR. The red closed circles indicate the height of the cloud base derived from the ceilometer.

5.4.2 Convergence lines

Figure 5.8 shows radar reflectivities at 1.1° and 0.7° elevation angles from the C-band radar at 1517 JST and time series of convergence lines. The thin line (approximately 3 km in width) of enhanced radar reflectivity in Fig. 5.8a has an east-northeast to west-southwest orientation. The depth of the line is about 900 m. The western edge of the line was located at the eastern edge of the Doppler lidar observation area.

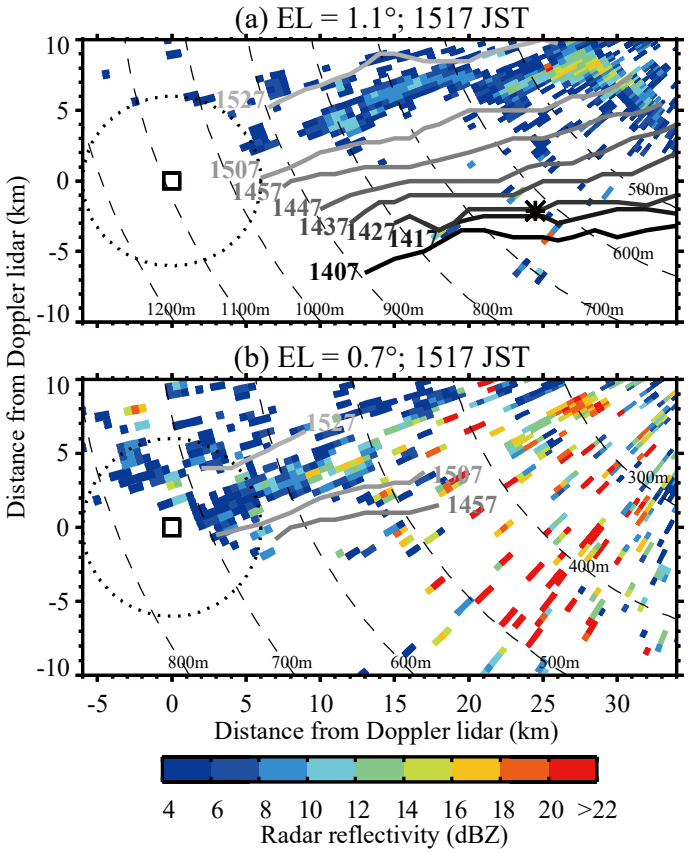

Figure 5.8. Radar reflectivities at (a) 1.1° and (b) 0.7° elevation angles from the C-band radar at 1517 JST on 17 August 2012. Time series of convergence lines detected at 1.1° and 0.7° elevation angles are superimposed as solid lines on the radar reflectivities. The open square indicates the location of the Doppler lidar (NICT headquarters). The dotted circle encompasses the observation area of the Doppler lidar. The dashed arcs represent the observation heights (AMSL) of the C-band radar. In Fig. 5.8a, the asterisk indicates the location of the AMeDAS Tokyo site.

On the other hand, the western edge of the line at 0.7° elevation angle was located inside the Doppler lidar observation area (Fig. 5.8b). The line was moving north-northwest. The line passed the AMeDAS Tokyo site at 1427 JST. It seems that the line was organized as an SBF moving inland from Tokyo Bay.

Figure 5.9a shows the radial wind component of the Doppler lidar, measured in a PPI scan at 4° elevation angle at 1517 JST. A southeasterly flow prevailed over the observed region. The convergence line detected by the C-band radar is indicated in Fig. 5.9a. Flows A and B are the sea breeze from Tokyo Bay, and flow C is the weak easterly flow ahead of the SBF (see Fig. 5.13b). Figure 5.9b shows the perturbation Doppler velocity, which is derived by subtracting the VAD-retrieved mean horizontal wind velocity from the Doppler velocity (Browning and Wexler 1968; Oda et al. 2011). At about 3 km east to north-east of the Doppler lidar, the wind field changed considerably. The locations of the local maximum of the convergence in the radial direction ($-dV_r'/dr$) are defined as the "convergence points" (gray open squares in Fig. 5.9b). An outbound-to-inbound direction change implies that radial velocities converge at the convergence points. Note that the convergence points were coincident with the western edge of the

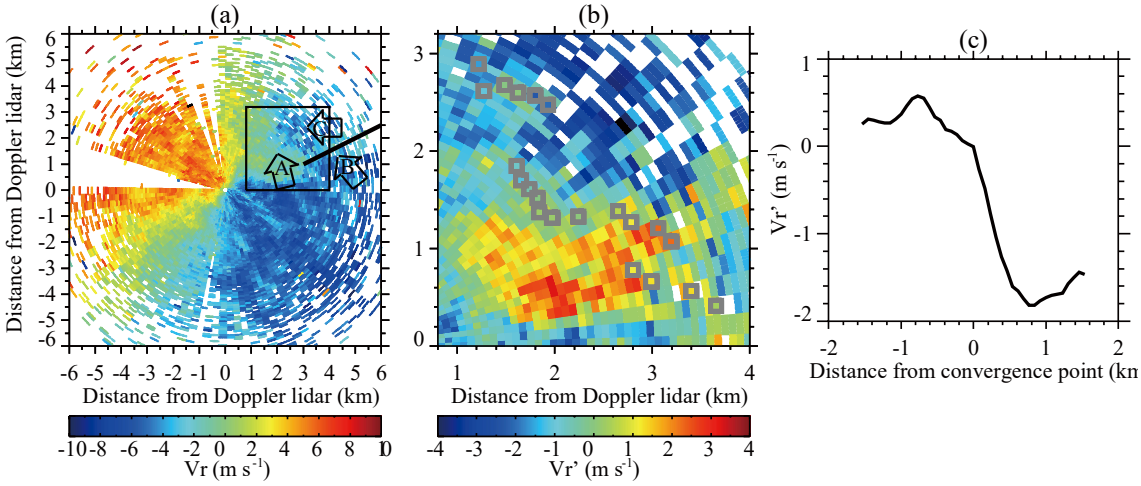

Figure 5.9. Doppler lidar 4°-elevation PPI scan of the (a) Doppler velocity (V_r) and (b) perturbation Doppler velocity ($V_r^{'}$) at 1517 JST on 17 August 2012. The perturbation Doppler velocity is derived by subtracting the VAD-retrieved mean horizontal wind velocity from the Doppler velocity. The black square in Fig. 5.9a denotes the area displayed in Fig. 5.9b. The thick solid line in Fig. 5.9a indicates the convergence line detected by the C-band radar. The gray open squares in Fig. 5.9b indicate the locations of the local maximum of the convergence in the radial direction ($-dV_r^{'}/dr$), defined as the "convergence points". (c) Composite profile of the perturbation Doppler velocity along the radial direction. Perturbation Doppler velocities were averaged along the convergence points in the azimuthal direction.

enhanced thin line of radar reflectivity (Fig. 5.8b). Figure 5.9c shows a composite profile of the perturbation Doppler velocity along the radial direction inside the 3-km scale convergence zone. In the radial direction, a 7-point simple moving average was applied to eliminate small-scale variability below several hundred meters along the radial direction. In the azimuthal direction, perturbation Doppler velocities were averaged along the convergence points in the convergence zone. The convergence at the convergence zone is about 1.5×10^{-3} s^{-1}. Since the convergence line is parallel to the Doppler lidar radial direction, the tangential velocity components are not known and the convergence between flows B and C cannot be estimated.

Another enhanced thin line of radar reflectivity detected by the C-band radar (i.e., a convergence line), which has a north-northwest to south-southeast orientation, was located about 6 km southwest of the Doppler lidar at 1537 JST (not shown). Figure 5.10 shows the entire convergence line B at 1552 JST. Line B was an SBF moving inland from Sagami Bay, which can be seen from the spatial relationship between line B and the convergence of the surface wind fields at 1600 JST. Line A was the SBF moving inland from Tokyo Bay shown in Fig. 5.8. Line B was moving northeast and approached the Doppler lidar site. A convective cell on line B was observed beside the Doppler lidar site by the C-band radar. The convective cell was also detected by the Ku-band radar (Fig. 5.6c). This indicates that line B passed under the existing convective cell. The sea-breeze frontal passage at the Doppler lidar site was detected at 1554 JST by the surface meteorological sensor (Fig. 5.7b).

Starting at 1543 JST, the Doppler lidar east-west RHI scans indicated the SBF associated with convergence line B (Fig. 5.11a). Figure 5.11b shows that the SBF exhibits typical gravity current or density current structure (Simpson 1994). The structure of the SBF is similar to that presented in Chapter 4 (Fig. 4.10c). Figure 5.11c shows an east-west vertical cross section of Doppler velocities at 1553 JST. A strong radial velocity (about 10 m s^{-1}) was observed over the nose of the SBF. The height of the cloud base, estimated using the empirical threshold level of the range-corrected SNR (0 dB), is about 0.8 to 1.4 km AGL. Figure 5.11d shows the vertical profile of the zonal wind derived by the WPR at 1553 JST. An easterly flow is evident up to 1.5 km AGL, and the easterly wind speed at 1.4 km AGL was 4.66 m s^{-1}. Since the Doppler velocity at 1.4 km west of the Doppler lidar and 1.4 km AGL was 9.16 m s^{-1}, the vertical velocity contributed to the Doppler velocity and was estimated to be 8.29 m s^{-1}. It is suggested that the strong updraft over the nose of the SBF reached the cloud base. Unfortunately, the WPR did not detect the updraft because the strong echo from the heavy rainfall completely obscured the clear-air echo.

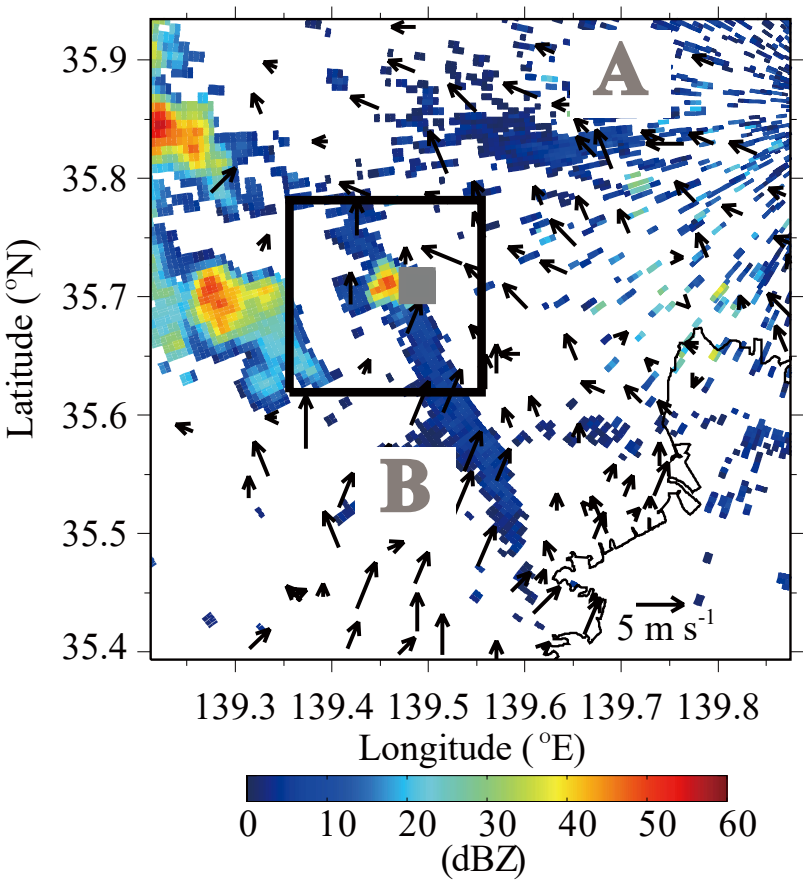

Figure 5.10. Surface wind fields (black arrows) observed by ambient air pollution monitoring stations at 1600 JST on 17 August 2012 superimposed on radar reflectivity (dBZ) at 0.7° elevation angle at 1552 JST from the C-band radar. The gray square indicates the location of the Doppler lidar. Labels A and B indicate the enhanced thin lines of radar reflectivity. The rectangle delineates the area of the x-y-plane displayed in Fig. 5.6.

5.4.3 Convection initiation

Figure 5.12 shows the temporal evolution of the boundary layer measured by the Doppler lidar between 1300 and 1600 JST. A well-mixed and cumulus-cloud-topped convective boundary layer developed. The growth of thermals in the boundary layer is considerable, and the thermals reached the cloud base. Cumulus clouds were prevalent throughout the NICT headquarters at 1432 JST (Figs. 5.13a and 5.13c). These cumulus clouds produced very weak precipitation 2 km west of the NICT headquarters at 1450 JST (Fig. 5.5b), but there was no indication of deep convection near the NICT headquarters. Since the Doppler lidar and C-band radar did not detect convergence lines and horizontal convective rolls in the precipitation area (not shown), the precipitation was produced by the cumulus clouds, which was triggered by the thermals. This suggests that the thermal updraft was insufficient to sustain the precipitation clouds against entrainment in the dry air above the boundary layer. At 1530 JST an optically thick cloud covered the NICT headquarters (Fig. 5.13d). After 1525 JST the strong updraft (>3 m s^{-1}) continued at and below the cloud base (Fig. 5.12). The updraft should be more conducive to convection initiation relative to that

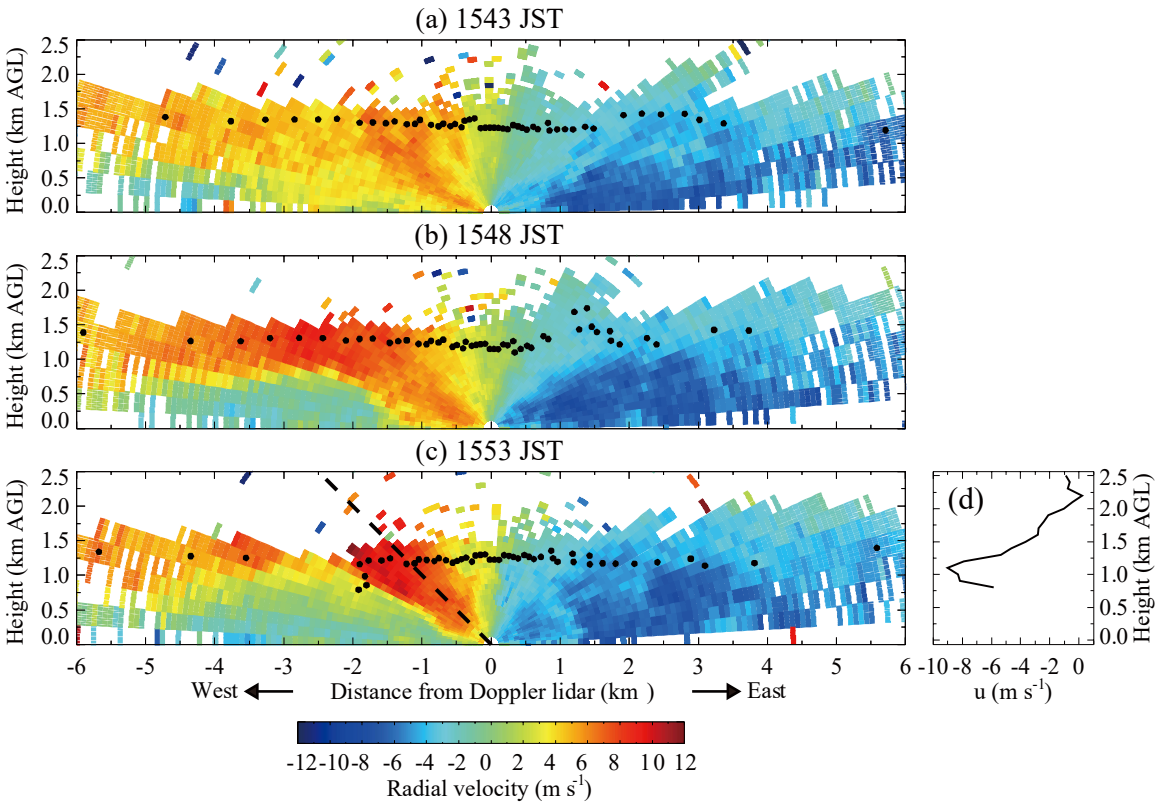

Figure 5.11. East-west vertical cross section of Doppler lidar radial velocity (color bar in m s^{-1}) at (a) 1543, (b) 1548, and (c) 1553 JST on 17 August 2012 with positive values indicating flow away from the Doppler lidar. The horizontal axis is the distance in km from the Doppler lidar with positive values pointing toward the 90° azimuth (eastward), and the vertical axis is the height in km AGL. The closed circles indicate the height of the cloud base, estimated using the empirical threshold level of the range-corrected SNR (0 dB). The dashed line in Fig. 5.11c indicates the beam direction at an elevation angle of 45°. (d) Vertical profile of zonal wind derived by WPR at 1553 JST on 17 August 2012.

before 1525 JST.

Figure 5.14 shows Doppler spectra measured in the vertical beam of the WPR. Since there is strong ground clutter below about 300 m AGL, it is difficult to estimate spectral moments accurately below about 300 m AGL. When multiple signal peaks are present at the same range in the spectral data, each first moment (i.e., Doppler velocity) is computed (Figs. 14g and 14h). From 1527 to 1530 JST (Figs. 5.14a and 5.14b), the SNR between 1.5 and 2.2 km AGL increases above the cloud base (1.4 km; Fig. 5.12) in the presence of cumulus clouds (Fig. 5.13d). This SNR enhancement may be due to strong humidity gradients at the top and edges of the cloud or to strong turbulence within the cloud (White et al. 1991; Grimsdell and Angevine 1998). This implies that an air parcel reached its LCL, which was 1.5 km AGL, derived from the ceilometer data. The LCL is also consistent with that derived from MANAL data (Section 5.3.1). Although the Doppler lidar detected the strong updraft (>3 m s-1) at and below the cloud base after 1525 JST (Fig. 5.12), the WPR did not detected it. One possible reason for the discrepancy is due to the different locations of the Doppler lidar and WPR. Since the location of the WPR was about 450 m south of the Doppler lidar (Section 5.2), the Doppler lidar and WPR observed updrafts associated with different thermals or sensed the different part of the same thermal. At 1534 JST, the enhanced SNR region extended to about 3 km AGL and there was a weak updraft below the LCL and a weak downdraft above the LCL (Fig. 5.14c). The weak downdraft suggests the existence of the entrainment of dry air aloft. A weak updraft (about 1 m s^{-1}) was present between 1.5 and 2.5 km AGL at 1535 JST (Fig. 5.14d). The updraft suddenly increased to 4.5 m s^{-1} between 2 and 2.5 km AGL at 1536 JST (Fig. 5.14e). This implies that the air parcel reached its LFC, which is estimated as 2 km AGL. The LFC is slightly higher than that derived from MANAL data (Section 5.3.1). The updraft showed a monotonic increase in Doppler velocity to peak values of 5–6 m s^{-1} from 2.2 km AGL at 1536 JST to 3.0 km AGL at 1539 JST (Fig. 5.14f). There was a downdraft of about 5 m s^{-1} at about 4 km AGL. The downdraft is probably caused by a compensating downdraft for the rising air parcel or small raindrops. The Ku-band and C-band radars detected no echo above the WPR from 1535 to 1539 JST (not shown) due to the relatively low sensitivity of the Ku-band radar and the relatively coarse temporal resolution of the C-band radar. The updraft reached a freezing level (about 5 km AGL derived from MANAL data) and the

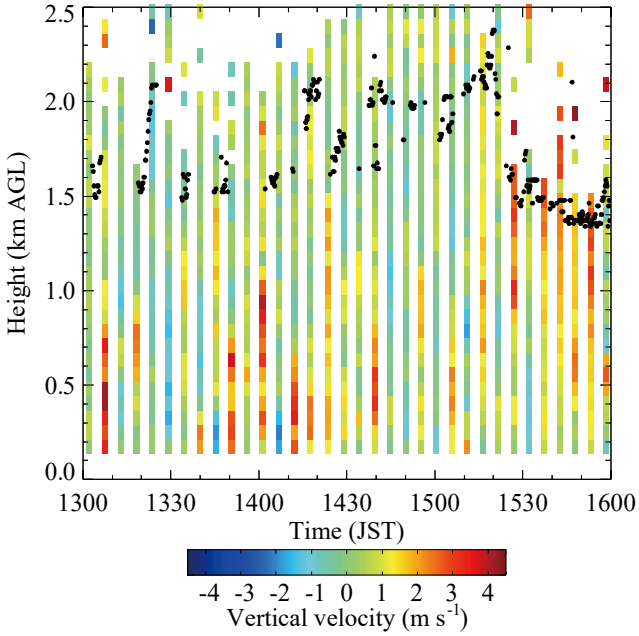

Figure 5.12. Time-height cross section of the vertical velocities observed by the Doppler lidar between 1300 and 1600 JST on 17 August 2012. Closed circles indicate the height of the cloud base derived from the ceilometer.

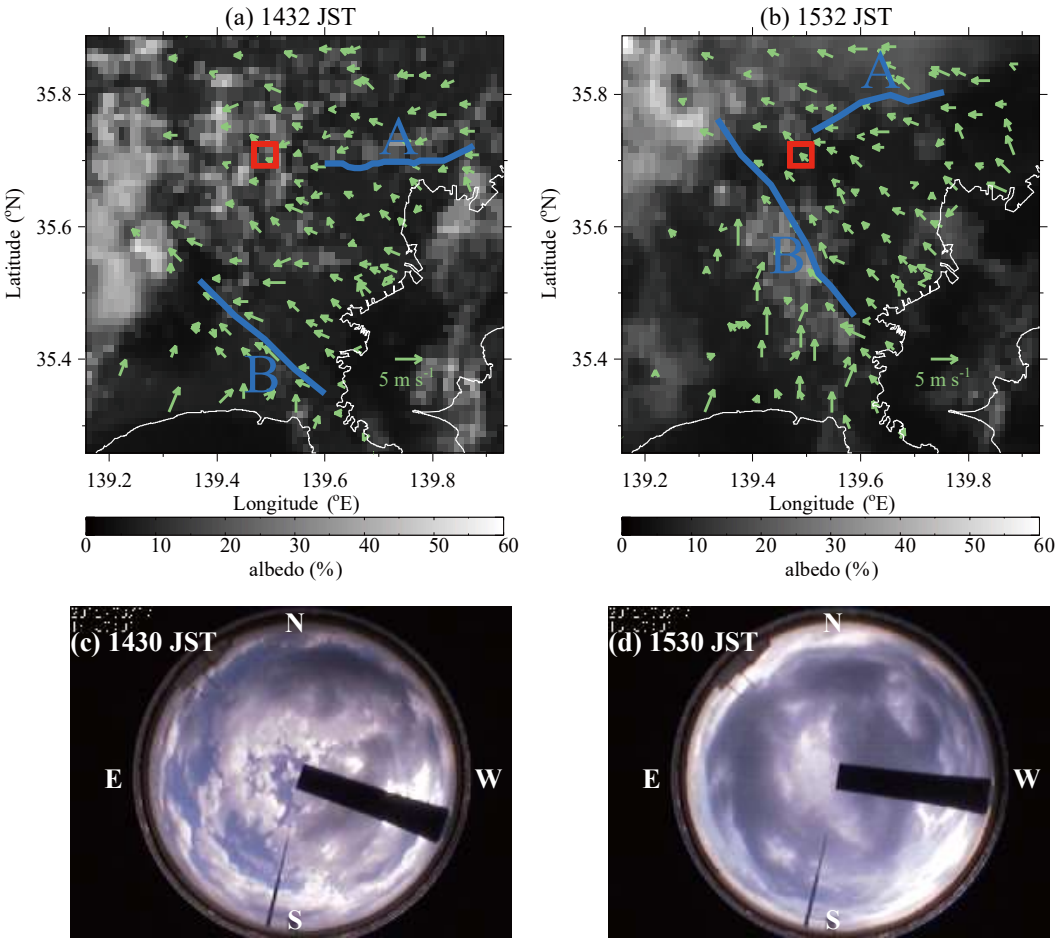

Figure 5.13. MTSAT-1R visible images at (a) 1432 and (b) 1532 JST on 17 August 2012. Surface wind fields (green arrows) observed by ambient air pollution monitoring stations at (a) 1400 and (b) 1500 JST are superimposed on the visible images. The blue lines indicate convergence lines observed by the C-band radar at (a) 1432 and (b) 1532 JST. The red open square indicates the location of the Doppler lidar (NICT headquarters). Fisheye images taken by the cloud camera from the NICT headquarters at (c) 1430 and (d) 1530 JST.

updraft–downdraft couplet was observed in the height region of 4–5 km AGL at 1541 JST (Fig. 5.14g). It is suggested that the updraft would sustain raindrops around the bottom of the freezing level. At 1543 JST, significant enhancement of the echo in the downdraft region (3.0–5.5 km AGL) occurred, resulting in strong backscattering from growing raindrops, which could not be sustained by the updraft, and snowflakes (Fig. 5.14h). The updraft above 3.5 km AGL was obscured by the strong echo from the raindrops and snowflakes. From 1541 to 1542 JST, the significant enhancement in the SNR in the height region of 2.5–4.5 km AGL was already present in only the north beam (not shown). This indicates that the precipitation echo was first observed in the north beam, and then observed one minute later in the vertical beam. This result is consistent with the fact that the first echo of hydrometeors was observed by the Ku-band radar about 1 km north-northeast of the Doppler lidar at 1541:30 JST (Fig. 5.6a).

5.5 Discussion

5.5.1 Trigger of convection initiation

The initiation of deep convection was associated with convergence line A, which formed the SBF moving inland from Tokyo Bay (Fig. 5.8). The western edge of the convergence line passed near the Doppler lidar site and the Doppler lidar also detected the same convergence (Fig. 5.9). Schreiber (1986) reported a case study in which thunderstorm initiation occurred on the extreme south end of a convergence line (Fig. 6 in Schreiber 1986). However, the location where storms will occur along a convergence line is often unknown (Wilson and Schreiber 1986). As mentioned in Section 1, several observational studies

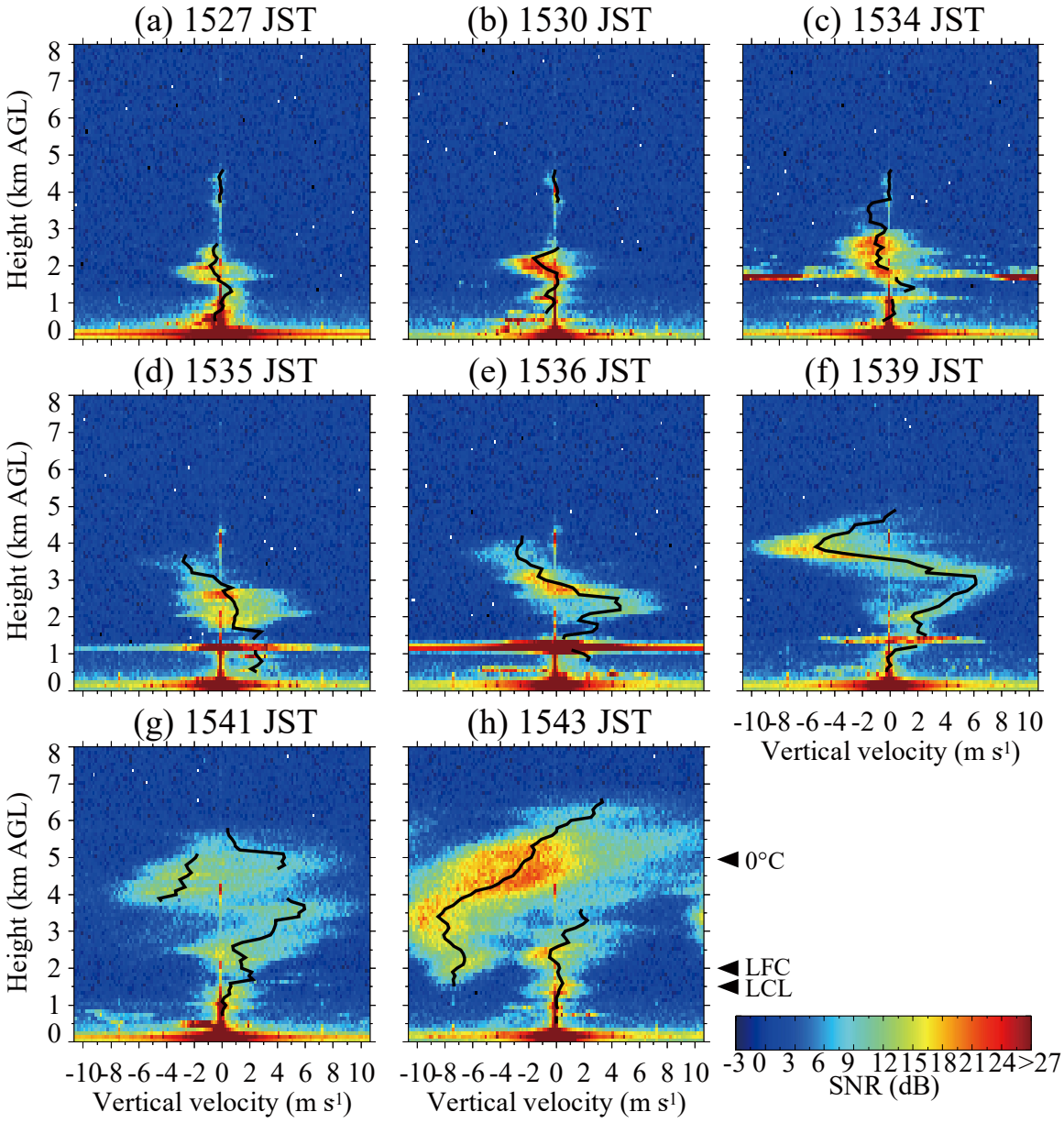

Figure 5.14. Height profiles of Doppler spectra (color bar in dB) measured in the vertical beam of the WPR and associated vertical velocity estimates (solid lines) at (a) 1527, (b) 1530, (c) 1534, (d) 1535, (e) 1536, (f) 1539, (g) 1541, and (h) 1543 JST on 17 August 2012. Colors show the SNR of the backscattered signal.

have shown that convection initiation is favored at locations where horizontal convective rolls intersect convergence lines (e.g., Wilson et al. 1992; Wakimoto and Atkins 1994; Atkins et al. 1995). However, in our observation, no horizontal convective rolls were observed by the Doppler lidar (Fig. 5.9) and other instruments. Several observational studies have shown that storms initiate near the collision regions of two boundaries (e.g., Wilson and Schreiber 1986). In our observation, the two convergence lines were observed by the C-band radar (Fig. 5.10), but they did not collide.

Between 1500 and 1600 JST, the mixing ratio increased from 15 to 16 g kg^{-1}, and the wind direction shifted from east to southeast (Fig. 5.7b) at the NICT headquarters. This indicates that the southeasterly flow transported water vapor from Tokyo Bay to the NICT headquarters (Fig. 5.4b). Note that light rain developed 2 km west of the NICT headquarters (Fig. 5.5b) an hour before the deep convection developed. The light rain was produced by cumulus clouds (Figs. 5.13a and 5.13c), which were triggered by the boundary layer thermals. Wilson and Mueller (1993) and Mueller et al. (1993) found that cumulus clouds are a good indicator of unstable atmospheric condition, since the existence of these clouds suggests that there are regions of deep moisture in the boundary layer. In this study, there is considered to have been deep boundary layer moisture present around the NICT headquarters before the convection initiation.

The strong low-level convergence and updraft at the location of convection initiation is necessary for the low-level moist air parcel to reach its LCL. The convergence at the convergence zone, which is the western edge of the convergence line (Fig. 5.9b), is about 1.5×10^{-3} s^{-1} (Section 5.4.2). Assuming an incompressible atmosphere and applying the continuity equation, the mean vertical wind speed at the LCL ($w(h)$, h = 1.5 km AGL) was calculated as

$$w(h) = w(0) - \int_0^h \left(\frac{\partial u}{\partial x} + \frac{\partial v}{\partial y} \right) dz = -\left(\frac{\partial u}{\partial x} + \frac{\partial v}{\partial y} \right) h , \tag{5.1}$$

where $w(0)$ is the vertical velocity at the surface and assumed to be 0, u and v are horizontal wind components. Thus, the mean vertical wind speed at the LCL was 2.25 m s^{-1}. This value is slightly less than, but comparable to the vertical velocity observed by the Doppler lidar below the cloud base at 1525 JST (Fig. 5.12). For the cumulus cloud formation, a rising air parcel must reach its LCL by a persistent updraft (parcel continuity principle; Ziegler and Rasmussen 1998; Ziegler et al. 2007). The time required for the near-surface air parcel to rise to its LCL is about 11 min. Since the air parcel was advected west with an easterly flow of about 4 m s^{-1} (Fig. 5.7c), the time required for the air parcel to advect from the convergence zone to the Doppler lidar/WPR was about 12 min. This means that the saturated air parcel existed over the Doppler lidar/WPR at 1529 JST. At 1530 JST, the SNR between 1.5 and 2.2 km in the vertical beam of the WPR increased above the cloud base (Fig. 5.14b). This SNR enhancement may be due to strong humidity gradients at the top and edges of clouds. It is consistent with the saturated air parcel advection. The fisheye image (Fig. 5.13d) showed that convective non-precipitating clouds were above the Doppler lidar/WPR at 1530 JST. However, the convergence line, which triggered the updraft, had already left the region of air parcel lifting (Figs. 5.8b and 5.13b). Therefore, an additional lifting mechanism is needed for the air parcel to reach its LFC. After 1525 JST, thermals with a strong updraft (>3 m s^{-1}) were vigorous at and below the cumulus cloud base (Fig. 5.12). Then the WPR directly and continuously

observed the rising air parcel above the LFC (2 km AGL) after 1536 JST (Fig. 5.14). It is suggested that the updrafts associated with the thermals was sufficient for the saturated air parcel to reach its LFC. As pointed out by Markowski et al. (2006) and Bergmaier et al. (2014), it is likely that the boundary layer thermals would play an important role in convection initiation. Since the boundary layer thermals operate on small spatial and temporal scales, the Doppler lidar and WPR are relevant tools to capture them.

It seems plausible that the weak vertical wind shear at the LCL and LFC (Figs. 5.3b and 5.7c) was a preferential factor in convection initiation. By cloud modeling study, Reuter and Yau (1987) have shown that vertical wind shear increases the entrainment of dry air into clouds, which would have reduced the rising air parcel buoyancy. Before 1536 JST, the high SNR region in the vertical beam of the WPR moved upward between 2.2 and 3.0 km (Figs. 5.14b and 5.14c). It is suggested that part of the saturated air parcel at the LCL was lifted to its LFC by the updrafts associated with thermals. The weak downdraft in the enhanced SNR above the LCL also suggests the existence of the entrainment of dry air aloft. Since the entrainment that reduces the rising air parcel buoyancy was gradually weak, it seems that the high SNR region moved upward. Then the rising air parcel did not lose its buoyancy and the sudden increase in updraft above the LFC was observed (Fig. 5.14e).

5.5.2 Interaction between SBF and preexisting cell

Convergence line B, which formed the SBF moving inland from Sagami Bay, passed through the NICT headquarters after the convection initiation (Fig. 5.10). According to the analysis of the flow at the SBF using the vertical cross section of Doppler lidar radial velocity, the strong updraft (8.29 m s^{-1}) over the nose of the SBF reached the cloud base at 1553 JST (Fig. 5.11c). At that time, precipitation cell A had already developed with a radar reflectivity of about 50 dBZ (Fig. 5.6c). Some previous studies (e.g., Wilson and Mueller 1993; Fankhauser et al. 1995; Kingsmill 1995; Wilson et al. 2001) have documented radar reflectivity intensification when convergence lines approach and pass under existing cumulus clouds. Using a WPR, May (1999) directly observed an updraft associated with a gust front, which interacted with a preexisting weak cell, and the cell intensification occurred near the WPR. However, in our case, the updraft over the nose of the SBF was associated with not the intensification of the preexisting cell but the generation of a new precipitation cell. From 1552:10 to 1600:42 JST, precipitation core of cell A descended (Figs. 5.6c and 5.6d) and the peak fall speed of the rain observed by the WPR reached 10 m s^{-1} below 5 km AGL (not shown). Cell A was not intensified after the SBF passage. It is suggested that the updraft over the nose of the SBF did not overcome the downdraft with heavy rainfall. By contrast, a new precipitation cell B was generated in a relatively weak echo (30 to 35 dBZ) region of cell A. This suggests that there was a preferential region of convection initiation. Note that cell B in Fig. 5.6e appears to be an embryo of cell A and is similar to a “new misoscale convective echo” (NMCE) reported by Sakurai et al. (2012) using a Ka-band Doppler radar. However, the initiation mechanism of the NMCE has not been clarified. As pointed out by Sakurai et al., a further series of case studies is needed.

5.6 Summary

In this study, we described the dynamics leading to convection initiation associated with an isolated convective storm using observations collected in the southern Kanto Plain on 17 August 2012. Several surface sensors and ground-based remote sensing instruments were operated simultaneously and captured the life cycle of the isolated convective storm. The observation results are summarized in the schematic illustration presented in Fig. 5.15.

Before the convection initiation, a southeasterly flow transported water vapor from Tokyo Bay to the NICT headquarters, and a well-mixed and cumulus-cloud-topped convective boundary layer developed (Fig. 5.15a). Although the CAPE was high, the CIN was moderate and the LCL and LFC were large. In such circumstances, one might expect that a strong trigger would be necessary for convection initiation over a flat terrain.

When the convergence line in the form of an SBF moving inland from Tokyo Bay approached near the NICT headquarters, the near-surface air parcel was lifted to its LCL (1.5 km AGL) by the updraft at the western edge of the convergence line (Fig. 5.15b). The saturated air parcel at the LCL was lifted to its LFC (2 km AGL) by the updrafts associated with thermals at and below the cumulus cloud base. It is possible that the weak vertical wind shear and entrainment at the LCL and LFC did not inhibit convective growth. The air parcel ascended with a peak updraft of 5–6 m s^{-1}. About 6 min after the air parcel reached to its LFC, the first echo of hydrometeors was

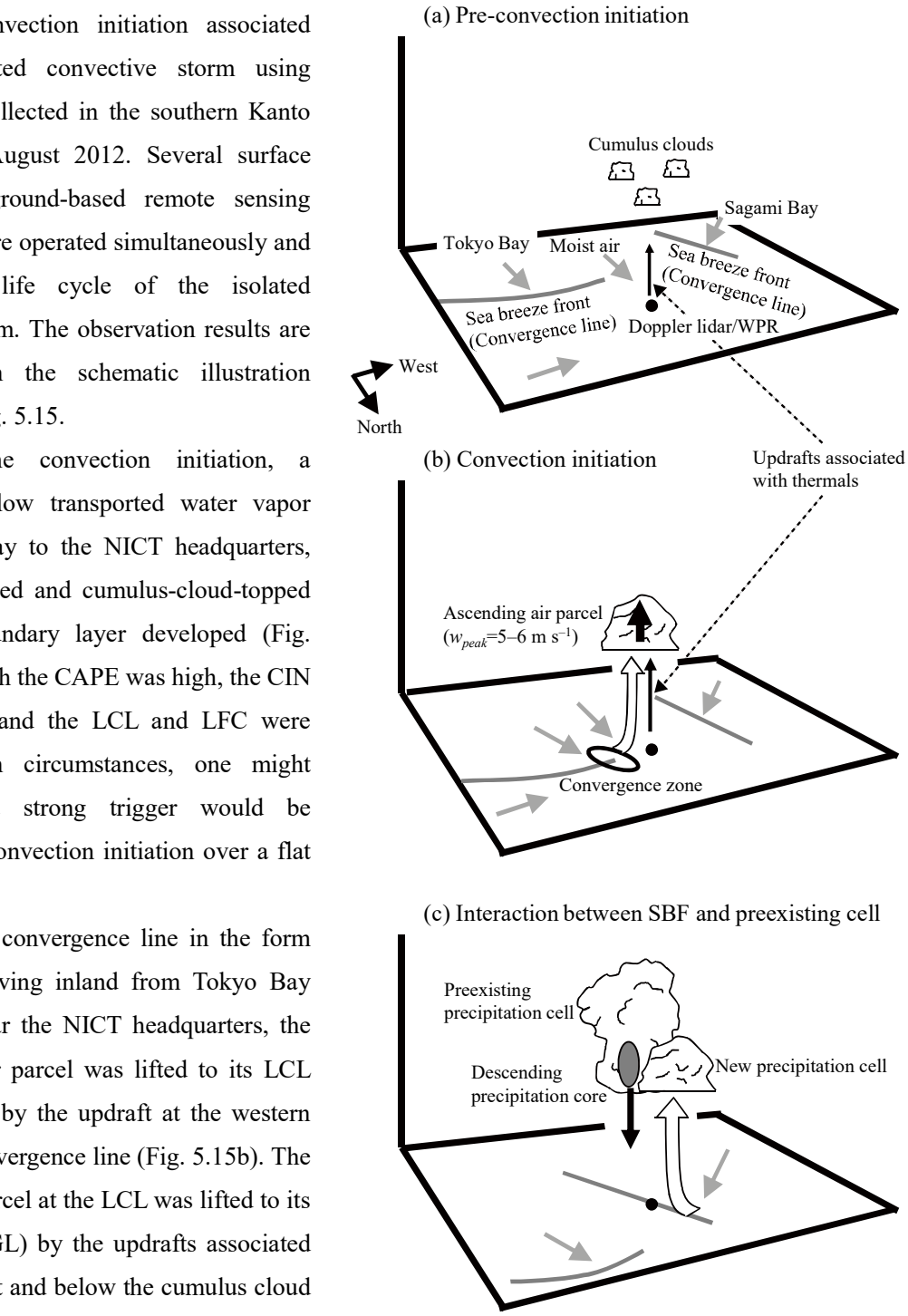

Figure 5.15. Schematic illustration of observation results (a) before the convection initiation, (b) during the convection initiation, and (c) at the interaction between the SBF and the preexisting cell.

detected by the Ku-band radar and WPR. The precipitation cell grew rapidly and the radar reflectivity of the precipitation core reached 50 dBZ about 10 min after the first echo.

When the precipitation core descended, the SBF moving inland from Sagami Bay passed under the preexisting precipitation cell (Fig. 5.15c). Although the updraft over the nose of the SBF was strong, the preexisting precipitation cell was not intensified after the SBF passage owing to the downdraft with heavy rainfall. The updraft triggered a new precipitation cell, which was generated in a relatively weak echo region of the preexisting precipitation cell.

The combined use of different remote sensing instruments was helpful for investigating convection initiation, because each instrument has its advantages and limitations. The Ku-band radar provided the precise location of the convection initiation with high temporal and spatial resolution. The C-band radar observed the entire structure, location, and movement of convergence lines in a wide range. The Doppler lidar observed the detailed kinematic structure of the convergence line, such as the convergence and updraft, although its observation area was narrow. The Doppler lidar could observe the vertical velocity below clouds but not that in optically thick clouds. By contrast, the WPR captured the vertical motion of the air parcel below and in the clouds associated with convection initiation. In particular, the high temporal and spatial observations of the subcloud and in-cloud vertical air motion by the Doppler lidar and WPR revealed updraft and downdraft structure associated with the convection initiation.

6. CONCLUDING REMARKS

This thesis is devoted to an observational study on mesoscale phenomena associated with sea breezes from the viewpoint of winds based on coherent Doppler lidar (CDL) observations. On the basis of the three case studies presented in this thesis, we could clarify the dynamic structures of mesoscale phenomena: the three-dimensional structure of convection in the convective internal boundary layer (CIBL) formed in the sea-breeze layer (Chapter 3), the formation of the updraft at the sea-breeze front (SBF) (Chapters 4 and 5), the effect of the SBF on the vertical transport of a near-surface dense aerosol (Chapter 4), and the effect of the SBF on the convection initiation of an isolated convective storm (Chapter 5). The observational results obtained by the CDLs along with other meteorological instruments provide new insights into the vertical turbulent transport of momentum and heat within the CIBL and the vertical transport of aerosols and water vapor at the SBF.

The first case study illustrated that the three-dimensional structure of several-hundred-meter-scale horizontal convective rolls (HCRs) and near-surface streaks in the slightly unstable CIBL formed in the sea-breeze layer. The dual-Doppler lidar observation at Sendai Airport was conducted for the first time in Japan. The dynamic structure of convection in the CIBL was clarified from the results of dual-Doppler lidar analysis. There were streaky structures of the streamwise velocity and vertical velocity fluctuations and convergence-divergence patterns of cross-stream velocity fluctuations that were elongated in the streamwise direction near the surface. The region of upward flow in the HCRs originated in near-surface low-speed streaks. The relationship between the HCRs and the streaks is consistent with the results of the previous LES studies. The aspect ratio of HCRs was 2.05–2.50, which is close to the value predicted by linear theories. The difference between the wavelengths of the HCRs and streaks to the north and south of Sendai Airport can be explained in terms of the different surface-heating conditions and surface roughnesses. It has recently been confirmed by numerical simulation studies using an advanced mesoscale weather forecasting system with a super-high resolution (Chen et al. 2015a; 2015b). The CDLs also performed intersecting RHI scans to vertical profiles of horizontal wind vectors in the intersecting vertical lines. The spatial variations of vertical wind profiles in the sea-breeze layer at the near-shore coastal area could be measured by this technique. The CIBL height estimated from vertical wind profiles was roughly proportional to the square root of the downwind distance from the shore.

In the second case study, the formation of a strong updraft at an SBF and the associated vertical transport of a near-surface dense aerosol, which occurred in the Tokyo metropolitan area, are discussed. Over the nose of the SBF, a strong updraft of approximately 5 m s^{-1} was formed with a horizontal scale of about 500 m and a vertical scale of 2 km. The updraft reached the mixing height. The spatial relationship between the updraft and the prefrontal thermal suggests that the strong updraft was triggered by the interaction between the SBF and the thermal. Immediately after the updraft formation, the vertical extent of an intense aerosol backscatter up to the mixing height was observed by the ceilometer. The observational results suggest that the near-surface denser aerosols trapped in the head region of the SBF

escaped from the nose of the SBF and were then vertically transported up to the mixing height by the strong updraft at the SBF. This implies that these phenomena occurred not continuously but intermittently.

In the third case study, the dynamics leading to a convection initiation associated with an isolated convective storm that occurred in the Tokyo metropolitan area is clarified. The convection initiation was triggered by an SBF moving inland from Tokyo Bay. A 3-km-scale convergence zone formed at the west edge of the convergence line in the form of the SBF. The near-surface air parcel was lifted to its lifting condensation level (LCL) by the updraft in the convergence zone. The saturated air parcel at the LCL was lifted to its level of free convection (LFC) by the thermal updraft at and below the cumulus cloud base. After the air parcel reached its LFC, the convective cell developed rapidly. When the SBF arriving from Sagami Bay passed under the cell, the updraft over the nose of the SBF triggered a new precipitation cell generated in a relatively weak echo region of the preexisting cell. However, the preexisting cell was not intensified by the updraft.

The third case study shows that the synergetic use of different remote sensing instruments including CDLs is important to observe severe mesoscale phenomena involved in precipitation. To increase the warning lead time of the severe mesoscale phenomena such as localized heavy rainfalls and tornadoes, early detection of the phenomena will require monitoring disturbances in the optically clear boundary layer such as convergence lines. From the viewpoint of disaster prevention and mitigation, CDLs have potential applications for the early detection of clear-air phenomena that trigger convection initiation. To understand the mechanisms leading to the convection initiation of severe mesoscale phenomena and the relationship between the convection initiation and the subsequent occurrence of severe mesoscale phenomena, the synergetic use of CDLs and radars is essential. From the viewpoint of the early prediction of the severe mesoscale phenomena, it is also important to assimilate the CDL data into state-of-the-art numerical weather prediction systems. It has recently been confirmed that assimilating CDL data into a nonhydrostatic four-dimensional variational data assimilation system significantly improved the reproduction of an isolated mesoscale convective system (Kawabata et al. 2014). A study on real time assimilation of CDL data is also being conducted.

References

Abbs, D. J., and W. J. Physick, 1992: Sea-breeze observation and modeling: A review. *Aust. Meteor. Mag.*, **41**, 7–19.

Atkinson, B. W., and J. W. Zhang, 1996: Mesoscale shallow convection in the atmosphere. *Rev. Geophys.*, **34**, 403–431.

Atkins, N. T., and R. M. Wakimoto, 1997: Influence of the synoptic-scale flow on sea breezes observed during CaPE. *Mon. Wea. Rev.*, **125**, 2112–2130.

Atkins, N. T., R. M. Wakimoto, and T. M. Weckwerth, 1995: Observations of the sea-breeze front during CaPE. Part II: Dual-Doppler and aircraft analysis. *Mon. Wea. Rev.*, **123**, 944–969.

Atlas, D., 1960: Radar detection of the sea breeze. *J. Meteor.*, **17**, 244–258.

Balanchard, D. O., and R. E. López, 1985: Spatial patterns of convection in south Florida. *Mon. Wea. Rev.*, **113**, 1282–1299.

Baker, R. D., B. H. Lynn, A. Boone, W.-K. Tao, and J. Simpson, 2001: The influence of soil moisture, coastline curvature, and land-breeze circulations on sea-breeze-initiated precipitation. *J. Hydrometeor.*, **2**, 193–211

Baker, W. E., G. D. Emmitt, F. Robertson, R. M. Atlas, J. E. Molinari, D. A. Bowdle, J. Paegle, R. M. Hardesty, R. T. Menzies, T. N. Krishnamurti, R. A. Brown, M. J. Post, J.R. Anderson, A. C. Lorenc, and J. McElroy, 1995: Lidar-measured winds from space: An essential component for weather and climate prediction. *Bull. Amer. Meteor. Soc.*, **76**, 869–888.

Banta, R. M., L. D. Oliver, and D. H. Levinson, 1993: Evolution of the Monterey Bay sea-breeze layer as observed by pulsed Doppler lidar. *J. Atmos. Sci.*, **50**, 3959–3982.

Banta, R. M., 1995: Sea breezes shallow and deep on the California coast. *Mon. Wea. Rev.*, **123**, 3614–3622.

Banta, R. M., C. J. Senff, J. Nielsen-Gammon, L. S. Darby, T. B. Ryerson, R. J. Alvarez, S. P. Sandberg, E. J. Williams, and M. Trainer, 2005: A bad air day in Houston. *Bull. Amer. Meteor. Soc.*, **86**, 657–669.

Bastin, S., P. Drobinski, A. M. Dabas, P. Delville, O. Reitebuch, and C. Werner, 2005: Impact of the Rhône and Durance valleys on sea breeze circulation in the Marseille area. *Atmos. Res.*, **74**, 303–328.

Bastin, S., P. Drobinski, V. Guénard, J.-L. Caccia, B. Campistron, A. M. Dabas, P. Delville, O. Reitebuch, and C. Werner, 2006: On the interaction between sea breeze and summer mistral at the exit of the Rhône valley. *Mon. Wea. Rev.*, **134**, 1647–1668.

Behrendt, A., S. Pal, F. Aoshima, M. Bender, A. Blyth, U. Corsmeier, J. Cuesta, G. Dick, M. Dorninger, C. Flamant, P. D. Girolamo, T. Gorgas, Y. Huang, N. Kalthoff, S. Khodayar, H. Mannstein, K. Träumner, A. Wieser, and V. Wulfmeyer, 2011: Observation of convection initiation processes with a suite of state-of-the-art research instruments during COPS IOP 8b. *Quart. J. Roy. Meteor. Soc.*, **137**, 81–100.

Bennett, L. J., K. A. Brown, A. M. Blyth, D. J. Parker, and P. A. Clark, 2006: A review of the initiation of precipitating convection in the United Kingdom. *Quart. J. Roy. Meteor. Soc.*, **132**, 1001–1020.

Bergmaier, P. T., B. Geerts, Z. Wang, B. Liu, and P. C. Campbell, 2014: A dryline in southeast Wyoming. Part II: Airborne in situ and Raman lidar observations. *Mon. Wea. Rev.*, **142**, 2961–2977.

Berry, R. E., and L. R. Taylor, 1968: High-altitude migration of aphids in maritime and continental climates. *J. Anim. Ecol.*, **37**, 713–722.

Bilbro, J. W., and W. W. Vaughan, 1978: Wind field measurement in the nonprecipitous regions surrounding severe storms by an airborne pulsed Doppler lidar system. *Bull. Amer. Meteor. Soc.*, **59**, 1095–1100.

Bilbro, J. W., G. Fichtl, D. Fitzjarrald, M. Krause, and R. Lee, 1984: Airborne Doppler lidar wind field measurements. *Bull. Amer. Meteor. Soc.*, **65**, 348–359.

Boyouk, N., J.-F. Léon, H. Delbarre, P. Augustin, and M. Fourmentin, 2011: Impact of sea breeze on vertical structure of aerosol optical properties in Dunkerque, France. *Atmos. Res.*, **101**, 902–910.

Brown, R. A., 1980: Longitudinal instabilities and secondary flows in the planetary boundary layer: A review. *Rev. Geophys. Space Phys.*, **18**, 683–697.

Browning, R. A., and R. Wexler, 1968: The determination of kinematic properties of a wind field using Doppler radar. *J. Appl. Meteor.*, **7**, 105–113.

Browning, K. A., C. J. Morcrette, J. Nicol, A. M. Blyth, L. J. Bennett, B. J. Brooks, J. Marsham, S. D. Mobbs, D. J. Parker, F. Perry, P. A. Clark, S. P. Ballard, M. A. Dixon, R. M. Forbes, H. W. Lean, Z. Li, N. M. Roberts, U. Corsmeier, C. Barthlott, B. Deny, N. Kalthoff, S. Khodayar, M. Kohler, C. Kottmeier, S. Kraut, M. Kunz, J. Lenfant, A. Wieser, J. L. Agnew, D. Bamber, J. McGregor, K. M. Beswick, M. D. Gray, E. Norton, H. M. A. Ricketts, A. Russell, G. Vaughan, A. R. Webb, M. Bitter, T. Feuerle, R. Hankers, H. Schulz, K. E. Bozier, C. G. Collier, F. Davies, C. Gaffard, T. J. Hewison, D. N. Ladd, E. C. Slack, J. Waight, M. Ramatschi, D. P. Wareing, and R. J. Watson, 2007: The Convective Storm Initiation Project. *Bull. Amer. Meteor. Soc.*, **88**, 1939–1955.

Burpee, R. W., and L. N. Lahiff, 1984: Area-average rainfall variations on sea-breeze days in south Florida. *Mon. Wea. Rev.*, **112**, 520–534.

Byers, H. R., and H. R. Rodebush, 1948: Causes of thunderstorms of the Florida Peninsula. *J. Meteor.*, **5**, 275–280.

Carrol, J. J., 1989: Analysis of airborne Doppler lidar measurements of the extended California sea breeze. *J. Atmos. Oceanic Technol.*, **6**, 820–831.

Chan, P. W., and Y. F. Lee, 2012: Application of short-range lidar in wind shear alerting. *J. Atmos. Oceanic Technol.*, **29**, 207–220.

Chen, G., X. Zhu, W. Sha, T. Iwasaki, H. Seko, K. Saito, H. Iwai, and S. Ishii, 2015a: Toward improved forecast of sea-breeze horizontal convective rolls at super high resolution. Part I: configuration and verification of a Down-Scaling Simulation System (DS^3). *Mon. Wea. Rev.*, **143**, 1849–1872.

Chen, G., X. Zhu, W. Sha, T. Iwasaki, H. Seko, K. Saito, H. Iwai, and S. Ishii, 2015b: Toward improved forecast of sea-breeze horizontal convective rolls at super high resolution. Part II: The impacts of

land use and buildings. *Mon. Wea. Rev.*, **143**, 1873–1894.

Chiba, O., 1993: The turbulent characteristics in the lowest port of the sea breeze front in the atmospheric surface layer. *Bound.-Layer Meteor.*, **65**, 181–195.

Chiba, O., 1997: Variability of the sea-breeze front from sodar measurements. *Bound.-Layer Meteor.*, **82**, 165–174.

Chuda, T., and H. Niino, 2005: Climatology of environmental parameters for mesoscale convections in Japan. *J. Meteor. Soc. Japan*, **83**, 391–408.

Cressman, G. P., 1959: An operational objective analysis system. *Mon. Wea. Rev.*, **87**, 367–374.

Cros, B., P. Durand, H. Cachier, P. Drobinski, E. Fréjafon, C. Kottmeïer, P. E. Perros, V. H. Peuch, J. L. Ponche, D. Robin, F. Saïd, G. Toupance, and H. Wortham, 2004: The ESCOMPTE program: An overview. *Atmos. Res.*, **69**, 241–279.

Crosman, E., and J. Horel, 2010: Sea and lake breezes: A review of numerical studies. *Bound.-Layer Meteor.*, **137**, 1–29.

Darby, L. S., 2005: Cluster analysis of surface winds in Houston, Texas, and the impact of wind patterns on ozone. *J. Appl. Meteor.*, **44**, 1788–1806.

Darby, L. S., R. M. Banta, W. A. Brewer, W. D. Neff, R. D. Marchbanks, B. J. McCarty, C. J. Senff, A. B. White, W. M. Angevine, and E. J. Williams, 2002: Vertical variations in O_3 concentrations before and after a gust front passage. *J. Geophys. Res.*, **107**, D13, 4176.

Deardorff, J. W., G. E. Willis, and D. K. Lilly, 1969: Laboratory investigation of non-steady penetrative convection. *J. Fluid Mech.*, **35**, 7–31.

Demoz, B., C. Flamant, T. Weckwerth, D. Whiteman, K. Evans, F. Fabry, P. D. Girolamo, D. Miller, B. Geerts, W. Brown, G. Schwemmer, B. Gentry, W. Felts, and Z. Wang, 2006: The dryline on 22 May 2002 during IHOP_2002: Convective-scale measurements at the profiling site. *Mon. Wea. Rev.*, **134**, 294–310.

De Wekker, S. F. J., K. S. Godwin, G. D. Emmitt, and S. Greco, 2012: Airborne Doppler lidar measurements of valley flows in complex coastal terrain. *J. Appl. Meteor. Climatol.*, **51**, 1558–1574.

Doviak, R. J., and M. Berger, 1980: Turbulence and waves in the optically clear planetary boundary layer resolved by dual-Doppler radars. *Radio Sci.*, **15**, 297–317.

Drobinski, P., P. Carlotti, R. Newsom, R. Banta, R. Foster, and J. Redelsperger, 2004: The structure of the near-neutral atmospheric surface layer. *J. Atmos. Sci,*, **61**, 699–714.

Drobinski, P., S. Bastin, A. Dabas, P. Delville, and O. Reitebuch, 2006: Variability of three-dimensional sea breeze structure in southern France: observations and evaluation of empirical scaling laws. *Ann. Geophys,*, **24**, 1783–1799.

Drobinski, P., P. Carlotti, J. Redelsperger, R. Banta, V. Masson, and R. Newsom, 2007: Numerical and experimental investigation of the neutral atmospheric surface layer. *J. Atmos. Sci.*, **64**, 137–156.

Druilhet, A., A. Herrada, J. P. Pages, J. Saïssac, C. Allet, and M. Ravaut, 1982: Étude expérimentale de la couche limite interne associée à la brise de mer. *Bound.-Layer Meteor.*, **22**, 511–524.

Eastwood, E., and G. C. Rider, 1961: A radar observation of a sea-breeze front. *Nature*, **189**, 978–-980.

Emeis, S., C. Münkel, S. Vogt, W. J. Muller, and K. Schafer, 2004: Atmospheric boundary-layer structure from simultaneous SODAR, RASS, and ceilometer measurements. *Atmos. Environ.*, **38**, 273–286.

Estoque, M. A., 1962: The sea breeze as a function of the prevailing synoptic situation. *J. Atmos. Sci.*, **19**, 244–250.

Etling, D., and R. A. Brown, 1993: A review of large-eddy dynamics in the planetary boundary layer. *Bound.-Layer Meteor.*, **65**, 215–248.

Eymard, L., and A. Weill, 1984: Dual Doppler radar investigation of the tropical convective boundary layer. *J. Atmos. Sci.*, **45**, 853–864.

Fankhause, J. C., N. A. Crook, J. Tuttle, L. J. Miller, and C. G. Wade, 1995: Initiation of deep convection along boundary layer convergence lines in a semitropical environment. *Mon. Wea. Rev.*, **123**, 291–313.

Finkele, K., J. M. Hacker, H. Kraus, and R. A. D. Byron-Scott, 1995: A complete sea-breeze circulation cell derived from aircraft observations. *Bound.-Layer Meteor.*, **73**, 299–317.

Fitzgerald, J. W., 1989: Model of the aerosol extinction profile in a well-mixed marine boundary layer. *Appl. Opt.*, **28**, 3534–3538.

Frank, N. L., P. L. Moore, and G. E. Fisher, 1967: Summer shower distribution over the Florida Peninsula as deduced from digitized radar data. *J. Appl. Meteor.*, **6**, 309–316.

Frehlich, R., 1995: Comparison of 2- and 10-μm coherent Doppler lidar performance. *J. Atmos. Oceanic Technol.*, **14**, 415–420.

Frehlich, R., S. M. Hannon, and S. W. Henderson, 1997: Coherent Doppler lidar measurements of winds in the weak signal regime. *Appl. Opt.*, **36**, 3491–3499.

Fujibe, F., and T. Asai, 1979: A study of local winds in the Kanto district. Part 1: Structures of wind systems with diurnal variation. *Tenki*, **26**, 595–604 (in Japanese).

Fujibe, F., and T. Asai, 1984: A detailed analysis of the land and sea breeze in the Sagami Bay area in summer. *J. Meteor. Soc. Japan*, **62**, 534–551.

Fujibe, F., K. Sakagami, K. Chubachi, and K. Yamashita, 2002: Surface wind patterns preceding short-time heavy rainfall in Tokyo in the afternoon on midsummer days. *Tenki*, **49**, 395–405 (in Japanese).

Fujiwara, C., K. Yamashita, and Y. Fujiyoshi, 2010: Dust devil-like vortices along sea-breeze fronts detected by a 3-D scanning Doppler lidar. *Proc. 28th Laser Sensing Simp.*, 150–153.

Fujiwara, C., K. Yamashita, and Y. Fujiyoshi, 2012: Observed effect of mesoscale vertical vorticity on rotation sense of dust devil-like vortices in an urban area. *SOLA*, **8**, 25–28.

Gal-Chen, T., 1982: Errors in fixed and moving frame of references: Applications for conventional and Doppler radar analysis. *J. Atmos. Sci.*, **39**, 2279–2300.

Gamo, M., S. Yamamoto, and O. Yokoyama, 1982: Airborne measurements of the free convective internal boundary layer during the sea breeze. *J. Meteor. Soc. Japan*, **60**, 1284–1298.

Gao, J., M. Xue, A. Shapiro, and K. K. Droegemeier, 1999: A variational method for the analysis of three-dimensional wind fields from two Doppler radars. *Mon. Wea. Rev.*, **127**, 2128–2142.

Gentry, R. C., and P. L. Moore, 1954: Relation of local and general wind interaction near the sea coast to time and location of air-mass showers. *J. Meteor.*, **11**, 507–511.

Geotis, S. G., 1964: On sea breeze 'angels'. *Proc. World Conf. on Radio Meteor.*, Boston, Mass., Amer. Meteor. Soc., 6–9.

Gibert, F., J. Cuesta, J. Yano, N. Arnault, and P. H. Flamant, 2007: On the correlation between convective plume updrafts and downdrafts, lidar reflectivity and depolarization ratio. *Bound.-Layer Meteor.*, **125**, 553–573.

Grimsdell, A. W., and W. M. Angevine, 1998: Convective boundary layer height measurement with wind profilers and comparison to cloud base. *J. Atmos. Oceanic Technol.*, **15**, 1331–1338.

Grund, C. D., R. M. Banta, J. L. George, J. N. Howell, M. J. Post, R. A. Richter, and A. M. Weickmann, 2001: High-resolution Doppler lidar for boundary layer and cloud research. *J. Atmos. Oceanic Technol.*, **18**, 376–393.

Hadi, T. W., T. Horinouchi, T. Tsuda, H. Hashiguchi, and S. Fukao, 2002: Sea-breeze circulation over Jakarta, Indonesia: A climatology based on boundary layer radar observations. *Mon. Wea. Rev.*, **130**, 2153–2166.

Helmis, C. G., D. N. Asimakopoulos, D. G. Deligiorgi, and D. P. Lalas, 1987: Observations of sea-breeze fronts near the shoreline. *Bound.-Layer Meteor.*, **38**, 395–410.

Henderson, S. W., C. P. Hale, J. R. Magee, M. J. Kavaya, and A. V. Huffaker, 1991: Eye-safe coherent laser radar system at 2.1 μm using Tm,Ho:YAG lasers. *Opt. Lett.*, **16**, 773–775.

Henderson, S. W., P. J. M. Suni, C. P. Hale, S. M. Hannon, J. R. Magee, D. L. Bruns, and E. H. Yuen, 1993: Coherent laser radar at 2 μm using solid-state lasers. *IEEE Trans. Geosci. Remote Sens.*, **31**, 4–15.

Henderson, S., P. Gatt, D. Rees, and R. M. Huffaker, 2005: Wind Lidar, *Laser Remote Sensing*, T. Fujii and T. Fukuchi, Eds., CRC Press, 469–722.

Hinrichsen, D., 1998: *Coastal Waters of the World: Trends, Threats, and Strategies*, Island Press, Washington D.C., 275 pp.

Hinrichsen, D., 1999: The coastal population explosion, *Trends and Future Challenges for U.S. National Ocean and Coastal Policy*, Cicin-Sain B., R. W. Knecht, and N. Foster, Eds., National Oceanic and Atmospheric Administration, 27–29.

Hirano, K., and M. Maki, 2010: Method of VIL calculation for X-band polarimetric radar and potential of VIL for nowcasting of localized severe rainfall –Case study of the Zoshigaya downpour, 5 August 2008–. *SOLA*, **6**, 89–92.

Horie, H., and K. Tomine, 1998: A study on generation and movement of air mass thunderstorms over Kanto area in summer 1995. *Tenki*, **45**, 441–453 (in Japanese).

Huffaker, R. M., T. R. Lawrence, M. J. Post, J. T. Priestley, F. F. Hall, Jr., R. A. Richter, and R. J. Keeler, 1984: Feasibility studies for a global wind measuring satellite system (Windsat): Analysis of simulated performance. *Appl. Opt.*, **23**, 2523–2536.

Imai, K., T. Nakagawa, and H. Hashiguchi, 2007: Development of tropospheric wind profiler radar with Luneberg lens antenna. *SEI Technical Review*, **64**, 38–42.

Intrieri, J. M., A. J. Bedard, and R. M. Hardesty, 1990: Details of colliding thunderstorm outflows as observed by Doppler lidar. *J. Atmos. Sci.*, **47**, 1081–1099.

Ishihara, M., 2012a: Radar echo population of thunderstorms generated on the 2008 Zoshigaya-rainstorm day and nowcasting of thunderstorm-induced local heavy rainfalls. Part I: Three-dimensional radar echo population of the thunderstorms. *Tenki*, **59**, 549–561 (in Japanese).

Ishihara, M., 2012b: Radar echo population of thunderstorms generated on the 2008 Zoshigaya-rainstorm day and nowcasting of thunderstorm-induced local heavy rainfalls. Part II: A feasibility study on nowcasting of thunderstorm-induced local heavy rainfalls. *Tenki*, **59**, 563–577 (in Japanese).

Ishii, S., K. Mizutani, T. Aoki, M. Sasano, Y. Murayama, T. Itabe, and K. Asai, 2005: Wind profiling with an eye-safe coherent Doppler lidar system: comparison with radiosondes and VHF radar. *J. Meteor. Soc. Japan*, **83**, 1041–1056.

Ishii, S., K. Mizutani, T. Itabe, T. Aoki, Y. Ohno, H. Horie, T. Shimabukuro, A. Sato, and K. Asai, 2006: Development of 2-μm airborne coherent Doppler lidar at NICT. *Proc. SPIE*, **6409**, 6409J-1–6409J -8, Goa, India.

Ishii, S., K. Sasaki, K. Mizutani, T. Aoki, T. Itabe, H. Kannno, D. Matsushima, W. Sha, A. Noda, M. Sawada, M. Ujiie, Y. Matsuura, and T. Iwasaki, 2007: Temporal evolution and spatial structure of the local easterly wind "Kiyokawa-dashi" in Japan PART I: Coherent Doppler lidar observations. *J. Meteor. Soc. Japan*, **85**, 797–813.

Ishii, S., K. Mizutani, H. Fukuoka, T. Ishikawa, B. Philippe, H. Iwai, T. Aoki, T. Itabe, A. Sato, and K. Asai, 2010: Coherent 2 μm differential absorption and wind lidar with conductively cooled laser and two-axis scanning device. *Appl. Opt.*, **49**, 1809–1817.

Itabe, T., K. Mizuitani, M. Ishizu, and K. Asai, 2001: ISS/JEM-borne coherent Doppler lidar program to measure the wind from space. *Proc. Society of Photo-Optical Instrumentation Engineering*, **4153**, 412–419.

Iwai, H., S. Ishii, N. Tsunematsu, K. Mizutani, Y. Murayama, T. Itabe, I. Yamada, N. Matayoshi, D. Matsushima, W. Sha, T. Yamazaki, and T. Iwasaki, 2008: Dual-Doppler lidar observation of horizontal convective rolls and near-surface streaks. *Geophys. Res. Lett.*, **35**, L14808.

Iwai, H., Y. Murayama, S. Ishii, K. Mizutani, Y. Ohno, and T. Hashiguchi, 2011: Strong updraft at a sea-breeze front and associated vertical transport of near-surface dense aerosol observed by Doppler lidar and ceilometer. *Bound.-Layer Meteor.*, **141**, 117–142.

Iwai, H., S. Ishii, R. Oda, K. Mizutani, S. Sekizawa, and Y. Murayama, 2013: Performance and technique of coherent 2-μm differential absorption and wind lidar for wind measurement. *J. Atmos. Oceanic Technol.*, **30**, 429–449.

Kai, K., K. Ura, T. Kawamura, and H. Ono, 1995: A case study on the Kanpachi Street cloud. *Tenki*, **42**, 417–427 (in Japanese).

Kanda, M., Y. Inoue, and I. Uno, 2001: Numerical study on cloud lines over an urban street in Tokyo. *Bound.-Layer Meteor.*, **98**, 251–273.

Karan, H., and K. Knupp, 2006: Mobile Integrated Profiler System (MIPS) observations of low-level

convergent boundaries during IHOP. *Mon. Wea. Rev.*, **134**, 92–112.

Kato, A., and M. Maki, 2009: Localized heavy rainfall near Zoshigaya, Tokyo, Japan on 5 August 2008 observed by X-band polarimetric radar –preliminary analysis–. *SOLA*, **5**, 89–92.

Kawabata, T., T. Kuroda, H. Seko, and K. Saito, 2011: A cloud-resolving 4DVAR assimilation experiment for a local heavy rainfall event in the Tokyo metropolitan area. *Mon. Wea. Rev.*, **139**, 1911–1931.

Kawabata, T., H. Iwai, H. Seko, Y. Shoji, K. Saito, S. Ishii, and K. Mizutani, 2014: Cloud-resolving 4D-Var assimilation of Doppler wind lidar data on a meso-gamma scale convective system. *Mon. Wea. Rev.*, **142**, 4484–4498.

Khanna, S., and J. G. Brasseur, 1998: Three-dimensional buoyancy- and shear-induced local structure of the atmospheric boundary layer. *J. Atmos. Sci.*, **55**, 710–743.

Kim, S. W., and S. U. Park, 2003: Coherent structures near the surface in a strongly sheared convective boundary layer generated by large-eddy simulation. *Bound.-Layer Meteor.*, **106**, 35–60.

Kim, D.-S., M. Maki, S. Shimizu, and D.-I. Lee, 2012: X-band dual-polarization radar observations of precipitation core development and structure in a multi-cellular storm over Zoshigaya, Japan, on August 5, 2008. *J. Meteor. Soc. Japan*, **90**, 701–719.

Kingsmill, D. E., 1995: Convection initiation associated with a seabreeze front, a gust front and their collision. *Mon. Wea. Rev.*, **123**, 2913–2933.

Kitada, T., 1987: Turbulence structure of sea breeze front and its implication in air pollution transport– Application of k-ε turbulence model. *Bound.-Layer Meteor.*, **41**, 217–239.

Kobayashi, F., Y. Ueno, N. Inatomi, and T. Shimura, 2001: Cumulonimbus which brought heavy rainfall in the metropolitan area on 21 July 1999. *Tenki*, **48**, 3–4 (in Japanese).

Kobayashi, F., H. Sugawara, Y. Ogawa, M. Kanda, and K. Ishii, 2007: Cumulonimbus generation in Tokyo metropolitan area during mid-summer days. *J. Atmos. Electr.*, **27**, 41–52.

Koch, G. J., J. Y. Beyon, B. W. Barnes, M. Petros, J. Yu, F. Amzajerdian, M. J. Kavaya, and U. N. Singh, 2007: High-energy 2 μm Doppler lidar for wind measurements. *Opt. Eng.*, **46**, 116201.

Koch, S. E., and W. L. Clark, 1999: A nonclassical cold front observed during COPS-91: Frontal structure and the process of severe storm initiation. *J. Atmos. Sci.*, **56**, 2862–2890.

Komatsubara, T., and N. Kaku, 2005: The status of wake vortex research in Japan. *Proc. 13th Coherent Laser Radar Conf.*, 140–143.

Korb, C. L., B. M. Gentry, and C.Y. Weng, 1992: Edge technique: theory and application to the lidar measurement of atmospheric wind. *Appl. Opt.*, **31**, 4202–4213.

Kozo, T. L., 1982: An observational study of sea breezes along the Alaskan Beaufort Sea coast: Part I. *J. Appl. Meteor.*, **21**, 891–905.

Kraus, H., J. M. Hacker, and J. Hartmann, 1990: An observational aircraft-based study of sea-breeze frontogenesis. *Bound.-Layer Meteor.*, **53**, 223–265.

Kristovich, D. A. R., 1993: Mean circulations of boundary-layer rolls in lake-effect snow storms. *Bound.-Layer Meteor.*, **63**, 293–315.

Kropfli, R. A., and N. M. Kohn, 1978: Persistent horizontal rolls in the urban mixed layer as revealed by

dual-Doppler radar. *J. Appl. Meteor.*, **17**, 669–676.

Kuettner, J. P., 1971: Cloud bands in the Earth's atmosphere. *Tellus*, **23**, 404–425.

Kurita, H., H. Ueda, and S. Mitsumoto, 1990: Combination of local wind systems under light gradient wind conditions and its contribution to the long-range transport of air pollutants. *J. Appl. Meteor.*, **29**, 331–348.

Kusunoki, K., 2002: A preliminary survey of clear-air echo appearances over the Kanto Plain in Japan from July to December 1997. *J. Atmos. Oceanic Technol.*, **19**, 1063–1072.

Kusunoki, K., and T. Matsumura, 1999: Clear-air radar echoes in boundary layers: The origin and the climatology in Japan. Preprints, *13th Symp. on Boundary Layers and Turbulence*, Dallas, TX, Amer. Meteor. Soc., 387–390.

Kusunoki, K., S. Saito, and H. Inoue, 2012: Radar and surface mesonet observations of convection initiation associated with seabreeze front and outflow boundary. *Proc. 7th European Conference on Radar in Meteorology and Hydrology*, Toulouse, France.

Lapworth, A., 2000: Observations of atmospheric density currents using a tethered balloonborne turbulence probe system. *Quart. J. Roy. Meteor. Soc.*, **126**, 2811–2850.

LeMone, M. A., 1973: The structure and dynamics of horizontal roll vortices in the planetary boundary layer. *J. Atmos. Sci.*, **30**, 1077–1091.

LeMone, M. A., 1976: Modulation of turbulence energy by longitudinal rolls in an unstable planetary boundary layer. *J. Atmos. Sci.*, **33**, 1308–1320.

Lemonsu, A., S. Bastin, V. Masson, and P. Drobinski, 2006: Vertical structure of the urban boundary layer over Marseille under sea-breeze conditions. *Bound.-Layer Meteor.*, **118**, 477–501.

Levin, M. J., 1965: Power spectrum parameter estimation. *IEEE Trans. Inform. Theory*, **11**, 100–107.

Lhermitte, R. M. and M. Gilet, 1975: Dual-Doppler radar observations and study of sea breeze convective storm development. *J. Appl. Meteor.*, **14**, 1346–1361.

Lin, C.-L., C. H. Moeng, P. P. Sullivan, and J. C. McWilliams, 1997: The effect of surface roughness on flow structures in a neutrally stratified planetary boundary layer. *Phys. Fluids*, **9**, 3235–3249.

Luhar, A. K., B. L. Sawford, J. M. Hacker, and K. N. Rayner, 1998: The Kwinana coastal fumigation study: II – Growth of the thermal internal boundary layer. *Bound.-Layer Meteor.*, **89**, 385–405.

Lyons, W. A., and L. E. Olsson, 1973: Detailed mesometeorological studies of air pollution dispersion in the Chicago lake breeze. *Mon. Wea. Rev.*, **101**, 387–403.

Lyons, W. A., R. A. Pielke, C. J. Tremback, R. L. Walko, D. A. Moon, and C. S. Keen, 1995: Modeling impacts of mesoscale vertical motions upon coastal zone air pollution dispersion. *Atmos. Environ.*, **29**, 283–301.

Maki, M., R. Misumi, T. Nakatani, S. Suzuki, T. Kobayashi, Y. Yamada, A. Adachi, I. Nakamura, M. Ishihara, and TOMACS members, 2012: Tokyo Metropolitan Area Convection Study for Extreme Weather Resilient Cities (TOMACS). *Proc. 7th European Conference on Radar in Meteorology and Hydrology*, Toulouse, France.

Markowski, P., C. Hannon, and E. Rasmussen, 2006: Observations of convection initiation "failure" from

the 12 June 2002 IHOP deployment. *Mon. Wea. Rev.*, **134**, 375–405.

Matayoshi, N., H. Inokuchi, K. Yazawa, and Y. Okuno, 2005: Development of airborne ultrasonic velocimeter and its application to helicopters. paper presented at AIAA Atmospheric Flight Mechanics Conference and Exhibit, San Francisco, U.S.A., AIAA 2005-6118, 15–18 August.

May, P. T., 1999: Thermodynamic and vertical velocity structure of two gust fronts observed with a wind profiler/RASS during MCTEX. *Mon. Wea. Rev.*, **127**, 1796–1807.

Mayor, S. D., 2011: Observations of seven density current fronts in Dixon, California. *Mon. Wea. Rev.*, **139**, 1338–1351.

Mega, T., K. Monden, T. Ushio, K. Okamoto, Z. Kawasaki, and T. Morimoto, 2007: A low-power high-resolution broad-band radar using a pulse compression technique for meteorological application. *IEEE Geosci. Remote Sens. Lett.*, **4**, 392–396.

Melas, D., and H. D. Kambezidis, 1992: The depth of the internal boundary layer over an urban area under sea-breeze conditions. *Bound.-Layer Meteor.*, **61**, 247–264.

Melfi, S. H., J. D. Spinhirne, S-H. Chou, and S. P. Palm, 1985: Lidar observation of vertically organized convection in the planetary boundary layer over the ocean. *J. Clim. Appl. Meteor.*, **24**, 806–821.

Menzies, R. T., 1986: Doppler lidar atmospheric wind sensors: A comparative performance evaluation for global measurement applications from earth orbit. *Appl. Opt.*, **25**, 2546–2553.

Menzies, R. T., and R. M. Hardesty, 1989: Coherent Doppler lidar for measurements of wind fields. *Proc. IEEE*, **77**, 449–462.

Miller, S. T. K., B. D. Keim, R. W. Talbot, and H. Mao, 2003: Sea breeze: Structure, forecasting, and impacts. *Rev. Geophys.*, **41**, 1011.

Mitsumoto, S., H. Ueda, and H. Ozoe, 1983: A laboratory experiment on the dynamics of the land and sea breeze. *J. Atmos. Sci.*, **40**, 1228–1240.

Mizutani, K., T. Itabe, S. Ishii, T. Aoki, K. Asai, A. Sato, H. Fukuoka, and T. Ishikawa, 2008: Conductive-cooled 2 micron laser for CO_2 and wind observations. *Lidar Remote Sensing for Environmental Monitoring IX*, U. N. Singh, K. Asai, and A. Jayaraman, Eds., International Society for Optical Engineering (SPIE Proceedings, Vol. 7153).

Mizutani, K., T. Itabe, S. Ishii, M. Aoki, K. Asai, A. Sato, H. Fukuoka, T. Ishikawa, and K. Noda, 2015: Diode-pumped 2-μm pulse laser with noncomposite Tm,Ho:YLF rod conductive-cooled down to –80°C. *Appl. Opt.*, **54**, 7865–7869.

Moeng, C.-H., and P. P. Sullivan, 1994: A comparison of shear- and buoyancy-driven planetary boundary layer flows. *J. Atmos. Sci.*, **51**, 999–1022.

Monin, A. S., and A. M. Obukhov, 1954: Basic laws of turbulent mixing in the ground layer of the atmosphere. *Trudy Geofiz. Inst. Akad. Nauk SSSR*, **24**, 163–187 (in Russian).

Mueller, C. K., J. W. Wilson, and N. A. Crook, 1993: The utility of sounding and mesonet data to nowcast thunderstorm initialization. *Wea. Forecasting*, **8**, 132–146.

Münkel, C., N. Eresmaa, J. Räsänen, and A. Karppinen, 2007: Retrieval of mixing height and dust concentration with lidar ceilometer. *Bound.-Layer Meteor.*, **124**, 117–128.

Neumann, J., 1973: The sea and land breezes in the classical Greek literature. *Bull. Amer. Meteor. Soc.*, **54**, 5–8.

Nakane, H., and Y. Sasano, 1986: Structure of a sea-breeze front revealed by scanning lidar observation. *J. Meteor. Soc. Japan*, **64**, 787–792.

Nakatani, T., R. Misumi, Y. Shoji, K. Saito, H. Seko, N. Seino, S. Suzuki, Y. Shusse, T. Maesaka, and H. Sugawara, 2015: Tokyo metropolitan area convection study for extreme weather resilient cities. *Bull. Amer. Meteor. Soc.*, **96**, ES123–ES126.

Newsom, R. K., R. Calhoun, D. Ligon, and J. Allwine, 2008: Linearly organized turbulence structures observed over a suburban area by dual-Doppler lidar. *Bound.-Layer Meteor.*, **127**, 111–130.

Oda, R., H. Iwai, Y. Murayama, S. Ishii, K. Mizutani, T. Itabe, N. Tsunematsu, I. Yamada, N. Matayoshi, D. Matsushima, W. Sha, T. Yamazaki and T. Iwasaki, 2010: Doppler lidar observations of the coherent structures in the internal boundary layer. *Preprints 9th Symp. on Urban Environment*, Keystone, CO, Amer. Meteor. Soc., 10.1.

Oda, R., H. Iwai, S. Ishii, S. Sekizawa, K. Mizutani, and Y. Murayama, 2011: Structure of turbulence in the urban atmospheric boundary layer detected in the Doppler lidar observation. *J. Jpn. Soc. Civil Eng. Ser. B1 (Hydraulic Engineering)*, **67**, I_313–I_318 (in Japanese).

Ogawa, S., W. Sha, T. Iwasaki, and Z. Wang, 2003: A numerical study on the interaction of a sea-breeze front with convective cells in the daytime boundary layer. *J. Meteor. Soc. Japan*, **81**, 635–651.

Ogura, Y., and N. A. Phillips, 1962: Scale analysis of deep and shallow convection in the atmosphere. *J. Atmos. Sci.*, **19**, 173–179.

Ohno, H., and O. Suzuki, 1993: Small-scale high wind cores enhancing low-level wind shear: Doppler radar observation of opposing wind adjacent to the sea-breeze frontal zone on 20 September 1989. *Meteor. Atmos. Phys.*, **81**, 635–651.

Okuno, Y., N. Matayoshi, Y. Terui, K. Wakairo, K. Hozumi, H. Inokuchi, and K. Funabiki, 2002: Development of a research helicopter MuPAL-ε. TECHNICAL MEMORANDUM OF NATIONAL AEROSPACE LABORATORY, TM-764 (in Japanese).

Parrish, D. D., D. T. Allen, T. S. Bates, M. Estes, R. C. Fehsenfeld, G. Feingold, R. Ferrare, R. M. Hardesty, J. F. Meagher, J. W. Nielsen-Gammon, R. B. Pierce, T. B. Ryerson, J. H. Seinfeld, and E. J. Williams, 2009: Overview of the Second Texas Air Quality Study (TexAQS II) and the Gulf of Mexico Atmospheric Composition and Climate Study (GoMACCS). *J. Geophys. Res.*, **114**, D00F13.

Pielke, R. A., 1974: A three-dimensional numerical model of the sea breezes over south Florida. *Mon. Wea. Rev.*, **102**, 115–139.

Pielke, R. A., and W. R. Cotton, 1977: A mesoscale analysis over south Florida for a high rainfall event. *Mon. Wea. Rev.*, **105**, 343–362.

Post, M. J., and R. E. Cupp, 1990: Optimizing a pulsed Doppler lidar. *Appl. Opt.*, **29**, 4145–4158.

Post, M. J., and W. D. Neff, 1986: Doppler lidar measurements of winds in a narrow mountain valley. *Bull. Amer. Meteor. Soc.*, **67**, 274–281.

Prahba, T. V., R. Venkatesan, E. Mursch-Radlgruber, G. Rengarajan, and N. Jayanthi, 2002: Thermal internal boundary layer characteristics at a tropical coastal site as observed by a mini-SODAR under varying synoptic conditions. *Proc. Indian Acad. Sci. (Earth Planet. Sci.)*, **111**, 63–77.

Press, W. H., B. P. Flannery, S. A. Teukolsky, and W. T. Vetterling, 1988: *Numerical Recipes in C*. Cambridge University Press, 317 pp.

Raasch, S., and G. Harbusch, 2001: An analysis of secondary circulations and their effects caused by small-scale surface inhomogeneities using large-eddy simulation. *Bound.-Layer Meteor.*, **101**, 31–59.

Raynor, G. S., J. V. Hayes, and E. C. Ogden, 1974: Mesoscale transport and dispersion of airborne pollens. *J. Appl. Meteor.*, **13**, 87–95.

Reible, D. D., J. E. Simpson, and P. F. Linden, 1993: The sea breeze and gravity-current frontogenesis. *Quart. J. Roy. Meteor. Soc.*, **119**, 1–16.

Reuter, G. W., and M. K. Yau, 1987: Mixing mechanisms in cumulus congestus clouds. Part II: Numerical simulations. *J. Atmos. Sci.*, **44**, 798–827.

Rotunno, R., 1983: On the linear theory of the land and sea breeze. *J. Atmos. Sci.*, **40**, 1999–2009.

Rye, B. J., and R. M. Hardesty, 1993: Discrete spectral peak estimation in incoherent backscatter heterodyne lidar. I: Spectral accumulation and the Cramer–Rao lower bound. *IEEE Trans. Geosci. Remote Sens.*, **31**, 16–27.

Saito, K., T. Fujita, Y. Yamada, J. Ishida, Y. Kumagai, K. Aranami, S. Ohmori, R. Nagasawa, S. Kumagai, C. Muroi, T. Kato, H. Eito, and Y. Yamazaki, 2006: The operational JMA non-hydrostatic model. *Mon. Wea. Rev.*, **134**, 1266–1298.

Saito, Y., Kobayashi, F., A. Katsura, T. Takamura, T. Takano, and T. Kurino, 2013: The lifetime of an isolated cumulonimbus observed by weather satellite (MTSAT-1R) rapid scans. *Tenki*, **60**, 247–260 (in Japanese).

Sakurai, N., K. Iwanami, T. Maesaka, S. Suzuki, S. Shimizu, R. Misumi, D.-S. Kim, and M. Maki, 2012: Case study of misoscale convective echo behavior associated with cumulonimbus development observed by Ka-band Doppler radar in the Kanto Region, Japan. *SOLA*, **8**, 107–110.

Sato, E., C. Fujiwara, K. Kusunoki and S. Saito, 2013: Characteristics of descending reflectivity cores observed by Ku-band radar. *Proc. 36th Conference on Radar Meteorology*, Breckenridge, CO.

Schreiber, W. E., 1986: Case studies of thunderstorms initiated by radar-observed convergent lines. *Mon. Wea. Rev.*, **114**, 2256–2266.

Seibert, P., F. Beyrich, S. E. Gryning, S. Joffre, A. Rasmussen, and P. Tercier, 2000: Review and intercomparison of operational methods for the determination of the mixing height. *Atmos. Environ.*, **34**, 1001–1027.

Seko, H., Y. Shoji, and F. Fujibe, 2007: Evolution and airflow structure of a Kanto thunderstorm on 21 July 1999 (the Nerima heavy rainfall event). *J. Meteor. Soc. Japan*, **85**, 455–477.

Sha, W., T. Kawamura, and H. Ueda, 1991: A numerical study on sea/land breezes as a gravity current: Kelvin-Helmholtz billows and inland penetration of the sea-breeze front. *J. Atmos. Sci.*, **48**, 1649–

1665.

Sha, W., T. Kawamura, and H. Ueda, 1993: A numerical study of nocturnal sea/land breezes: Prefrontal gravity waves in the compensating flow and inland penetration of the sea-breeze cutoff vortex. *J. Atmos. Sci.*, **50**, 1076–1088.

Shibata, T., M. Ishizu, and T. Itabe, 1991: Coherent Doppler lidar using a hybrid CO_2 laser with a low pressure gain section below the threshold. *J. Meteor. Soc. Japan*, **69**, 413–418.

Simpson, J. E., D. A. Mansfield, and J. R. Milford, 1977: Inland penetration of sea breeze fronts. *Quart. J. Roy. Meteor. Soc.*, **103**, 47–76.

Simpson, J. E., and R. E. Britter, 1980: A laboratory model of an atmospheric mesofront. *Quart. J. Roy. Meteor. Soc.*, **106**, 485–500.

Simpson, J. E., 1994: *Sea breeze and local wind*. Cambridge University Press, 234 pp.

Smedman, A. S., and U. Högström, 1983: Turbulent characteristics of a shallow convective internal boundary layer. *Bound.-Layer Meteor.*, **25**, 271–287.

Srivastava, V., M. A. Jarzembski, and D. A. Bowdle, 1992: Comparison of calculated aerosol backscatter at 9.1- and 2.1-μm wavelengths. *Appl. Opt.*, **31**, 1904–1906.

Stensrud, D. J., and R. A. Maddox, 1988: Opposing mesoscale circulations: A case study. *Wea. Forecasting*, **3**, 189–204.

Stephan, K., H. Kraus, C. M. Ewenz, and J. M. Hacker, 1999: Sea-breeze front variations in space and time. *Meteor. Atmos. Phys.*, **70**, 81–95.

Stevens, E. R., 1975: Chemistry and meteorology in an air pollution episode. *J. Air Poll. Contr. Ass.*, **25**, 271–274.

Steyn, D. G., 1998. Scaling the vertical structure of sea breezes. *Bound.-Layer Meteor.*, **86**, 505–524.

Steyn, D. G., 2003. Scaling the vertical structure of sea breezes revisited. *Bound.-Layer Meteor.*, **107**, 177––188.

Strauch, R. G., D. A. Merritt, K. P. Moran, K. B. Earnshaw, and D. Van De Kamp, 1984: The Colorado wind profiling network. *J. Atmos. Oceanic Technol.*, **1**, 37–49.

Stull, R. B., 1988: *An Introduction to Boundary Layer Meteorology*. Kluwer Academic, 666 pp.

Sykes, R. I., and D. S. Henn, 1989: Large-eddy simulation of turbulent sheared convection. *J. Atmos. Sci.*, **46**, 1106–1118.

Talbot, C., P. Augustin, C. Leroy, V. Willart, H. Delbarre, and G. Khomenko, 2007: Impact of a sea breeze on the boundary-layer dynamics and the atmospheric stratification in a coastal area of the North Sea. *Bound.-Layer Meteor.*, **125**, 133–154.

Thompson, W. T., T. Holt, and J. Pullen, 2007: Investigation of a sea breeze front in an urban environment. *Quart. J. Roy. Meteor. Soc.*, **133**, 579–594.

Tsunematsu, N., H. Iwai, S. Ishii, Y. Murayama, M. Yasui, and K. Mizutani, 2009: The formation of sharp multi-layered wind structure over Tokyo associated with sea-breeze circulation. *SOLA*, **5**, 1–4.

Tucker, S. C., R. M. Banta, A. O. Langford, C. J. Senff, W. A. Brewer, E. J. Williams, B. M. Lerner, H. Osthoff, and R. M. Hardesty, 2010: Relationships of coastal nocturnal boundary layer winds and

turbulence to Houston ozone concentrations during TexAQS 2006. *J. Geophys. Res.*, **115**, D10304.

Ueda, H., S. Mitsumoto, and H. Kurita, 1988: Flow mechanism for the long-range transport of air pollutants by the sea breeze causing inland nighttime high oxidants. *J. Appl. Meteor.*, **27**, 182–187.

United Nations Department of Economic and Social Affairs, 2007: PERCENTAGE OF TOTAL POPULATION LIVING IN COASTAL AREAS. Indicators of Sustainable Development: Guidelines and Methodologies, 3rd Edition.

Vaisala, 1999: *Ceilometer CT25K User's Guide*. CT25K-U059en-2.1, Helsinki, Finland, 125 pp.

Venkatram, A., 1977: A model of internal boundary-layer development. *Bound.-Layer Meteor.*, **11**, 419–437.

Young, G. S., D. S. Kristovich, M. R. Hjelmfelt, and R. C. Foster, 2002: Rolls, streets, waves and more: A review of quasi-two dimensional structures in the atmospheric boundary layer. *Bull. Amer. Meteor. Soc.*, **83**, 997–1001.

Wakimoto, R. M., 1982: The life cycle of thunderstorm gust fronts as viewed with Doppler radar and rawinsonde data. *Mon. Wea. Rev.*, **110**, 1060–1082.

Wakimoto, R. M., and N. T. Atkins, 1994: Observations of the sea-breeze front during CaPE. Part I: Single-Doppler, satellite, and cloud photogrammetry analysis. *Mon. Wea. Rev.*, **122**, 1092–1114.

Wakimoto, R. M., H. V. Murphey, E. V. Browell, and S. Ismail, 2006: The "triple point" on 24 May 2002 during IHOP. Part I: Airborne Doppler and LASE analyses of the frontal boundaries and convection initiation. *Mon. Wea. Rev.*, **134**, 231–250.

Wallington, C. E., 1959: The structure of the sea breeze front as revealed by gliding flights. *Weather*, **14**, 263–270.

Walsh, J. E., 1974: Sea breeze theory and applications. *J. Atmos. Sci.*, **31**, 2012–2026.

Weckwerth, T. M., J. W. Wilson, and R. M. Wakimoto, 1996: Thermodynamic variability within the convective boundary layer due to horizontal convective rolls. *Mon. Wea. Rev.*, **124**, 769–784.

Weckwerth, T. M., J. W. Wilson, R. M. Wakimoto, and N. A. Crook, 1997: Horizontal convective rolls: Determining the environmental conditions supporting their existence and characteristics. *Mon. Wea. Rev.*, **125**, 505–526.

Weckwerth, T. M., D. B. Parsons, S. E. Koch, J. A. Moore, M. A. LeMone, B. B. Demoz, C. Flamant, B. Geerts, J. Wang, and W. F. Feltz, 2004: An overview of the International H_2O Project (IHOP_2002) and some preliminary highlights. *Bull. Amer. Meteor. Soc.*, **85**, 253–277

Werner, C., P. H. Flamant, O. Reitebuch, F. Köpp, J. Streicher, S. Rahm, E. Nagel, M. Klier, H. Herrmann, C. Loth, P. Delville, P. Drobinski, B. Romand, C. Boitel, D. Oh, M. Lopez, M. Messionnier, D. Bruneau, and A. Dabas, 2001: Wind infrared Doppler lidar instrument. *Opt. Eng.*, **40**, 116–125.

Werner, C., 2005: Doppler wind lidar. *Lidar: Range-Resolved Optical Remote Sensing of the Atmosphere*, C. Weitkamp, Ed., Series in Optical Sciences, Vol. 102, Springer, 339–342.

White, A. B., C. W. Fairall, and D. W. Thomson, 1991: Radar observations of humidity variability in and above the marine atmospheric boundary layer. *J. Atmos. Oceanic Technol.*, **8**, 639–658.

Wilson, J. W., and W. E. Schreiber, 1986: Initiation of convective storms by radar-observed boundary layer

convergent lines. *Mon. Wea. Rev.*, **114**, 2516–2536.

Wilson, J. W, and D. L. Megenhardt, 1997: Thunderstorm initiation, organization and lifetime associated with Florida boundary layer convergence lines. *Mon. Wea. Rev.*, **125**, 1507–1525.

Wilson, J. W., G. B. Foote, N. A. Crook, J. C. Fankhauser, C. G. Wade, J. D. Tuttle, C. K. Muller, and S. N. Krueger, 1992: The role of boundary-layer convergence zones and horizontal rolls in the initiation of thunderstorms: A case study. *Mon. Wea. Rev.*, **120**, 1785–1814.

Wilson, J. W., and C. K. Mueller, 1993: Nowcasts of thunderstorm initialization and evolution. *Wea. Forecasting*, **8**, 113–131.

Wilson, J. W., R. E. Carbone, J. D. Tuttle, and T. D. Keenan, 2001: Tropical island convection in the absence of significant topography. Part II: Nowcasting storm evolution. *Mon. Wea. Rev.*, **129**, 1637–1655.

Wood, R., I. M. Storomberg, and P. R. Jonas, 1999: Aircraft observation of sea-breeze frontal structure. *Quart. J. Roy. Meteor. Soc.*, **125**, 1959–1995.

Wulfmeyer, V., A. Behrendt, H.-S. Bauer, C. Kottmeier, U. Corsmeier, A. Blyth, G. Craig, U. Schumann, M. Hagen, S. Crewell, P. D. Girolamo, C. Flamant, M. Miller, A. Montani, S. Mobbs, E. Richard, M. W. Rotach, M. Arpagaus, H. Russchenberg, P. Schlüssel, M. König, V. Gärtner, R. Steinacker, M. Dorninger, D. D. Turner, T. Weckwerth, A. Hense, and C. Simmer, 2008: The convective and orographically induced precipitation study: A research and development project of the World Weather Research Program for improving quantitative precipitation forecasting in low-mountain regions. *Bull. Amer. Meteor. Soc.*, **89**, 1477–1486.

Xu, Q., 1992: Density currents in shear flows–A two-fluid model. *J. Atmos. Sci.*, **49**, 511–524.

Yasui, M., J. Zhou, L. Liu, T. Itabe, K. Mizutani, and T. Aoki, 2005: Vertical profiles of aeolian dust in a desert atmosphere observed using lidar in Shapotou, China. *J. Meteor. Soc. Japan*, **83A**, 149–171.

Yoshikado, H., and H. Kondo, 1989: Inland penetration of the sea breeze over the suburban area of Tokyo. *Bound.-Layer Meteor.*, **48**, 389–407.

Yoshikado, H., 1990: Vertical structure of the sea breeze penetrating through a large urban complex. *J. Appl. Meteor.*, **29**, 878–891.

Yoshikado, H., 1992: Numerical study of the daytime urban effect and its interaction with the sea breeze. *J. Appl. Meteor.*, **31**, 1146–1164.

Yoshikawa, E., T. Ushio, Z. Kawasaki, T. Mega, S. Yoshida, T. Morimoto, K. Imai, and S. Nagayama, 2010: Development and initial observation of high-resolution volume-scanning radar for meteorological application. *IEEE Trans. Geosci. Remote Sens.*, **48**, 3225–3235.

Ziegler, C. L., T. J. Lee, and R. A. Pielke Sr., 1997: Convection initiation at the dryline: A modeling study. *Mon. Wea. Rev.*, **125**, 1001–1026.

Ziegler, C. L., and E. N. Rasmussen, 1998: The initiation of moist convection at the dryline: Forecasting issues from a case study perspective. *Wea. Forecasting*, **13**, 1106–1131.

Ziegler, C. L., E. N. Rasmussen, M. S. Buban, Y. P. Richardson, L. J. Miller, and R. M. Rain 2007: The “triple point” on 24 May 2002 during IHOP. Part II: Ground-radar and in situ boundary layer

analysis of cumulus development and convection initiation. *Mon. Wea. Rev.*, **135**, 2443–2472.

Publication list

Refereed journals

1. Iwai, H., S. Ishii, N. Tsunematsu, K. Mizutani, Y. Murayama, T. Itabe, I. Yamada, N. Matayoshi, D. Matsushima, W. Sha, T. Yamazaki, and T. Iwasaki, 2008: Dual-Doppler lidar observation of horizontal convective rolls and near-surface streaks. *Geophys. Res. Lett.*, **35**, L14808, doi:10.1029/2008GL034571.
2. Tsunematsu. N., H. Iwai, S. Ishii, Y. Murayama, M. Yasui, and K. Mizutani, 2009: The formation of sharp multi-layered wind structure over Tokyo associated with sea-breeze circulation. *SOLA*, **5**, 1–4, doi:10.2151/sola.2009–001.
3. Tsunematsu. N., H. Iwai, S. Ishii, M. Yasui, Y. Murayama, and K. Mizutani, 2009: Influence of surface-based stable layer development on Asian dust behaviour over Tokyo. *Bound.-Layer Meteor.*, **131**, 263–275, doi:10.1007/s10546-001-9366-6.
4. Ishii, S., K. Mizutani, H. Fukuoka, T. Ishikawa, P. Baron, H. Iwai, T. Aoki, T. Itabe, A. Sato, and K. Asai, 2010: Coherent 2μm differential absorption and wind lidar with conductively-cooled laser and two-axis scanning device. *Appl. Opt.*, **49**, 1809–1817, doi:10.1364/AO.49.001809.
5. Iwai, H., Y. Murayama, S. Ishii, K. Mizutani, Y. Ohno, and T. Hashiguchi, 2011: Strong updraft at a sea-breeze front and associated vertical transport of near-surface dense aerosol observed by Doppler lidar and ceilometer. *Bound.-Layer Meteor.*, **141**, 117–142, doi:10.1007/s10546-011-9635-z.
6. Oda, R., H. Iwai, S. Ishii, S. Sekizawa, K. Mizutani, and Y. Murayama, 2011: Structure of turbulence in the urban atmospheric boundary layer detected in the Doppler lidar observation. *J. Jpn. Soc. Civil Eng. Ser. B1 (Hydraulic Engineering)*, **67**, I_313-I_318, doi:10.2208/ jscejhe.67.I_313 (in Japanese).
7. Oda, R., H. Iwai, A. Inagaki, S. Satoh, S. Sekizawa, S. Ishii, K. Mizutani, and Y. Murayama, 2012: Structure of stable nocturnal boundary layer in urban area detected in a Doppler lidar observation. *J. Jpn. Soc. Civil Eng. Ser. B1 (Hydraulic Engineering)*, **68**, I_1777–I_1782, doi:10.2208/jscejhe.68.I_1777 (in Japanese).
8. Ishii, S., K. Mizutani, P. Baron, H. Iwai, R. Oda, T. Itabe, H. Fukuoka, T. Ishikawa, M. Koyama, T. Tanaka, I. Morino, O. Uchino, A. Sato, and K. Asai, 2012: Partial CO_2 column-averaged dry-air mixing ratio from measurements by coherent 2-μm differential absorption and wind lidar with laser frequency offset locking. *J. Atmos. Oceanic Technol.*, **29**, 1169–1181, doi:10.1175/JTECH-D-11-00180.1.
9. Sawada, M., T. Iwasaki, W. Sha, T. Yamazaki, H. Iwai, S. Ishii, K. Mizutani, T. Itabe, and I. Yamada, 2012: Transient downslope winds under the influence of stationary lee waves from the Zao mountain range. *J. Meteor. Soc. Japan*, **90**, 79–100, doi:10.2151/jmsj.2012-105.
10. Iwai, H., S. Ishii, R. Oda, K. Mizutani, S. Sekizawa, and Y. Murayama, 2013: Performance and technique of coherent 2-μm differential absorption and wind lidar for wind measurement. *J. Atmos. Oceanic Technol.*, **30**, 429–448, doi:10.1175/JTECH-D-12-00111.1.

11. Ishii, S., M. Koyama, P. Baron, H. Iwai, K. Mizutani, T. Itabe , A. Sato, and K. Asai, 2013: Ground-based integrated path coherent differential absorption lidar measurement of CO_2: foothill target return. *Atmos. Meas. Tech*., **6**, 1169–1181, doi:10.5194/amt-6-1359-2013.
12. Kawabata, T., H. Iwai, H. Seko, Y. Shoji, K. Saito, S. Ishii, and K. Mizutani, 2014: Cloud-resolving 4D-Var assimilation of Doppler wind lidar data on a meso-gamma scale convective system. *Mon. Wea. Rev.*, **142**, 4484–4498, doi:10.1175/MWR-D-13-00362.1.
13. Chen, G., X. Zhu, W. Sha, T. Iwasaki, H. Seko, K. Saito, H. Iwai, and S. Ishii, 2015a: Toward improved forecast of sea-breeze horizontal convective rolls at super high resolution. Part I: configuration and verification of a Down-Scaling Simulation System (DS^3). *Mon. Wea. Rev.*, **143**, 1849–1872, doi:10.1175/MWR-D-14-00212.1.
14. Chen, G., X. Zhu, W. Sha, T. Iwasaki, H. Seko, K. Saito, H. Iwai, and S. Ishii, 2015b: Toward improved forecast of sea-breeze horizontal convective rolls at super high resolution. Part II: The impacts of land use and buildings. *Mon. Wea. Rev.*, **143**, 1873–1894, doi:10.1175/MWR-D-14-00230.1.
15. Aoki, M., H. Iwai, K. Nakagawa, S. Ishii, and K. Mizutani, 2016: Measurements of rainfall velocity and raindrop size distribution using coherent Doppler lidar. *J. Atmos. Oceanic Technol.*, **33**, 1949–1966, doi:10.1175/JTECH-D-15-0111.1.
16. Kawamura, S., H. Ohta, H. Hanado, M. K. Yamamoto, N. Shiga, K. Kido, S. Yasuda, T. Goto, R. Ichikawa, J. Amagai, K. Imamura, M. Fujieda, H. Iwai, S. Sugitani, and T. Iguchi, 2017: Water vapor estimation using digital terrestrial broadcasting waves. *Radio Sci.*, doi:10.1002/2016RS006191.
17. Iwai, H., S. Ishii, S. Kawamura, E. Sato, and K. Kusunoki, 2018: Case study on convection initiation associated with an isolated convective storm developed over flat terrain during TOMACS. *J. Meteor. Soc. Japan*, **96A**, doi:10.2151/jmsj.2017-014.

Unrefereed articles

1. Iwai, H., S. Ishii, K. Mizutani, Y. Murayama, N. Kaku, W. Sha, T. Yamazaki, and T. Iwasaki, 2007: Single- and Dual-Doppler lidar measurements of the sea breeze at Sendai Airport. *Proc. 14th Coherent Laser Radar Conf.*, Snowmass, CO.
2. K. Mizutani, T. Itabe, S. Ishii, T. Aoki, Y. Murayama, H. Iwai, K. Asai, A. Sato, H. Fukuoka, and T. Ishikawa, 2007: Wind lidar developments and measurements at NICT. *Proc. 14th Coherent Laser Radar Conf.*, Snowmass, CO.
3. N. Tsunematsu, H. Iwai, S. Ishii, Y. Murayama, M. Yasui, K. Mizutani, S. Kawamura, and Y. Ohno, 2007: A case study of multi-layered wind structure over Tokyo associated with sea breeze circulation by use of a coherent Doppler lidar and the WRF model. *Proc. 14th Coherent Laser Radar Conf.*, Snowmass, CO.
4. Iwai, H., S. Ishii, N. Tsunematsu, K. Mizutani, Y. Murayama, I. Yamada, R. Yoshida, W. Sha, T. Yamazaki, and T. Iwasaki, 2007: Dual-Doppler lidar measurements of three-dimensional flow over Sendai Airport. *Proc. 7th Int. Symp. on Advanced Fluid Information and 4th Int. Symp. on*

Transdisciplinary Fluid Integration, 24–27, Sendai.

5. Tamura, K., W. Sha, T. Yamazaki, T. Iwasaki, H. Iwai, S. Ishii, T. Itabe, K. Mizutani, N. Tsunematsu, T. Aoki, and I. Yamada, 2007: High resolution simulation of seabreeze and its validation with Doppler Lidar observation in Sendai Airport. *Proc. 7th Int. Symp. on Advanced Fluid Information and 4th Int. Symp. on Transdisciplinary Fluid Integration*, 38–39, Sendai.
6. Iwai, H., S. Ishii, N. Tsunematsu, K. Mizutani, Y. Murayama, T. Itabe, I. Yamada, N. Matayoshi, D. Matsushima, W. Sha, T. Yamazaki, and T. Iwasaki, 2008: Observations of near-surface streaks utilizing dual-Doppler lidar and heliborne sensors. *Proc. 24th Int. Laser Radar Conf.*, 346–349, Boulder, CO.
7. Ishii, S., K. Mizutani, H. Fukuoka, T. Ishikawa, H. Iwai, P. Baron, J. Mendrok, Y. Kasai, T. Aoki, A. Sato, K. Asai, and T. Itabe, 2008: Deveolopment of 2 micron coherent differential absorption lidar. *Proc. 24th Int. Laser Radar Conf.*, 689–692, Boulder, CO.
8. Iwai, H., S. Ishii, N. Tsunematsu, K. Mizutani, Y. Murayama, T. Itabe, I. Yamada, N. Matayoshi, D. Matsushima, W. Sha, T. Yamazaki, and T. Iwasaki, 2009: Comparison of dual-Doppler lidar measurements of wind with helicopter measurements. *Proc. 15th Coherent Laser Radar Conf.*, 103–106, Toulouse, France.
9. Ishii, S., K. Mizutani, H. Fukuoka, T. Ishikawa, H. Iwai, P. Baron, T. Aoki, A. Sato, K. Asai, and T. Itabe, 2009: Development of coherent 2-μm differential absorption and wind lidar. *Proc. 15th Coherent Laser Radar Conf.*, 85–88, Toulouse, France.
10. Iwai, H., T. Hashiguchi, S. Ishii, K. Mizutani, and Y. Murayama, 2009: A strong updraft at a sea-breeze front over the Tokyo metropolitan area observed by Doppler lidar. *Proc. 7th Int. Conf. on Urban Climate*, P4-25, Yokohama.
11. Tsunematsu, N., Y. Murayama, H. Iwai, M. Yasui, S. Ishii, K. Mizutani, T. Nagani, T. Sakai, and T. Murayama, 2009: The influence of local meteorological phenomena on the behavior of aeolian dust over the Tokyo metropolitan area. *Proc. 7th Int. Conf. on Urban Climate*, A14-3, Yokohama.
12. S. Ishii, K. Mizutani, H. Iwai, T. Aoki, T. Itabe, A. Sato, and K. Asai, 2009: Development of differential absorption lidar for CO_2 measurement, *Technical report of IEICE. SANE*, **109(13)**, 31–35, Okinawa (in Japanese).
13. Oda, R., H. Iwai, Y. Murayama, S. Ishii, K. Mizutani, T. Itabe, N. Tsunematsu, I. Yamada, N. Matayoshi, D. Matsushima, W. Sha, T. Yamazaki and T. Iwasaki, 2010: Doppler lidar observation study on the horizontal turbulent structures in the internal boundary layer. *Proc. Hydraulic Engineering*, **54**, 277–282, Sapporo (in Japanese).
14. Ishii, S., K. Mizutani, H. Fukuoka, T. Ishikawa, P. Baron, H. Iwai, T. Aoki, T. Itabe, A. Sato, and K. Asai, 2010: Development of coherent 2-μm differential absorption lidar with laser frequency offset locking. *Proc. 25th Int. Laser Radar Conf.*, 834–837, St. Petersburg, Russia.
15. Oda, R., H. Iwai, Y. Murayama, S. Ishii, K. Mizutani, T. Itabe, N. Tsunematsu, I. Yamada, N. Matayoshi, D. Matsushima, W. Sha, T. Yamazaki and T. Iwasaki, 2010: Doppler lidar observations of the coherent structures in the internal boundary layer. *Preprints 9th Symp. on Urban Environment*,

Keystone, CO.

16. Ishii, S., K. Mizutani, H. Fukuoka, T. Ishikawa, P. Baron, H. Iwai, T. Aoki, T. Itabe, A. Sato, and K. Asai, 2010: Development of coherent 2-μm differential absorption and wind lidar with laser frequency offset locking technique. *Proc. SPIE*, **7860**, 786004-1–786004-6, Incheon, Korea.
17. Ishii, S., H. Iwai, and K. Mizutani, 2011: Doppler lidar for wind measurement and its applications. *The Review of Laser Engineering*, **39**, 596–600, doi:10.2184/lsj.39.596 (in Japanese).
18. Ishii, S., K. Mizutani, H. Fukuoka, T. Ishikawa, P. Baron, T. Tanaka, I. Morino, O. Uchino, H. Iwai, T. Aoki, T. Itabe, A. Sato, and K. Asai, 2011: Development of coherent 2-μm differential absorption and wind lidar with laser frequency offset locking technique and column-integrated CO_2 measurement. *Proc. 16th Coherent Laser Radar Conf.*, Long Beach, CA.
19. Mizutani, K., T. Itabe, S. Ishii, H. Iwai, K. Asai, A. Sato, H. Fukuoka, T. Ishikawa, T. Kase, and T. Shiina, 2011: 2-micron laser development for wind and CO_2 observations. *Proc. 16th Coherent Laser Radar Conf.*, Long Beach, CA.
20. Oda, R., H. Iwai, A. Inagaki, S. Ishii, S. Satoh, S. Sekizawa, K. Mizutani, and Y. Murayama, 2012: Doppler lidar observation of turbulent mixing in the urban atmospheric boundary layer. *Proc. 8th Int. Conf. on Urban Climate*, Dublin, Ireland.
21. Iwai, H., S. Ishii, R. Oda, K. Mizutani, and Y. Murayama, 2012: Performance evaluation of coherent 2-μm differential absorption and wind lidar for wind measurement. *Proc. SPIE*, **8526**, 85260Z-1–85260Z-7, Kyoto.
22. Mizutani, K., T. Itabe, S. Ishii, H. Iwai, K. Asai, A. Sato, H. Fukuoka, T. Ishikawa, and T. Kase, 2013: 2-micron laser development for wind and CO_2 sensing. *Proc. 17th Coherent Laser Radar Conf.*, Barcelona, Spain.
23. Ishii, S., H. Iwai, K. Mizutani, P. Baron, T. Itabe, H. Fukuoka, T. Ishikawa, A. Sato, and K. Asai, 2013: 2-μm coherent lidar for CO_2 and wind measurements. *Proc. SPIE*, **8872**, 887206-1–887206-10, San Diego, CA.
24. Yasui, M., S. Ishii, and H. Iwai, 2013: New generation wind measurement technique for disaster prevention: 3-dimensional wind observation by Doppler lidar. *J. Inst. Electr. Engin. Japan*, **133**, 138–140, doi:10.1541/ieejjournal.133.138 (in Japanese).
25. Iwai, H., S. Ishii, and K. Mizutani, 2016: Wind measurements by Doppler lidar and its application to weather forecasting. *J. Inst. Electr. Engin. Japan*, **136**, 534–537, doi:10.1541/ieejjournal.136.534 (in Japanese).